# Synthesis and applications of porous non-silica metal oxide submicrospheres

Yash Boyjoo,[a] Meiwen Wang,[a] Vishnu K. Pareek,[a] Jian Liu*[a] and Mietek Jaroniec*[b]

Nowadays the development of submicroscale products of specific size and morphology that feature a high surface area to volume ratio, well-developed and accessible porosity for adsorbates and reactants, and are non-toxic, biocompatible, thermally stable and suitable as synergetic supports for precious metal catalysts is of great importance for many advanced applications. Complex porous non-silica metal oxide submicrospheres constitute an important class of materials that fulfill all these qualities and in addition, they are relatively easy to synthesize. This review presents a comprehensive appraisal of the methods used for the synthesis of a wide range of porous non-silica metal oxide particles of spherical morphology such as porous solid spheres, core–shell and yolk–shell particles as well as single-shell and multi-shell particles. In particular, hydrothermal and low temperature solution precipitation methods, which both include various structure developing strategies such as hard templating, soft templating, hydrolysis, or those taking advantage of Ostwald ripening and the Kirkendall effect, are reviewed. In addition, a critical assessment of the effects of different experimental parameters such as reaction time, reaction temperature, calcination, pH and the type of reactants and solvents on the structure of the final products is presented. Finally, the practical usefulness of complex porous non-silica metal oxide submicrospheres in sensing, catalysis, biomedical, environmental and energy-related applications is presented.

## 1. Introduction

The design of functional nano- and microsized particles is a hot topic due to their application in a wide range of fields such as energy conversion and storage, catalysis, biomedicine, and environmental remediation. These tiny particles feature a high surface area to volume ratio, which is beneficial for diffusion and transport of reactants and products.

[a] *Department of Chemical Engineering, Curtin University, Perth, WA, 6845, Australia. E-mail: jian.liu@curtin.edu.au*
[b] *Department of Chemistry & Biochemistry, Kent State University, Kent, Ohio 44242, USA. E-mail: jaroniec@kent.edu*

*Yash Boyjoo received his PhD in 2013 from Curtin University, Australia. After two years as a research associate at Curtin University working with Dr Jian Liu and Prof. Vishnu Pareek, he currently works as a postdoctoral research fellow at Université Lille 1 in France, where his studies deal with the synthesis of materials for VOC elimination from polluted air. His other research interests include photocatalytic wastewater treatment, synthesis of activated carbons for application as $CO_2$ adsorbents and supercapacitors, and the design and modelling of photocatalytic reactors.*

**Yash Boyjoo**

*Meiwen (Sharon) Wang received her bachelor's degree with first class honours in Chemical Engineering at Curtin University, where she is now pursuing PhD research under the supervision of Dr Jian Liu. She is interested in the design and fabrication of yolk–shell particles and their use as nanoreactors.*

**Meiwen Wang**

This journal is © The Royal Society of Chemistry 2016

*Chem. Soc. Rev.*, 2016, 45, 6013–6047 | 6013

Furthermore, depending on the material used, the particle size, crystal size, surface area, pore size distribution, and morphology can be tailored for specific applications by adjusting the chemical composition and synthesis conditions.

Metal oxides (MeO) exhibit several attractive features such as high mechanical strength, thermal stability, chemical inertness, non-toxicity, biocompatibility, oxygen vacancies, semiconductor properties and high isoelectric point, and can act as supports for noble metals such as Au, Pt and Pd, or rare earth metals to achieve synergistic catalytic activity toward specific chemical reactions. Furthermore, for nanosized crystals, quantum effects become important as reflected by significantly different optical and electronic properties from those observed for the
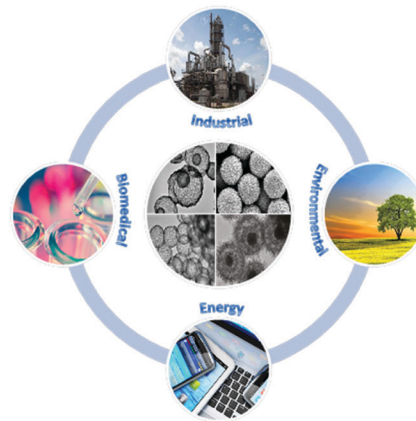


Fig. 1   Spherical metal oxide particles and their potential applications.

bulk phases,[1] which can have favorable outcomes for their application in catalysis and photocatalysis; for example, new physicochemical phenomena such as ferromagnetism and paramagnetism can be achieved for otherwise antiferromagnetic systems, as in the case of NiO spheres.[2] As a result, countless studies have been performed to synthesize submicrosized porous non-silica metal oxide particles with different morphologies, phases, sizes, crystal sizes and pore size distributions. These particles are useful for a variety of industrial, biomedical, environmental and energy-related applications as illustrated in Fig. 1.

The porous non-silica metal oxide submicrospheres can be designed to have large surface areas and well-developed porosity to enhance interfacial interactions with reactants and facilitate the transport and diffusion of reactants and products. Also, the crystal size and growth directions need to be considered for specific catalytic and semiconductor applications. Furthermore, a proper balance between micropores, mesopores and

*Vishnu Pareek is a Professor in the Department of Chemical Engineering at Curtin University, Australia. He received his PhD degree from the University of New South Wales, an MTech from IIT Delhi and a BE from the University of Rajasthan, Jaipur, all in Chemical Engineering and with high distinction. Prof. Pareek's expertise lies in the simulation and design of chemical processes with particular emphasis on the use of these tools in industrial-*

**Vishnu K. Pareek**

*scale processes. He is an ardent cricket fan and an enthusiastic reader especially on subjects related to politics, environment and economy. In his spare time, he is a bird watcher with special interest in understanding the behaviour of birds of prey.*

*Jian Liu obtained his PhD degree in Physical Chemistry from the Dalian Institute of Chemical Physics, Chinese Academy of Science, in 2008. Subsequently, he moved to Australia and worked as a Postdoctoral Research Fellow at AIBN, the University of Queensland. He started as a Lecturer at Curtin University in 2013 and was promoted to Senior Lecturer in 2014. Dr Liu has published more than 120 peer reviewed journal articles with over 6300 citations*

**Jian Liu**

*(H-index of 43). He has been honoured with a prestigious UQ Foundation Research Excellence Award and Australian Postdoctoral Fellowship. His current research interests are nanoreactor design, green chemical processes, and utilization of $CO_2$.*

*Mietek Jaroniec received his MS and PhD from M. Curie-Sklodowska University, Poland, in 1972 and 1976, respectively. Since 1991 he has been a Professor of Chemistry at Kent State University, Kent, Ohio (USA). Before joining Kent State he was a Professor of Chemistry at M. Curie-Sklodowska University, Poland. His research interests revolve primarily around inter-disciplinary topics of interfacial chemistry, and chemistry of materials, including physical*

**Mietek Jaroniec**

*adsorption at the gas/solid and liquid/solid interfaces, adsorbents, and catalysts. At Kent State he has established a vigorous research program in the area of ordered nanoporous materials such as ordered mesoporous silicas, organosilicas, inorganic oxides and carbons, focusing on their synthesis and environmental and energy-related applications.*

6014 | Chem. Soc. Rev., 2016, 45, 6013–6047

This journal is © The Royal Society of Chemistry 2016

macropores that respectively act as reaction sites, distribution/ evacuation pathways and reservoirs is desired. The spherical morphology is the most stable shape that is achieved in nature. In the case of metal oxides, the advantages offered by spherical structures are high mechanical strength, short pathways for diffusion of species, dispersion enhancement due to the stabilization of electrostatic charges, high surface area to volume ratios, easy coating with other species or metal oxides, minimization of viscous effects and predictable hydrodynamics. Typical spherical morphologies of metal oxides discussed in this review can be classified into three groups: porous solid spheres (Fig. 2Aa), core–shell spheres (Fig. 2Ab) and hollow spheres (Fig. 2Ac). The core–shell spheres shown in Fig. 2Ab can be further extended into single-core particles with a multi-particle (raspberry-like) shell (Fig. 2Ab1), multi-core particles with a single shell (Fig. 2Ab2), single-core particles with a multi-shell (Fig. 2Ab3), or a combination of particles shown in Fig. 2Ab and b1 (see Fig. 2Ab4). Also, hollow spheres can be further classified into yolk–shell spheres (Fig. 2Ac1) and multi-shell hollow spheres (Fig. 2Ac2). In principle, each compartment of these spheres can be nonporous or porous with different pore sizes (micropores, mesopores, and macropores). More complex metal oxide spheres can be proposed and synthesized by combining and modifying the aforementioned nine patterns as shown in Fig. 2A.

Several excellent reviews have been published previously focusing on the synthesis and applications of metal oxides. However, these reviews consider either a specific metal oxide such as $TiO_2$[4,5] and iron oxides,[6] or a specific application such as gas sensors,[7] energy storage and conversion applications[8,9] or a specific morphology such as hollow spheres[10] and multi-shell structures.[11] Indeed, a concise and up-to-date review on the synthesis strategies of different types of porous non-silica metal oxide submicrospheres with various spherical morphologies as well as their emerging applications is timely as this research field continuous to rapidly grow. This review is focused on the synthesis and applications of non-silica-based metal oxide spheres based on the literature for the past five years. One of the main sections of this review is devoted to the major strategies frequently used for the preparation of MeO particles such as hydrothermal/solvothermal synthesis at elevated temperatures ($>100$ °C), solution precipitation synthesis at low temperatures ($<100$ °C), and the aerosol-type synthesis. Other methods are only briefly mentioned. The hydrothermal and low temperature precipitation syntheses are general methods that allow for the development of more sophisticated structures by hard templating, soft templating or controlled hydrolysis, or by taking advantage of Ostwald ripening and the Kirkendall effect.[11,12] The aforementioned section on the synthesis methods is supplemented by a critical appraisal of the effect of different experimental parameters such as reaction time, reaction temperature, calcination, pH and the type of reactants and solvents on the structure of the resulting metal oxide particles. Finally, the last section presents the major applications of metal oxide spheres in industrially relevant sensing and catalysis, in the development of biomedically relevant photoluminescent devices and drug delivery vehicles, in environmentally relevant photocatalysis and adsorption, and in energy-relevant applications such as lithium-ion batteries, supercapacitors and dye sensitized solar cells.



Fig. 2  (A) Graphically illustrated classification of metal oxide spheres: (a) porous spheres; (b) core–shell spheres: (b1) raspberry-like core–shell spheres; (b2) multi-core spheres with a single shell; (b3) single-core spheres with multi-shells; (b4) raspberry-like single-core with multi-shells; and (c) hollow spheres: (c1) yolk–shell spheres; (c2) multi-shell hollow spheres. (B) SEM and TEM images of various metal oxide spherical particles: (a) dense spheres; (b) porous spheres; (c) core–shell spheres; (d and e) yolk–shell spheres; (f) hollow spheres. Panel B reproduced with permission from ref. 3. Copyright © 2007, American Chemical Society.

# 2. Synthesis methods

Metal oxide particles have been generated by using different synthetic strategies, for example, colloidal synthesis, sol–gel process, aerosol process, precipitation, hydrothermal/solvothermal synthesis, hot injection, and non-aqueous and non-hydrolytic chemistry method (e.g., solid-state reactions, solid–gas reactions). In this section we summarize the main methods for the preparation of MeO particles with spherical structures such as the hydrothermal synthesis at elevated temperatures ($>100$ °C), low temperature solution precipitation synthesis ($<100$ °C) and the spray method. The first two methods include structure defining approaches such as hard templating, soft templating, hydrolysis, Ostwald ripening and the Kirkendall effect. This section ends with a brief overview of other methods involving electrodeposition, laser irradiation or ultrasonic irradiation.

## 2.1  Hydrothermal and solution precipitation methods

The hydrothermal/solvothermal synthesis of metal oxide particles involves the use of a batch reactor at elevated temperatures (above 100 °C) and pressures. It offers a controlled environment for interactions of the salts used as metal oxide with other reactants
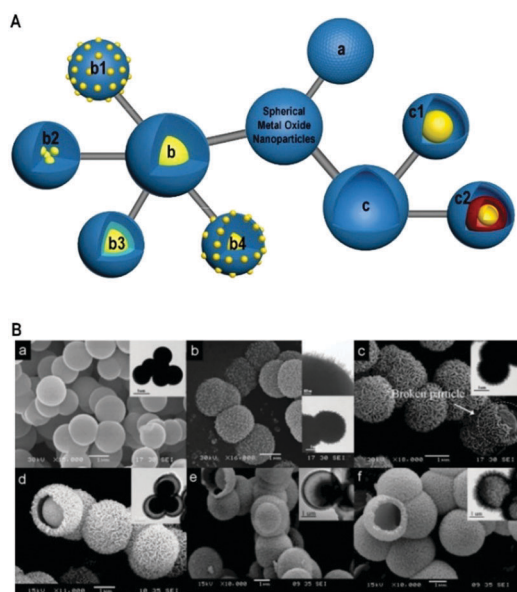
in solution to form nanosized crystallites. The elevated pressure and temperature conditions facilitate dissolution of precursors and recrystallization of materials that can be insoluble under ambient conditions. As a result, high purity, homogeneous, metastable and often crystalline products are formed with unique properties and narrow particle size distribution.[13] This synthesis method is flexible and well suited for the control of morphology and crystallinity of the porous metal oxide spheres by varying experimental parameters such as reaction temperature and time, type of reactants and solvents, and the chemical composition of the synthesis mixture. During the hydrothermal process, the nanosized crystallites self-assemble (with or without additives such as polymers and surfactants) into more complex architectures with optimal stability and lowest surface energy; hence, spherical shapes are favored. Also, metal oxide spherical structures can be synthesized *via* solution precipitation using milder conditions (*i.e.*, temperature below 100 °C and atmospheric pressure) as reported elsewhere.[13–20]

Tables 1 and 2 present the pertinent experimental conditions and characteristic features of solid spheres and shell-type particles obtained by hydrothermal synthesis together with relevant references.[21–119] As can be seen from these tables, the hydrothermal method is very popular for the synthesis of various categories of metal oxides such as alkaline earth metals (MgO), rare-earth metals ($CeO_2$, $Y_2O_3$), transition metals ($TiO_2$, $V_2O_5$, $Cr_2O_3$, $MnO_2$, $Fe_2O_3$, $Co_3O_4$, NiO, CuO, ZnO, $ZrO_2$, $Nb_2O_5$, $MoO_2$, $Ta_2O_5$ and $WO_3$) and post-transition metals ($Al_2O_3$, $Ga_2O_3$, $In_2O_3$, $Bi_2O_3$ and $SnO_2$). Composites, perovskites and doped metal oxides can also be created by controlling the ratio of the precursors.

Tables 3 and 4 provide a summary of metal oxide particles obtained by a solution precipitation method together with relevant references.[13,16–20,120–159] However, the range of metal oxide particles that can be made by this method is not as extensive as in the case of hydrothermal synthesis, probably due to the lower solubility of metal oxide precursors at lower temperatures and the smaller flexibility at the temperatures used. Nevertheless, such mild conditions are attractive in terms of green technology and cost effectiveness.

In general, metal salts are used for the synthesis of metal oxide spheres, often supplemented by complexing/structure directing agents and basic reactants in the case of precipitation method. A reducing or oxidizing agent can also be used. For instance, $NaBH_4$ was used to reduce $Co^{2+}$ into Co nanoparticles, which subsequently were spontaneously oxidized in air onto bacterial templates to form $Co_3O_4$,[14] ascorbic acid was employed to reduce $Cu(OH)_2$ to form composite $Cu/Cu_2O$ spheres under microwave hydrothermal conditions,[15] and $N_2H_4 \cdot H_2O$ was used to reduce $Cu^{2+}$ in solution to $Cu_2O$ in the reduction-induced precipitation method,[16] while oxidizing agents such as oxone monopersulfate[17] or $(NH_4)_2S_2O_8$[18,19] were employed to increase the valence states of metal cations. Moreover in some cases, metal ions were used as catalysts. For the synthesis of $MnO_2$ spheres, $Ag^+$ was used as a catalyst to help the reaction proceed at low temperature,[17,20] while in another work, $Fe^{2+}$ was used to oxidize $Mn^{2+}$ to $MnO_2$ crystals.[21]

The hydrothermal and solution precipitation syntheses are general methods that include hard templating, soft templating, hydrolysis, Ostwald ripening and the Kirkendall effect, which are briefly discussed in the following subsections.

### 2.1.1 Hard templating

*2.1.1.1 Shell structures.* Hard templating is the most common method for production of hollow spheres. In hard templating, nanoparticles are attached to the surface of a solid sphere and they aggregate to form a shell. A decade ago, the commonly used hard templates for the creation of spherical shells were carbon,[161–163] silica[164] or polymer spheres.[165] As can be seen from Tables 2 and 4 these templates are still very popular, while bio-organisms have also been used. The aforementioned templates have a large number of reactive oxygen functional groups that are electron donors and therefore attract positively charged metal cations, as depicted in Fig. 3. The size of the inner hollow space can be tailored by selecting solid templates with appropriate sizes, while the thickness of the shell can be adjusted by changing the concentration of the reactants[160] or by changing the hydrophilicity of the template's surface by alkaline or acid treatment.[141] Just recently, hollow $TiO_2$ nanospheres with a thin single layer of $TiO_2$ nanoparticles were synthesized by using quasi-nanosized carbonaceous spheres as a template.[166] In addition, hollow mesoporous organic networks (H-MONs), a new class of functional materials prepared through various carbon–carbon coupling reactions between organic building blocks, were prepared with varying shell thickness and used as templates to generate $Co_3O_4$ shells of different thicknesses and having surface areas between 60 and 67 $m^2 \ g^{-1}$.[142]

However, the use of templates does not restrict the final shape to hollow spheres. Lou and co-workers[116] found that the deposition of vanadium species on carbon sphere (CS) templates *via* a non-hydrolytic hydrothermal reaction between vanadium oxytriisopropoxide and isopropanol produced core–shell CS@V particles with shells made from interconnected nanosheets. Interestingly, when a small amount of water was added to the process, yolk–shell structures with rough surfaces were obtained. The $VO_2$ species formed by sol–gel reaction on the carbon spheres underwent an Ostwald ripening process to form a well-defined gap between the core and the shell. Yolk–shell particles of $V_2O_5@V_2O_5$ were also created from $C@V_2O_5$ core–shell particles[116] whereby the vanadium species bound to the carbon core surface would shrink into a core during annealing. Similarly, yolk–shell $ZnCo_2O_4$,[120] $SnO_2$, $CeO_2$ and $Tb_4O_7$[73] were generated by hydrothermal loading of the metal precursor into the carbon template pores followed by calcination in air. TGA studies revealed that the removal of the template occurred in two steps to give the shell first and then the core. Zeng *et al.*[167] reported the synthesis of multi-shell ZnO with single, double or triple shells by simply using carbon templates of different diameters for loading of the ZnO precursor.

Elsewhere, a penetration–solidification–annealing method was used to synthesize multi-shell spheres of $Co_xMn_{3−x}O_4$ by using carbon spheres as templates and controlling the molar ratios of Co and Mn oxide precursors.[168] Based on the anion-adsorption

Table 1  Porous solid spheres synthesized by the hydrothermal method

| Ref. | Particle type | Reactants | Solvents | Hydrothermal conditions | Calcination conditions | Particle size | BET SA (m² g⁻¹) | Pore volume (cm³ g⁻¹) | Pore size (nm) |
|---|---|---|---|---|---|---|---|---|---|
| 22 | $Bi_2O_3$ spheres | $Bi(NO_3)_3 \cdot 5H_2O$, PVP | EG | 180 °C, 0.17 h[a] | 400 °C, 3 h in air | 10 μm | NR | NR | NR |
| 23 | $Bi_2O_3$ spheres | $Bi(NO_3)_3 \cdot 5H_2O$, $HNO_3$, urea | Water, EG | 150 °C, 3 h | None | 350 nm | 8 | 0.018 | NR |
| 24 | $Bi_2WO_6$ spheres | $Na_2WO_4 \cdot 2H_2O$, $Bi(NO_3)_3 \cdot 5H_2O$, PVP K30 | Water | 180 °C, 12 h | None | 100 nm, 4 μm | 23 | 0.15 | NR |
| 25 | $Bi_2WO_6$ perovskite spheres | $Bi(NO_3)_3 \cdot 5H_2O$, $Na_2WO_4 \cdot 2H_2O$, $NaHCO_3$, citric acid | Water | 200 °C, 18 h | None | 2 μm | 24 | NR | NR |
| 26 | $CeO_2$ spheres | $Ce(NO_3)_3 \cdot 6H_2O$ | Water, $C_2H_5COOH$, EG | 180 °C, 3.3 h | None | 130 nm | 216 | NR | 3.8 |
| 27 | $Co_3O_4$ spheres | $Co(CH_3COO)_2 \cdot 4H_2O$, $NH_3$ | Water, EG | 180 °C, 12 h | 500 °C, 4 h in air | 2–5 μm | 13 | NR | NR |
| 28 | $Co_3O_4$ spheres | $Co(NO_3)_2 \cdot 6H_2O$, urea | Water | 160 °C, 6 h | 300 °C, 2 h in air | 8–20 μm | 30 | 0.245 | 17 |
| 29 | $CoFe_2O_4$ spheres | $CoCl_2 \cdot 6H_2O$, $FeCl_3 \cdot 6H_2O$, urea | Water, ethanol | 170 °C, 0.42 h[a] | 500 °C in air | 1 μm | 25 | 0.18 | 25 |
| 30 | $Cr_2O_3$ spheres | $C_{15}H_{21}CrO_6$, $NH_4HCO_3$ | Ethanol | 250 °C, 2 h | 500 °C, 4 h | 1–1.2 μm | 15 | NR | 20–80 |
| 31 | $Cr_2O_3$ spheres | $Cr(NO_3)_3 \cdot 9H_2O$, $H_2C_2O_4$, urea | Ethanol, PEG | 180 °C, 5 h | 500 °C, 2 h in air | 2–3 μm | NR | NR | NR |
| 32 | CuO spheres | $Cu(CH_3COO)_2$ | Water, EG | 160 °C, 1 h | None | 412 nm | 168 | NR | 5 |
| 33 | CuO spheres | $Cu(CH_3COO)_2$, $NH_3$, sodium alginate | Water | 160 °C, 2 h | None | 500 nm | 21 | NR | NR |
| 34 | $\alpha$-$Fe_2O_3$ spheres | $FeCl_3 \cdot 6H_2O$, ascorbic acid, urea | Water | 160 °C, 4 h | 500 °C, 4 h in air | 0.5–5 μm | 20 | 0.11 | 2–50 |
| 35 | $\alpha$-$Fe_2O_3$ spheres | $Fe(NO_3)_3 \cdot 9H_2O$ | Water, 2-butanone | 140 °C, 12 h | None | 100 nm | NR | NR | NR |
| 36 | $\alpha$-$Ga_2O_3$ spheres | $Ga(NO_3)_3$, oxalic acid | Water | 200 °C, 10 h | 450 °C, 3 h | 0.5–4 μm | 62 | 0.193 | 12.3 |
| 37 | Cubic-$In_2O_3$ spheres | $InCl_3 \cdot 4H_2O$, citric acid | Water, ethylenediamine | 180 °C, 7 h | 400 °C, 0.17 h in air | 150–200 nm | 88 | NR | NR |
| 37 | Hexagonal-$In_2O_3$ spheres | $InCl_3 \cdot 4H_2O$, tartaric acid | Water, ethylenediamine | 180 °C, 7 h | 400 °C, 0.17 h in air | 150–200 nm | 85 | NR | NR |
| 38 | $In_2O_3$ spheres | $InCl_3 \cdot 4H_2O$, urea, sodium citrate | Water, EG | 200 °C, 16 h | 400 °C, 2 h in air | 600–700 nm | 19 | NR | NR |
| 39 | $Nb_2O_5$ spheres | $NbCl_5$ | Ethanol | 200 °C, 24 h | 550 °C, 2 h in air | 200–900 nm[b] | 23–68[b] | NR | NR |
| 40 | $Nb_2O_5$ spheres | Glycolated $Nb_2O_5$ spheres[c] | Water | 180 °C, 12 h | None | 400–500 nm | 312 | 0.567 | 2 |
| 41 | NiO spheres | $Ni(NO_3)_2 \cdot 6H_2O$, $Na_2SO_4$, NaOH, glycine | Water | 180 °C, 0.5 h[a] | 300 °C, 3 h in air | 2 μm | 202 | NR | 25 |
| 42 | NiO spheres | $Ni(NO_3)_2 \cdot 6H_2O$, NaCl, sodium acetate | EG | 190 °C, 8 h | 300 °C, 2 h in air | 600 nm | 222 | NR | 4–10 |
| 2 | NiO spheres | $NiCl_2$, sodium acetate, polyethyleneimine | Water, triethanolamine | 200 °C, 8 h | 270 °C, 0.5 h in air | 500 nm | 60 | NR | 10–30 |
| 43 | NiO spheres | $NiCl_2 \cdot H_2O$, urea | Water | 100 °C, 20 h | 300 °C, 2 h in air | 3–4 μm | 200–240[d] | NR | 3.2, 8.9, 4[e] |
| 44 | La doped NiO spheres | $Ni(NO_3)_2 \cdot 6H_2O$, $La(NO_3)_2 \cdot 6H_2O$, $NH_3$, glucose | Water | 140 °C, 12 h | 550 °C, 4 h in air | 1–2 μm | 278 | 0.79 | 2–50, >50 |
| 45 | $SnO_2$ spheres | $Na_2SnO_3 \cdot 3H_2O$, sodium alginate | EG, water | 180 °C, 24 h | None | 200–400 nm | 29 | NR | 15 |
| 46 | $SnO_2$ spheres | $SnCl_2 \cdot 2H_2O$, NaClO, HCl | Ethanol | 180 °C, 12 h | None | 150 nm | 62 | NR | 4 |
| 47 | $SnO_2$ spheres | $SnCl_4 \cdot 5H_2O$, PVP | Methanol | 180 °C, 3 h | 500 °C, 2 h in air | 400–700 nm | 78 | NR | 10 |
| 48 | $SnO_2$ spheres | $SnCl_4 \cdot 5H_2O$, PVP | Methanol | 180 °C, 3 h | 500 °C, 2 h in air | 500–700 nm | 78 | NR | 10 |
| 49 | $SnO_2@C$ spheres | $K_2SnO_3 \cdot 3H_2O$, glucose | Water | 180 °C, 4 h | 450 °C, 4 h in $N_2$ | 100 nm | NR | NR | NR |
| 50 | C–$V_2O_3$ spheres | $NH_4VO_3$, citric acid | Ethanediol, water | 180 °C, 24 h | 600 °C, 3 h in $N_2$ | 2 μm | 45 | NR | 20 |
| 51 | $V_2O_5$ spheres | $VO(OiPr)_3$ | Acetic acid | 200 °C, 1.5 h | 350 °C, 0.5 h in air | 4–10 μm | 42 | NR | NR |
| 52 | $WO_2$ spheres | $W(CO)_6$ | Ethanol | 200 °C, 24 h | None | 0.7–1.5 μm[f] | 78–114[f] | NR | NR |
| 53 | $WO_3$ spheres | $WCl_6$, carbon microspheres | Dimethylformamide | 120 °C, 4 h | 420 °C, NR | 150–220 nm | 22 | 0.0447 | NR |
| 54 | $WO_3/TiO_2$ spheres | $(NH_4)_{10}H_2(W_2O_7)_6$, $TiOSO_4$, P123 | Water, ethanol | 140 °C, 16 h | 500 °C, 6 h in air | NR | 45–64[g] | 0.21–0.26[g] | 12.2–15.2[g] |
| 55 | $Eu^{3+}$:$Y_2O_3$ spheres | $Y(NO_3)_3 \cdot 6H_2O$, $Eu(NO_3)_3$, KOH | Water, 1-propanol | 400 °C[c,h], 0.17 h | 1000 °C, 1 h in air | 2–3 μm | NR | NR | NR |
| 56 | ZnO spheres | $Zn(NO_3)_2 \cdot 6H_2O$, urea | Water | 100 °C, 3 h | 300 °C, 0.5 h in air | Several μm | 194 | NR | 5 |
| 57 | ZnO spheres | $Zn(NO_3)_2$, urea | Water | 120 °C, 2 h | 450 °C, 2 h in air | 10 μm | 38 | NR | 8.67 |

This journal is © The Royal Society of Chemistry 2016

Chem. Soc. Rev., 2016, 45, 6013–6047 | 6017

**Table 1** (continued)

| Ref. | Particle type | Reactants | Solvents | Hydrothermal conditions | Calcination conditions | Particle size | BET SA ($m^2\ g^{-1}$) | Pore volume ($cm^3\ g^{-1}$) | Pore size (nm) |
|---|---|---|---|---|---|---|---|---|---|
| 58 | ZnO spheres | $Zn(NO_3)_2 \cdot 6H_2O$, trisodium citrate, urea | Water | 120 °C, 6 h | 300 °C, 2 h in air | 4–6 µm | 40 | NR | 20–60 |
| 59 | ZnO spheres | $Zn(CH_3COOH)_2 \cdot 2H_2O$, MEA, urea | Water | 120 °C, 12 h | 450 °C, 2 h in air | 1–2 µm | 40 | NR | 5–50 |
| 60 | ZnO spheres | $Zn(CH_3COO)_2 \cdot 2H_2O$, NaOH, citric acid | Water, ethanol | 120 °C, 24 h | None | 2–3 µm | 42 | NR | 2–30 |
| 61 | ZnO spheres | $Zn(CH_3COO)_2$, thiourea | Water | 180 °C, 10 h | 500 °C, 3 h in air | 3–5 µm | 21 | NR | 22.6 |
| 60 | Ag loaded ZnO spheres | $Zn(CH_3COO)_2 \cdot 2H_2O$, $AgNO_3$, NaOH, citric acid | Water, ethanol | 120 °C, 24 h | None | 2–3 µm | 37 | NR | NR |
| 62 | $ZrO_2$ spheres | $ZrOCl_2 \cdot 8H_2O$, HCl, urea | Ethanol, water | 160 °C, 2 h | None | 1–2 µm | 102 | 0.09 | 2–102 |

[a] Microwave heating. [b] By varying the concentration of $NbCl_5$, between 0.3 g and 0.5 g in 25 ml solution. [c] Prepared by an antisolvent method. [d] For nanowire-, flower- and urchin-like spheres respectively by increasing urea concentration. [e] For nanowire-, flower- and urchin-like spheres respectively. [f] For $W(CO)_6$ concentration between 4.26 mM and 28.4 mM. [g] For $WO_3/TiO_2$ between 2% and 10%. [h] Supercritical temperature. NR: not reported.

mechanism and usage of carbon spheres as templates, Wang and co-workers developed a sequential templating approach for production of multi-shell hollow spheres with different composition including ZnO, $TiO_2$, $SnO_2$, $Co_3O_4$, $\alpha$-$Fe_2O_3$, $Mn_2O_3$, $V_2O_5$, etc.[166,169–176] For example, multi-shell $V_2O_5$ hollow spheres were synthesized by a novel method involving competitive anion adsorption on carbon sphere templates followed by a Trojan catalytic combustion procedure (Fig. 4).[176] The carbon spheres were pre-treated to create a negative charge, which could facilitate adsorption of metal anions from a solution of ammonium salt. The $NH_4^+$ cations also penetrated the templates, neutralizing the negative charges and stimulating further anion adsorption. As a result, single- or multi-shell structures were formed either by using different precursor concentrations or by performing multiple adsorption processes. The method was shown to be flexible and could be extended to the synthesis of $MnO_2$, $MoO_3$, $Cr_2O_3$ and $WO_3$ multi-shell hollow spheres.

However, hard templating has a few disadvantages. An additional synthesis step is required to remove the templates, which is by either calcination in air for carbon-rich templates or alkaline or HF etching for $SiO_2$ templates. The use and subsequent removal of the solid templates represents a waste in resources, which goes against "green" processing. Furthermore, calcination can lead to the partial or full collapse of the shell architectures, while alkaline etching can implicate formation of unwanted crystalline phases, such as sodium titanate (by reacting with $TiO_2$) or impurities,[152,177] whereas HF is a very toxic chemical to deal with. Nevertheless, a recent study led to the successful synthesis of hollow spheres with sandwich-type heterostructured shells via $SiO_2$ templating, whereby hydrothermal treatment resulted in crystallization of metal oxide and simultaneous etching of $SiO_2$ in the super-hot water.[178]

Carbon templates can also be produced in situ during hydrothermal synthesis by adding glucose, sucrose or other organics to the metal oxide precursors during the one-pot hydrothermal process. For instance, this method afforded carbon-supported amorphous and crystalline $V_2O_3$ micro-spheres consisting of assembled ultrathin nanosheets of ca. 10 nm thickness by using $NH_4VO_3$ and citric acid in a mixed water and ethanediol solvent, followed by calcination in a $N_2$ atmosphere.[50] The carbon was generated by carbonization of citric acid and ethanediol, which resulted in its uniform distribution in the resulting composite having 10.6% and 8.1% of carbon in the amorphous and crystalline $V_2O_3$ respectively. Hollow spheres and multiple shells of $\alpha$-$Fe_2O_3$, $Cr_2O_3$, $Co_3O_4$, NiO and ZnO were also successfully prepared by hydrothermal heating of metal chlorides in a solution of fructose at a moderate temperature of 135 °C for 6 h, followed by calcination in air.[179] The carbonaceous core of partially dehydrated fructose contains functional groups such as –C=O and –OH that can attract positive metal ions forming a metal oxide–carbonaceous composite. In another work,[180] composite carbonaceous and $Y_2O_3$ spheres produced under hydrothermal conditions were used to generate hollow $Y_2O_3$ spheres with 1 to 4 shells by controlled calcination at different heating rates. Other multi-shell structures

**Table 2** Porous shells synthesized by the hydrothermal method

| Ref. | Particle type | Reactants | Hollowing mechanism | Solvents | Hydrothermal conditions | Calcination conditions | Particle and shell dimensions | BET SA ($m^2 g^{-1}$) | Pore volume ($cm^3 g^{-1}$) | Pore size (nm) |
|---|---|---|---|---|---|---|---|---|---|---|
| 63 | $\gamma$-Al$_2$O$_3$ hollow spheres | KAl(SO$_4$)$_2$·12H$_2$O, urea | Ostwald ripening | Water | 170 °C, 3 h | 600 °C, 2 h in air | 4–6 μm, shell thickness 700–900 nm | 149 | 0.45 | 12.3 |
| 64 | Perovskite BaZrO$_3$ hollow spheres | Ba(NO$_3$)$_2$, ZrOCl$_2$·8H$_2$O, KOH | Ostwald ripening | Water | 200 °C, 24 h | None | 160 nm, shell thickness 15 nm | NR | NR | NR |
| 65 | Bi$_2$O$_3$/Co$_3$O$_4$ hollow spheres | Bi(NO$_3$)$_3$·5H$_2$O, Co(NO$_3$)$_2$·6H$_2$O, PEG, NaAc | Ostwald ripening | EG | 180 °C, 12 h | 500 °C, 2 h in air | 2–6 μm | 46 | 0.16 | NR |
| 66 | BiFeO$_3$ hollow spheres | Bi(NO$_3$)$_3$·5H$_2$O, Fe(NO$_3$)$_3$·9H$_2$O, citric acid | Ostwald ripening | Glycerol, ethanol | 160 °C, 24 h | 500 °C, 24 h in air | 1.5 μm, shell thickness 0.2 μm | 15 | NR | NR |
| 67 | CeO$_2$ hollow spheres | Ce(NO$_3$)$_3$·6H$_2$O, HCl, citric acid | Ostwald ripening | Water | 160 °C, 24 h | 365 °C, 1.5 h in air | 2–4 μm | 56 | NR | NR |
| 68 | CeO$_2$ hollow spheres | Ce(NO$_3$)$_3$·6H$_2$O, PVP, H$_2$O$_2$, urea | Ostwald ripening | Water | 180 °C, 24 h | None | 126 nm | 21 | NR | 4 |
| 69 | CeO$_2$ hollow spheres | Ce(NO$_3$)$_3$·6H$_2$O, adipic acid | Ostwald ripening | Water, EG | 180 °C, 5 h | None | 135 nm | 145 | NR | 4 |
| 70 | CeO$_2$ hollow spheres | CeCl$_3$·7H$_2$O, H$_2$O$_2$, urea | Ostwald ripening | Water | 180 °C, 10 h | None | 300 nm, shell thickness 50 nm | 85 | 0.23 | 3–10 |
| 71 | CeO$_2$ hollow spheres | Ce(NO$_3$)$_3$·6H$_2$O, PVP | Ostwald ripening | EG, ethanol, water | 180 °C, 24 h | None | 160 nm | 66 | 0.181 | 3–30 |
| 72 | CeO$_2$ hollow spheres | CeCl$_3$·7H$_2$O, urea | Ostwald ripening | Water | 180 °C, 4 h | None | 300 nm, shell thickness 30 nm | 37 | NR | 36 |
| 73 | Yolk-shell CeO$_2$ | Ce(NO$_3$)$_3$·6H$_2$O, PVP, NH$_4$Ac·2H$_2$O | Carbon spheres | Ethanol | 180 °C, 12 h | 600 °C, 3 h in air | 180 nm | NR | NR | NR |
| 74 | Multi-yolk–shell Pd@CeO$_2$ spheres | Pd@SiO$_2$, Ce(NO$_3$)$_3$·9H$_2$O | SiO$_2$ etching | EG, CH$_3$COOH, water | 130 °C, 12 h | 350 °C, 2 h in H$_2$ | 150–200 nm | 104 | 0.078 | 2–25 |
| 75 | Co$_3$O$_4$ hollow spheres | Co(NO$_3$)$_2$·6H$_2$O, sodium citrate, HMT, sucrose | In situ carbon from sucrose | Water | 140 °C, 24 h | 500 °C, 5 h in air | Shell thickness 130 nm | 60 | NR | 7.8 |
| 76 | Co$_3$O$_4$ hollow spheres | Co(NO$_3$)$_2$ | Ostwald ripening | Glycerol, isopropanol | 180 °C, 6 h | 200 °C, 2 h in air | 1 μm | 180 | NR | 2–150 |
| 77 | CoFe$_2$O$_4$ double shell spheres | CoSO$_4$·7H$_2$O, (NH$_4$)$_2$Fe(SO$_4$)$_2$·6H$_2$O, sucrose | In situ carbon from sucrose | Water | 180 °C, 24 h | 600 °C, 2 h in air | 0.5–1.5 μm, 200–500 nm hollow core | NR | NR | NR |
| | Same as above with half sucrose concentration | | | | | | NR | 38 | NR | 30 |
| 33 | CuO hollow spheres | Cu(CH$_3$COO)$_2$, NH$_3$, sodium alginate | Ostwald ripening | Water | 160 °C, 6 h | None | 500 nm | 72 | NR | NR |
| 78 | CuO hollow spheres | Cu(NO$_3$)$_2$, urea | Ostwald ripening | Water | 180 °C, 18 h | 400 °C, 2 h in air | 4.5–6.5 μm | NR | NR | NR |
| 79 | CuO hollow spheres | Cu(CH$_3$COO)$_2$·H$_2$O | Ostwald ripening | Water | 120 °C, 24 h | None | 3.5 μm, shell thickness 1.25 μm | NR | NR | NR |
| 32 | Cu$_2$O hollow spheres | Cu(CH$_3$COO)$_2$, glucose | In situ carbon from glucose | Water, EG | 160 °C, 1 h | None | 1.5 μm, shell thickness 400 nm | 37 | NR | 50 |
| 15 | Cu/Cu$_2$O hollow spheres | Cu(Oac)$_2$·H$_2$O, PVP | Ostwald ripening | Ascorbic acid | 100 °C, 0.5 h[a] | None | 150–500 nm | 19 | 0.118 | 2–100 |
| 80 | CuO/Cu$_2$O composite hollow spheres | Cu(NO$_3$)$_2$·3H$_2$O, ethanolamine | Ostwald ripening | Water | 180 °C, 12 h | None | 1.5–3 μm | 16 | NR | NR |
| 31 | Cr$_2$O$_3$@C core shell spheres | Cr(NO$_3$)$_3$·9H$_2$O, H$_2$C$_2$O$_4$, urea | Controlled annealing | Ethanol, PEG | 180 °C, 5 h | 750 °C, 6 h in 5% Ar and 95% H$_2$ | 2–3 μm | NR | NR | NR |
| 81 | $\alpha$-Fe$_2$O$_3$ hollow spheres | FeCl$_3$·6H$_2$O | Ostwald ripening | Water, DMF, TFA | 180 °C, 24 h | None | 2 μm | 4 | NR | 65.8 |

This journal is © The Royal Society of Chemistry 2016

Chem. Soc. Rev., 2016, 45, 6013–6047 | 6019

Table 2 (continued)

| Ref. | Particle type | Reactants | Hollowing mechanism | Solvents | Hydrothermal conditions | Calcination conditions | Particle and shell dimensions | BET SA (m² g⁻¹) | Pore volume (cm³ g⁻¹) | Pore size (nm) |
|---|---|---|---|---|---|---|---|---|---|---|
| 82 | α-Fe₂O₃ hollow spheres | K₃[Fe(C₂O₄)₃] | In situ gas bubbles | Water, EG | 150 °C, 48 h | 450 °C, 3 h in air | 190 nm | 41 | NR | 4–12 |
| 83 | α-Fe₂O₃ hollow spheres | FeSO₄·7H₂O | Quasi-emulsion droplets | Water, glycerol | 145 °C, NR | None | 1 μm, shell thickness 100–200 nm | 103 | NR | <30 |
| 84 | Double-shelled α-Fe₂O₃ spheres | K₃[Fe(CN)₆], NH₄H₂PO₄ | Ostwald ripening | Water | 200 °C, 30 h | None | 350 nm, 200 nm core, 20 nm outer shell, 40 nm inner shell | 98 | NR | 11.2 |
| 85 | Fe₃O₄ hollow spheres | FeCl₃·6H₂O, NaOH, SDBS | Precursor templated | EG | 200 °C, 1.5 hᵃ | 300 °C, 1 h in N₂ | 2–4 μm | 62 | 0.131 | 10.2 |
| 86 | Fe₃O₄@TiO₂ double shelled yolk–shell spheres | Fe₃O₄@SiO₂@TiO₂, NaOH | Ostwald ripening + NaOH etching | Water | 150 °C, 24 h | None | 560 nm | 150 | 0.27 | 7.5 |
| 85 | γ-Fe₂O₃ hollow spheres | FeCl₃·6H₂O, SDBS, NaOH | Precursor templated | EG | 200 °C, 1.5 hᵃ | 300 °C, 1 h in air | 2–4 μm | 56 | 0.159 | 16.3 |
| 87 | α-Fe₂O₃ four shelled hollow spheres | Fe(NO₃)₃·9H₂O, L-histidine | Amino acid templated | Water | 180 °C, 12 h | 600 °C, 2 h in air | 3 μm | 14 | 0.07 | NR |
| 88 | γ-Fe₂O₃ hollow spheres | FeCl₃·6H₂O, NH₄F, ethylenediamine | Ostwald ripening | EG | 200 °C, 20 h | 250 °C, 5 h in air | 250 nm, shell thickness 20–40 nmᵇ | 9–19ᵇ | NR | 13.3–34.5ᵇ |
| 89 | Fe₃O₄ hollow spheres | Fe(NO₃)₃·6H₂O | Kirkendall mechanism | Glycerol, isopropanol, water | 190 °C, 12 h | 350 °C, 3 h in N₂ | 900 nm, shell thickness 10 nm | 89 | NR | 4, 5, 7 |
| 90 | α-FeOOH hollow spheres | FeSO₄·7H₂O | Quasi-emulsion | Water, glycerol | 120 °C, 24 h | None | 1 μm, varied shell thicknessᶜ | 54–97ᶜ | 0.28–0.36ᶜ | <20 |
| 91 | Perovskite LaFeO₃ hollow spheres | La(NO₃)₃·6H₂O, Fe(NO₃)₃·9H₂O, citric acid | Ostwald ripening | Water | 180 °C, 24 h | 800 °C, 2 h in air | 2–5 μm, shell thickness 40–60 nm | 49 | NR | 30–80 and 100–300 |
| 92 | β-Ga₂O₃ hollow spheres | Metallic Ga, HCl, urea | In situ gas bubbles | Acetone | 200 °C, 4 h | 700–800 °C, 2 h in air, 500–600 °C, 2 h in air | 1–2 μm | 22 | NR | 3 |
|  | γ-Ga₂O₃ hollow spheres |  |  |  |  |  | 1–2 μm | 31 | NR | 7 |
| 93 | Er doped In₂O₃ hollow spheres | InCl₃·4H₂O, Er(NO₃)₃·7H₂O | Carbon spheres | Water | 180 °C, 6 h | 500 °C, 3 h in O₂ | 300 nm, shell thickness 40 nm | NR | NR | NR |
| 94 | Rh-loaded In₂O₃ hollow spheres | In(NO₃)₃·xH₂O, RhCl₃·xH₂O, D(+) glucose monohydrate | In situ carbon from glucose | Water | 180 °C, 24 h | 500 °C, 2 h in air | 2.1 μm, shell thickness 180 nm | NR | NR | 40 |
| 95 | MgO hollow spheres | MgCl₂·6H₂O, urea | Ostwald ripening | Water, EG | 120 °C, 10 h | 450 °C, 1 h in air | 3–4 μm | 130 | 0.414 | 7 |
| 96 | MgO hollow spheres | Mg(Oac)₂·4H₂O, PVP K-30, NH₄OH | Ostwald ripening | EG | 185 °C, 5 h | 500 °C, 1 h in Ar + 1 h in air | 1 μm | 343 | 1.9 | <30 |
| 97 | MnO₂ hollow spheres | KMnO₄, SiO₂ spheres, Pluronic F127 | SiO₂ etching | Water | 150 °C, 48 h | None | 210 nm | 233 | NR | NR |
| 98 | MnO₂ hollow spheres | KMnO₄ | Hollow carbon spheres | Water | 160 °C, 5 h | None | 316 nm, shell thickness 69 nm | 30 | 0.112 | 19.4 |
| 99 | MnO₂ hollow spheres | KMnO₄, Ce(NO₃)₃·6H₂O, HNO₃ | Ostwald ripening | Water | 140 °C, 3 h | None | 3–4 μm | 29 | 0.3 | 2 |
| 100 | C@MnO₂ spheres | MnSO₄·H₂O, (NH₄)₂S₂O₈, glucose | Ostwald ripening | Water | 180 °C, 3 h | None | 1.5 μm | 142 | 0.27 | 3–4 |

6020 | Chem. Soc. Rev., 2016, 45, 6013–6047

This journal is © The Royal Society of Chemistry 2016

**Table 2** (continued)

| Ref. | Particle type | Reactants | Hollowing mechanism | Solvents | Hydrothermal conditions | Calcination conditions | Particle and shell dimensions | BET SA (m² g⁻¹) | Pore volume (cm³ g⁻¹) | Pore size (nm) |
|---|---|---|---|---|---|---|---|---|---|---|
| 101 | MoO₂ hollow spheres | MoO₃, diethylenetriamine | Ostwald ripening | Water | 200 °C, 144 h | 700 °C, 4 h in Ar | 3–5 μm | NR | NR | NR |
| 102 | MoO₂@MoO₂ yolk–shell particles | MoO₂(acac)₂^d, HNO₃ | Ostwald ripening | Isopropanol, water | 180 °C, 24 h | 350 °C, 2 h in N₂ | 1 μm, shell thickness 80 nm | 31 | NR | 3–4 |
| 103 | NiO hollow spheres | Ni(NO₃)₂·6H₂O, NH₃, L-cysteine | Ostwald ripening | Water | 120 °C, 10 h | 600 °C, 1 h in air | 2–3 μm, shell thickness 400 nm | 66 | 0.442 | 10–50 |
| 104 | NiO multi-shelled spheres | Ni(NO₃)₃·6H₂O, NH₃, D-glucose | In situ carbon from glucose | Water | 150 °C, 15 h | 500 °C, 6 h in air | 2–3.5 μm, shell thickness 50 nm | 29 | NR | NR |
| 105 | Core-in-double shell NiCo₂O₄ spheres | Ni-glycerate spheres prepared hydrothermally | Kirkendall mechanism | None | NA | 350 °C, 2 h@1 °C min⁻¹ | 400 nm outer shell, 200 nm inner shell, 40 nm core, 70 nm and 40 nm outer and inner shell thickness | 61 | NR | <10 |
| 81 | SnO₂ hollow spheres | SnCl₄·5H₂O | Ostwald ripening | Water, DMF, TFA | 180 °C, 48 h | None | 2 μm | 108 | NR | 6.04 |
| 106 | SnO₂ hollow spheres | SnSO₄ | Ostwald ripening | Water | 120 °C, 48 h | None | 100–200 nm | 69 | NR | 4 |
| 107 | SnO₂ hollow spheres | SnF₂, H₂O₂ | Ostwald ripening | Water | 180 °C, 12 h | None | 100–200 nm, shell thickness 40–50 nm | 156 | NR | NR |
| 108 | SnO₂ hollow spheres | K₂SnO₃·3H₂O, urea | Ostwald ripening | Water, ethanol | 150 °C, 24 h | None | 150–400 nm | 110 | NR | 4 |
| 109 | SnO₂ hollow spheres | SnCl₂·2H₂O, HCl, urea | Hollow polystyrene spheres | Mercaptoacetic acid | 120 °C, 6 h | 400 °C, 2 h in air | 650 nm, shell thickness 100 nm | 62 | NR | 3–8 |
| 73 | Yolk-shell SnO₂ | SnCl₂·2H₂O, HCl | Carbon spheres | DMF, water | 180 °C, 12 h | 600 °C, 3 h in air | 420 nm | 43 | 0.073 | 6.8 |
| 110 | SnO₂ multishell spheres | SnCl₄·5H₂O, sucrose | In situ carbon from sucrose | Water | 190 °C, 24 h | 600 °C, 3 h in air | 0.5–2 μm | 36 | 0.197 | 2.50 |
| 111 | SnO₂/C hollow spheres | Sn spheres, glucose | Kirkendall mechanism | Water | 180 °C, 3 h | 500 °C, 3 h in N₂ | 100 nm | NR | NR | NR |
| 108 | SnO₂/C hollow spheres | SnO₂ hollow spheres, glucose | In situ carbon from glucose | Water | 180 °C, 3 h | 550 °C, 3 h in N₂ | 150–400 nm | NR | NR | NR |
| 112 | Perovskite SrTiO₃ hollow spheres | Anatase TiO₂, SrCl₂·6H₂O, NaOH | Kirkendall mechanism | Water | 180 °C, 6 h | None | 3–5 μm, shell thickness 700 nm | NR | NR | NR |
| 113 | SiO₂–Ta₂O₅ hollow spheres^e | Tantalum isopropoxide, CTAB, TEOS, NH₃ | Ostwald ripening | Water, ethanol | 120 °C, 48 h | 550 °C, 5 h in air | 100–250 nm, shell thickness 50 nm | 249 | 0.48 | 14.8 |
| | SiO₂–Ta₂O₅ hollow spheres^f | | | | | | 200 nm, shell thickness 60 nm | 225 | 0.26 | 13.5 |
| 73 | Yolk-shell Tb₄O₇ | Tb(NO₃)₃, NH₄Ac·2H₂O | Carbon spheres | Ethanol | 180 °C, 12 h | 600 °C, 3 h in air | 200 nm | NR | NR | NR |
| 114 | V₂O₅ hollow spheres | NH₄VO₃ | In situ gas bubbles | EG | 180 °C, 24 h | 500 °C, 2 h in air | 3 μm, shell thickness 1.125 μm | 22 | NR | 5–8 |
| 115 | V₂O₅ hollow spheres | VO(C₅H₇O₂)₂, PVP | PVP micelles templated | EG | 140 °C, 12 h | 350 °C, 2 h in air | 800 nm | NR | NR | NR |
| 116 | V₂O₅@V₂O₅ yolk–shell spheres^g | Vanadium oxytriisopropoxide | Carbon spheres | Isopropanol | 200 °C, 12 h | 350 °C, 2 h in air | 1 μm, shell thickness 200 nm | NR | NR | NR |
| | V₂O₅@V₂O₅ yolk–shell spheres^h | Vanadium oxytriisopropoxide | Carbon spheres | Isopropanol, water | 200 °C, 12 h | 350 °C, 2 h in air | 2 μm, shell thickness 100 nm | NR | NR | NR |
| 117 | V₂O₅ yolk-shell spheres | V₂O₅, oxalic acid | Ostwald ripening | Water, isopropanol | 200 °C, 2.5 h | 350 °C, 2 h in air | 1 μm, shell thickness 100 nm | 28 | 0.15 | NR |
| 118 | ZnO hollow spheres | ZnCl₂, glucose | In situ carbon from glucose | Water | 180 °C, 24 h | 500 °C, 4 h | 0.8 μm | 63 | 0.17 | <5, 9–90 |

This journal is © The Royal Society of Chemistry 2016

Chem. Soc. Rev., 2016, 45, 6013–6047 | 6021

**Table 2** (continued)

| Ref. | Particle type | Reactants | Hollowing mechanism | Solvents | Hydrothermal conditions | Calcination conditions | Particle and shell dimensions | BET SA (m² g⁻¹) | Pore volume (cm³ g⁻¹) | Pore size (nm) |
|---|---|---|---|---|---|---|---|---|---|---|
| 119 | ZnO single shell hollow spheres | ZnSO₄·7H₂O, glucose | In situ carbon from glucose | Water | 180 °C, 12 h | 550 °C directly, 3 h in air | 1 μm | 10 | 0.04 | NR |
| | ZnO double shell hollow spheres | | | | | 550 °C, 5 °C min⁻¹, 3 h in air | 1 μm | 19 | 0.07 | NR |
| | ZnO triple shell hollow spheres | | | | | 550 °C, 2 °C min⁻¹, 3 h in air | 1 μm | 25 | 0.09 | NR |
| 62 | ZrO₂ hollow spheres | ZrOCl₂·8H₂O, HCl, urea | Ostwald ripening | Ethanol, water | 160 °C, 24 h | None | 1–2 μm | 136 | 0.1 | 2–105 |
| 120 | Yolk-shell ZnCo₂O₄ | ZnAc₂·2H₂O, CoAc₂·4H₂O | Carbon spheres | EG | 180 °C, 12 h | 600 °C, 3 h in air | 300–500 nm | 16 | 0.063 | 20 |

$^a$ Microwave heating. $^b$ For F/Fe fractions between 0 and 1. $^c$ By varying the fraction of glycerol in water between 0.05 and 0.125. $^d$ (acac) = $CH_3COCH=C(O-)CH_3$. $^e$ Ratio $SiO_2$:$Ta_2O_5$ = 1:0.85. $^f$ Ratio $SiO_2$:$Ta_2O_5$ = 1:1.7. $^g$ Nanosheet shell. $^h$ Porous shell. NR: not reported.

were successfully produced *via* this method such as ZnO,[119] NiO,[104] SnO$_2$[110] and CoFe$_2$O$_4$.[77] However, the metal oxide shells produced this way sometimes tend to aggregate and may be non-uniform in size.[75,110,181]

Nevertheless, hard templates could be environmentally friendly through the use of biotemplates such as yeast[139] and bacteria.[14] The utilization of bacteria (*Micrococcus lylae*) as a template to synthesize flower-like hierarchical Co$_3$O$_4$ hollow spheres with a uniform size of 1 μm, a high surface area of 149 m$^2$ g$^{-1}$ and a pore volume of 0.26 cm$^3$ g$^{-1}$ was achieved *via* a one-pot reduction/oxidation reaction at room temperature.[14] The bacterial surface is naturally covered with carboxyl, ester, amine and hydroxyl groups, which could readily capture cations. The bio-templating method is very attractive as it is facile, scalable and cost effective and could be extended to fabricate other materials and composites.

The choice of the template is important in determining the quality of the produced metal oxide nanoparticles. This has been shown when TiO$_2$ shells were prepared by coating a core with a TiO$_2$ layer followed by adding an outer protective layer around the TiO$_2$.[182] The core and the protective layer were made of either SiO$_2$ or a resorcinol–formaldehyde resin-derived carbon, which was then removed by either etching or calcination in air. It was found that better crystallization occurred with the use of resorcinol–formaldehyde resin as a template due to enhanced flexibility and volume shrinkage of the resin during carbonization, while the growth of TiO$_2$ crystals was inhibited by impregnated silicate species.

*2.1.1.2 Solid spheres.* The solid templates have been mainly used in the synthesis of metal oxide spheres for the creation of large mesopores. In this case, the metal species were infiltrated into mesoporous templates, which upon template removal created a porous spherical structure. Some reported examples are porous ZrO$_2$ spheres obtained by using the EDA-functionalized poly-(GMA-*co*-EGDMA) microspherical templates, Y$_2$O$_3$:Er mesoporous spheres fabricated by using mesoporous SiO$_2$ spheres as templates, and porous WO$_3$ spheres created by employing carbon microsphere templates.[53,132,136] In another work, Chen *et al.*[74] prepared multi-core–shell Pd@SiO$_2$@mesoporous–CeO$_2$ by assembling CeO$_2$ nanoparticles around multiple Pd@SiO$_2$ cores *via* a hydrothermal method. Once the silica was removed with concentrated NaOH, a multi-yolk–shell Pd@mesoporous–CeO$_2$ structure was obtained with a size of 150–200 nm and a BET surface area of ∼103 m$^2$ g$^{-1}$.

### 2.1.2 Soft templating

*2.1.2.1 Shell structures.* Soft templating is also a commonly used method for production of hollow spheres and yolk–shell spheres. In this method the gas–liquid, liquid–liquid or dissolved long chained organic micelles are used as soft templates for the formation and crystallization of metal oxide nanoparticles. Gas–liquid interfaces are *in situ* formed around gas bubbles that are generated during chemical reactions; for example, CO$_2$ bubbles are formed from urea, NH$_4$HCO$_3$[183] and ferric potassium oxalate[82] during decomposition at high temperatures or N$_2$ bubbles are formed from the reaction of

6022 | *Chem. Soc. Rev.*, 2016, **45**, 6013–6047

This journal is © The Royal Society of Chemistry 2016

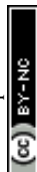Table 3  Porous solid spheres synthesized by the solution precipitation method

| Ref. | Particle type | Reactants | Solvents | Reaction conditions | Calcination conditions | Particle size | BET SA ($m^2\ g^{-1}$) | Pore volume ($cm^3\ g^{-1}$) | Pore size (nm) |
|---|---|---|---|---|---|---|---|---|---|
| 19 | $Ag_2O$-$MnO_2$ spheres | $MnSO_4$, $(NH_4)_2S_2O_8$, Ag nanoparticles | Water | 50 °C, 1 h[a] | None | 2.2 μm | NR | NR | NR |
| 121 | α-$Al_2O_3$ spheres | $Al_2(SO_4)_3 \cdot 16H_2O$, $Al(NO_3)_3 \cdot 9H_2O$, urea | Water | 98 °C, 1.5 h | 1100 °C, 1 h in air | 125–430 nm[b] | 76[b] | NR | 2–20 |
| 121 | γ-$Al_2O_3$ spheres | $Al_2(SO_4)_3 \cdot 16H_2O$, $Al(NO_3)_3 \cdot 9H_2O$, urea | Water | 98 °C, 1.5 h | 900 °C, 1 h in air | NR | 102[b] | NR | 2–20 |
| 18 | CuO spheres | Cu powder, NaOH, $(NH_4)_2S_2O_8$ | Water | 25[i] °C, 20 h | None | 1–2 μm | 8 | NR | NR |
| 122 | CuO spheres | $Cu(NO_3)_2 \cdot H_2O$, $NH_3$, NaOH | Water, glycol | 100 °C, 2 h | 300 °C, 4 h in air | 1–3 μm | 88 | NR | NR |
| 17 | $MnO_2$ spheres | $(CH3COO)_2Mn \cdot 4H_2O$, $AgNO_3$, $H_2SO_4$, oxone monopersulfate | Water | 25[i] °C, 36 h | None | 1–3 μm | 163 | NR | 65 |
| 21 | $MnO_2$ spheres | $MnSO_4$, $(NH_4)_2S_2O_8$, $FeSO_4$ | Water | 50 °C, 1.5 h[a] | None | 700 nm | NR | NR | NR |
| 20 | α-$MnO_2$ spheres | $MnSO_4 \cdot H_2O$, $K_2S_2O_8$, $K_2SO_4$, $H_2SO_4$, $AgNO_3$ | Water | 40 °C, 12 h | None | 2 μm | 150 | NR | 2, 10–20 |
| 20 | | | | 60 °C, 12 h | None | 2 μm | 106 | NR | 2, 10–20 |
| 20 | | | | 80 °C, 12 h | None | 2 μm | 83 | NR | 2, 10–20 |
| 123 | $Nb_2O_5$ spheres | $NbCl_5$, $HNO_3$, resol, PEO-b-PS diblock copolymer | THF | 50 °C, 24 h + 100 °C, 24 h | 350 °C, 3 h and 550 °C, 2 h in $N_2$ + 400 °C, 3 h in air | 0.2–1 μm | 131 | 0.26 | 11.4 |
| 124 | NiO spheres | $Ni(NO_3)_2 \cdot 6H_2O$, $NH_3$ | Water | 97 °C, 1 h | 300 °C, 2 h in air | 5 μm | 216 | 0.38 | 64.3 |
| 125 | $SnO_2$ spheres | $Na_2SnO_3 \cdot 3H_2O$, D-glucose monohydrate | Water | 50 °C, 12 h | None | 50 nm | 160 | 0.196 | 2.55 |
| 125 | | | | | 150 °C in air | 50 nm | 146 | NR | NR |
| 125 | | | | | 300 °C in air | 50 nm | 103 | NR | NR |
| 125 | | | | | 500 °C in air | 50 nm | 75 | NR | NR |
| 126 | $SnO_2$ spheres | $SnSO_4$ | Water, ethanol | 25[i] °C, 1 h | 500 °C, 2.5 h in air | 100–800 nm | 29 | NR | 4 |
| 127 | $V_2O_5$ spheres | Vanadium isopropoxide | Acetone, pyridine, water | 25[i] °C, 0.5 h | 400 °C, 2 h in $H_2$[c] + 300 °C, 1 h in air[d] | 150–1000 nm[e] | 31 | NR | <30 |
| 128 | $V_2O_5$ spheres | $NH_4VO_3$, HCl, hydrazine | Water | 25[i] °C, 0.5 h | 350 °C, 2 h in air | 400 nm | 12 | NR | <50 |
| 129 | $WO_3$ spheres | $Na_2WO_4 \cdot 2H_2O$, HCl[f] | Water, EG | 75 °C, 12 h | 450 °C, 2 h in air | 3–5 μm | 13 | NR | 3.3–5.4 |
| 130 | $WO_3$ spheres | $Na_2WO_4$, HCl, oxalic acid | Water | 25[i] °C, 1 h[a] | 500 °C in air | 1–3 μm | 13 | NR | 28.1 |
| 131 | $WO_3 \cdot H_2O$ spheres | $Na_2WO_4 \cdot 2H_2O$, HCl | Water | 70 °C, 10 h | 400 °C, 2 h in air | 2–3 μm | 11 | NR | 1.7–30 |
| 132 | $Y_2O_3$:Er spheres | Mesoporous $SiO_2$ spheres[g], $Y(NO_3)_3$, $Er(NO_3)_3$, urea | Water | 90 °C, 2 h | 700 °C, 3 h in air | 560 nm | 85 | 0.196 | 5.7 |
| 133 | $ZnCo_2O_4$@$CeO_2$ core-shell spheres | $ZnCo_2O_4$, $Ce(NO_3)_3$, hexamethylenetetramine | Water, ethanol | 60 °C, 2 h | None | 1.55–1.68 μm[h] | 34–57[h] | NR | NR |
| 134 | ZnO spheres | $Zn(CH_3COO)_2$, TEA | Water | 25[i] °C, 2 h[a] | None | 520 nm | 17 | NR | 25, 180 |
| 135 | ZnO spheres | $Zn(CH_3COO)_2 \cdot 2H_2O$, hexamine, sodium citrate | Water | 90 °C, 6 h | 600 °C in air | 2.5 μm | NR | NR | NR |
| 136 | $ZrO_2$ spheres | $ZrOCl_2 \cdot 8H_2O$, porous polymer spheres | Water, ethanol | 25[i] °C, 0.17 h[a] | 600 °C, 6 h in air | 2.6 μm | 22 | 0.17 | 31 |

[a] Sonicated. [b] When the ratio of $Al_2(SO_4)_3 \cdot 16H_2O$:$Al(NO_3)_3 \cdot 9H_2O$ is between 0.33 and 0.167. [c] To obtain $V_2O_3$ phase. [d] To obtain $V_2O_5$ phase. [e] Depending on water or pyridine concentration. [f] Mol ratio of $Na_2WO_4 \cdot 2H_2O$:concentrated HCl = 1:50. [g] Removed by NaOH etching. [h] By varying the Ce/HMT ratio. [i] Assumed room temperature. NR: not reported.

Table 4  Porous shells synthesized by the solution precipitation method

| Ref. | Particle type | Reactants (mol/mass ratios) | Hollowing mechanism | Solvents | Reaction conditions | Calcination conditions | Particle and shell dimensions | BET SA (m² g⁻¹) | Pore volume (cm³ g⁻¹) | Pore size (nm) |
|---|---|---|---|---|---|---|---|---|---|---|
| 137 | Al₂O₃ hollow spheres | Al₂O₃ spheres, PVP, NaOH | NaOH etching/Kirkendall | Water | $25^j$ °C, few minutes | 400 °C in air | 190 nm, shell thickness 23–30 nm | 292 | 0.442 | 6.3 |
| 138 | Al₂O₃, ZrO₂, ZnO shell | Metal salt | Solid core | Buffer solution | 70 °C, 2 h | 450 °C, 2 h in air | Shell thickness tunable 1–20 nm | NR | NR | NR |
| 139 | CdO hollow spheres | Cd(CH₃COO)₂, NaOH | Yeast | Water | $25^j$ °C, 12 h | 500 °C, 4 h in air | 2.3 μm, shell thickness 250–280 nm | 5 | 0.009 | 3–30 |
| 140 | CeO₂ hollow spheres | Ce(NO₃)₃·6H₂O, HMT | PS spheres | Water | 75 °C, 2 h | 600 °C, 2 h in air | 190 nm, shell thickness 15 nm | 66 | 0.19 | NR |
| 141 | Co₃O₄ hollow spheres | Co(NO₃)₂ | Untreated carbon spheres | Water | $25^j$ °C, 1 h | 450 °C, 2 h in Ar + 450 °C in air | 240 nm, shell thickness 40 nm | 223 | 0.29 | 15.3 |
| | | Co(NO₃)₂ | Acid treated carbon spheres | | | | 240 nm, shell thickness 15 nm | 301 | 0.36 | 9.9 |
| | | Co(NO₃)₂ | Alkali treated carbon spheres | | | | 240 nm, shell thickness 70 nm | 174 | 0.2 | 23 |
| 142 | Co₃O₄ hollow spheres | Co₂(CO)₈ | H-MON^a spheres | Toluene | 100 °C, 5 h | 500 °C, 5 h in air | 500 nm, shell thickness 20–80 nm^b | 64^c | 0.32^c | NR |
| 14 | Co₃O₄ hollow spheres | CoCl₂·6H₂O, NaBH₄ | Bacterial suspension^d | Water | $25^j$ °C, 12 h | None | 1 μm | 149 | 0.26 | 7.7 |
| 143 | CuO hollow spheres | CuSO₄, KOH, NH₃ | Ostwald ripening | Water | 68 °C, 24 h | None | 3–5 μm, shell thickness 500 nm | NR | NR | 1–2.2, 5–30 |
| 144 | CuO hollow spheres | Cu(CH₃COO)₂·H₂O, urea | In situ gas bubbles | Water | 80 °C, 2 h^e | None | 400–500 nm, shell thickness 45 nm | 60 | 0.104 | 3.6 |
| 145 | Gd₂O₃ hollow spheres | Gd(NO₃)₃, urea | Carbon spheres | Water, ethanol | 90 °C, 6 h | 800 °C, 2 h in air | 200–250 nm, shell thickness 20 nm | 33 | 0.17 | 10.9 |
| 146 | In₂O₃ hollow spheres | InCl₃ | Polymer spheres | C₂Cl₄ | 55 °C, 6 h | 600 °C, in air | 720 nm, shell thickness 110 nm | 329 | NR | 3 |
| | | | | | 75 °C, 6 h | 600 °C, in air | 950 nm, shell thickness 140 nm | 28 | NR | 3 |
| | | | | | 95 °C, 6 h | 600 °C, in air | 1180 nm, shell thickness 220 nm | 27 | NR | 3 |
| 147 | MnO₂ hollow spheres | MnSO₄ | CH₂Cl₂/H₂O interface | Water, CH₂Cl₂ | $25^j$ °C, 48 h | 300 °C, 2 h in air | 200–500 nm | 219 | 0.451 | 5.9 |
| 148 | NiO hollow spheres | Ni(NO₃)₂·6H₂O, urea | Sulfonated polystyrene hollow spheres | Water, ethanol | 80 °C, 12 h | 450 °C, 2 h in air | 500 nm, shell thickness 100 nm | 62 | NR | 2–4 |
| 149 | NiO hollow spheres | NiCl₂·6H₂O, (NH₄)₂C₂O₄ | Calcination of organic species | Water | $25^j$ °C, 0.67 h^e | 500 °C, 1 h in air | 1.7 μm | 32 | NR | 3–20 |
| 150 | SnO₂ hollow spheres | SnCl₂, HCl | Ostwald ripening | Water | 90 °C, 12 h | None | 100–300 nm, shell thickness 10 nm | 89 | NR | NR |
| 151 | SnO₂ hollow spheres | Tin butoxide | Microemulsion template | CTAB, hexanol, n-dodecane, methanol, water | 20 °C, 12 h | None | 15–25 nm, shell thickness 3–5 nm | 417 | NR | NR |
| 152 | SnO₂ hollow spheres | SnCl₂·2H₂O | Hollow SiO₂ spheres | None | 80 °C, 24 h | 700 °C, 2 h in air | 340 nm, shell thickness 50 nm | 46 | NR | 2–5 |
| 129 | WO₃ hollow spheres | Na₂WO₄·2H₂O, HCl^f | Ostwald ripening | Water, EG | 75 °C, 12 h | 450 °C, 2 h in air | 3–4 μm | 16 | NR | 5.4–89.6 |
| 153 | WO₃ hollow spheres with multiple shells | WCl₆ | PVA@GCP^g | Ethanol | 0 °C, 12 h | 450 °C, 1 h in air | 500 nm | 124 | 0.14 | 4.3 |
| 154 | WO₃/WO₃·H₂O hollow spheres | Na₂WO₄·2H₂O, HCl, oxalic acid | Ostwald ripening | Water, isopropyl alcohol | 80 °C, 12 h | 200 °C, 2 h in air | 2 μm, shell thickness 200 nm | 22 | 0.079 | 14.2 |

6024 | Chem. Soc. Rev., 2016, 45, 6013–6047

This journal is © The Royal Society of Chemistry 2016

**Table 4** (continued)

| Ref. | Particle type | Reactants (mol/mass ratios) | Hollowing mechanism | Solvents | Reaction conditions | Calcination conditions | Particle and shell dimensions | BET SA (m² g⁻¹) | Pore volume (cm³ g⁻¹) | Pore size (nm) |
|---|---|---|---|---|---|---|---|---|---|---|
| 155 | $Y_2O_3$ hollow spheres | $Y(NO_3)_3$, urea | Melamine formaldehyde spheres | Water | 85 °C, 3 h | 800 °C, 2 h in air | 1.8 μm, shell thickness 100 nm | NR | NR | NR |
| 156 | $Y_2O_3$:$Ln^{3+}$ hollow spheres | $Y(NO_3)_3$, $Eu(NO_3)_3$, urea | PS spheres | Water | 90 °C, 4 h | 800 °C, 2 h in air | 2.1 μm, shell thickness 70 nm | 62 | 0.313 | 20.7 |
| 157 | $Y_2O_3$:$Tb^{3+}$ hollow spheres | $Y(NO_3)_3$, $Tb(NO_3)_3$, urea | PS spheres | Water, ethyl alcohol | 85 °C, 3 h | 800 °C, 2 h in air | 1.3 μm, shell thickness 50 nm | NR | NR | NR |
| 158 | ZnO hollow spheres | $Zn(NO_3)_2 \cdot 6H_2O$, $(CH_2)_6N_4$, sodium citrate | Ostwald ripening | Water | 95 °C, 5 h | 400 °C, 2 h in air | 2 μm | 42 | NR | 5–8 |
| 159 | ZnO hollow spheres | $Zn(CH_3COO)_2$, HMT, sodium citrate | Calcination of organic species | Water | 95 °C, 3 h | 400 °C, 2 h in air | 2–3 μm | 138 | NR | NR |
| 160 | $ZrO_2$ hollow spheres | $ZrOCl_2 \cdot 8H_2O$, $NH_3$ vapour | PSA[h] spheres | Ethanol | 50 °C, NR | 700 °C, 4 h in air | 3.2–3.4 μm, shell thickness 80–200 nm[i] | NR | NR | NR |

[a] Hollow-microporous organic network (H-MON). [b] By varying the solvent ratio or the $SiO_2$ amount. [c] For H-MON prepared with the ratio of toluene : triethylamine = 1 : 1. [d] *Micrococcus lylae*. [e] Sonicated. [f] Mol ratio of $Na_2WO_4 \cdot 2H_2O$ concentrated HCl = 1 : 15. [g] Polyvinylalcohol@glucose derived carbon rich polysaccharide spheres. [h] Poly(styrene-acrylic acid). [i] When the molar ratio of $ZrOCl_2 \cdot 8H_2O$: ethanol is between 0.011 and 0.032. [j] Assumed room temperature. NR: not reported.
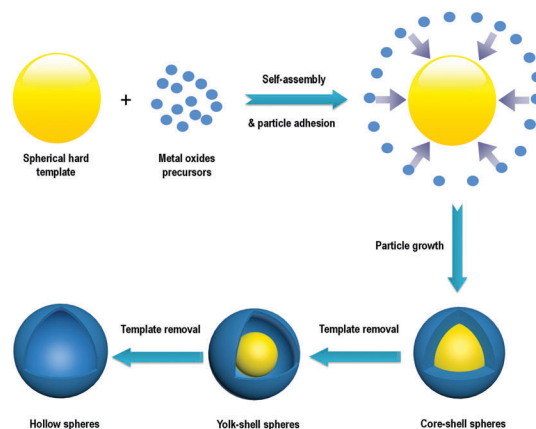


**Fig. 3** Hard templating method for synthesis of hollow metal oxide spheres.

$NH_4VO_3$ with EG.[114] Nevertheless, the hollowing of structures on gas bubbles is difficult to prove and it could be more likely that Ostwald ripening is responsible for the generation of hollow spheres.

A liquid–liquid interface occurs between immiscible liquids such as water and oil. Hierarchical mesoporous $MnO_2$ spheres were formed at the droplet interface between $CH_2Cl_2$ and $H_2O$.[147] Similarly, $SnO_2$ hollow spheres were prepared in a water-in-oil microemulsion of CTAB–hexanol-$n$-dodecane–methanol–water.[151] The calcined $SnO_2$ particles had a surface area of 119 m² g⁻¹. In another work, a mixture of TBOT and PS in toluene was emulsified in formamide containing the triblock polymer Pluronic P123.[184] After removal of toluene and PS spheres *via* heat treatment, macroporous $TiO_2$ spheres of sizes between 500 nm and 2000 nm were obtained. Finally, a glycerol, water and Fe oxide precursor mixture was hydro-thermally heated at 145 °C to obtain mesoporous α-$Fe_2O_3$ *via* a quasi-emulsion templating mechanism. The product had a surface area of 103 m² g⁻¹ when using a glycerol/water volume ratio of 1 : 7;[83] however a different phase of α-FeOOH[90] was produced at 120 °C.

A long-chained polymer such as PVP K30 ($M_w \sim 40\,000$) can form micelles in solution with a hydrophobic core and a hydrophilic shell. These micellar structures were used as soft templates to attach vanadium species and upon calcination to form uniform $V_2O_5$ hollow spheres with sizes of ~800 nm[115] and with exposed [110] facets, as shown in Fig. 5. During the formation of hollow spheres, VO(acac)$_2$ accumulated on the hydrophilic PVP micelles in the EG solvent to form VO(acac)$_2$@PVP core–shell particles. The $C_5H_8O_2$ ligand sub-sequently was replaced by EG to form VEG, which oligomerized *via* the LaMer process into a tight layer on the surface of micelles. Upon calcination, $V_2O_5$ hollow spheres were formed. On the other hand, α-$Fe_2O_3$ with multi-shell morphology of ~3 μm in size and with a surface area and pore volume of 14 m² g⁻¹ and 0.07 cm³ g⁻¹, respectively, was obtained with the ʟ-histidine amino acid as a template.[87] The Fe(OH)$_3$–ʟ-histidine–$H^+$–$NO_3^-$ complex obtained under hydrothermal conditions underwent size shrinkage and phase separation during the

This journal is © The Royal Society of Chemistry 2016

*Chem. Soc. Rev.*, 2016, **45**, 6013–6047 | 6025
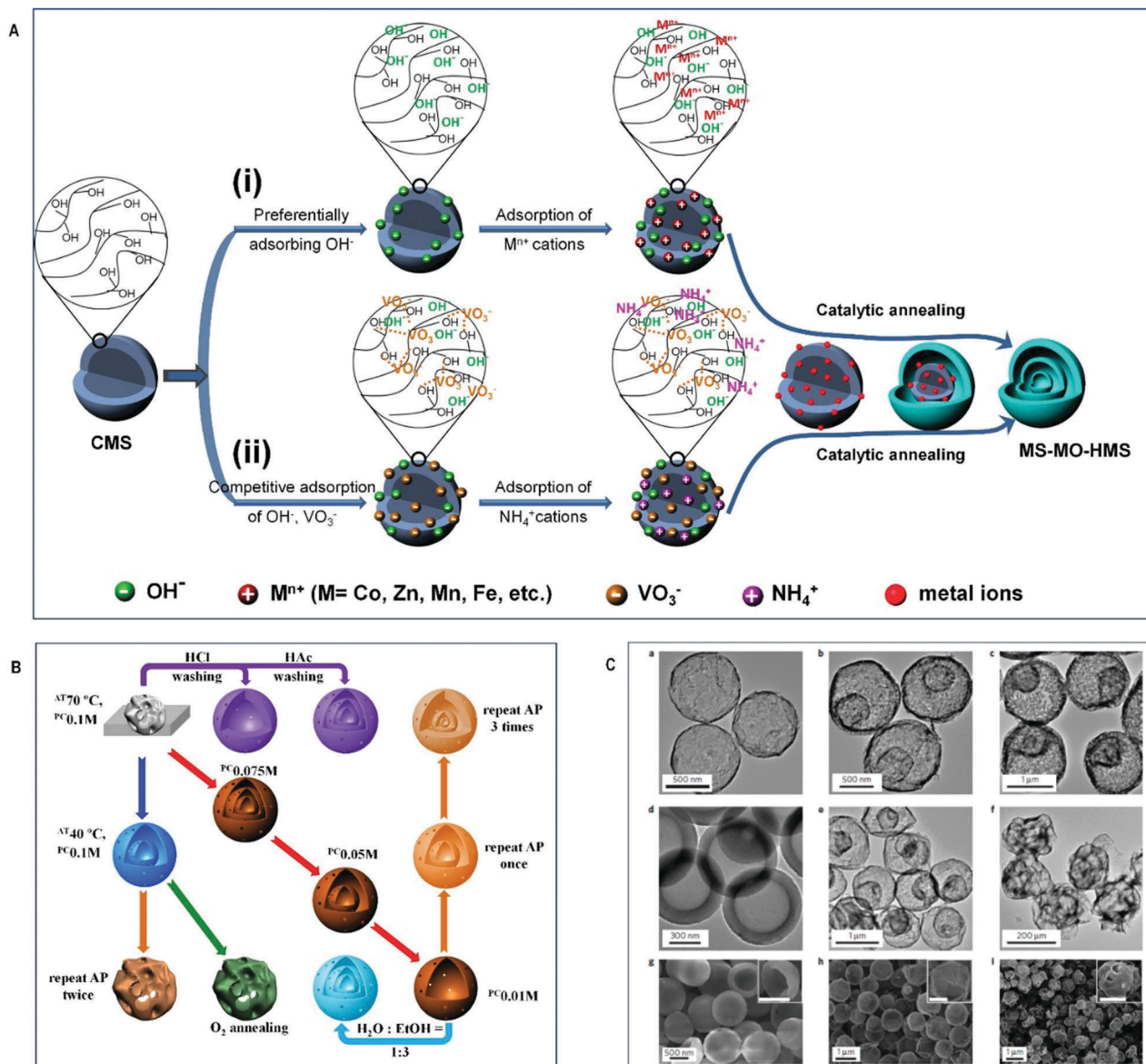
Fig. 4  Multi-shell metal oxides prepared *via* an anion-adsorption mechanism: (A) schematic representation of two synthesis routes to obtain multi-shell hollow microspheres. (i) Cation-adsorption process. (ii) Anion-adsorption process. (B) Effects of synthesis conditions on the morphology of products. (C) Morphological and structural analysis of $V_2O_5$ spheres: (a–f) TEM images of the as-prepared samples. (g–i) SEM images of the as-prepared samples. Reproduced with permission from ref. 176. Copyright © 2016, Nature Publishing Group.

calcination stage to form porous multi-shell particles. In another work,[97] a double templating method was employed by decorating soft micelles of the F127 copolymer onto $SiO_2$ spheres to obtain $MnO_2$ hollow particles following hydrothermal treatment of the template with $KMnO_4$. The morphology and surface area could be varied from urchin-like (233 $m^2$ $g^{-1}$) to flower-like (201 $m^2$ $g^{-1}$) and non-hierarchical (120 $m^2$ $g^{-1}$) by varying the F127/$SiO_2$ mass ratio to 0.2, 0.4 and 0.6 respectively.

*2.1.2.2 Solid spheres.* In the synthesis of metal oxide spheres, long chained organics are mostly used as soft templates for surface stabilization of building blocks. These organics accumulate on the nanocrystallites favoring their growth in certain directions or planes, which affects the spatial orientation of crystal nanoparticles and growth of hierarchical structures. Eventually, the removal of these organics by calcination frees hidden pores in the assembled metal oxide structures. Some examples of the organic compounds used as structure directing agents are amino acids such as L-asparagine[56] and glycine,[41] sugars such as D-glucose monohydrate,[125] carbohydrates such as starch[185] and polymers such as sodium alginate,[33,45] polyethyleneimine[2] and also PVP, which has been commonly employed.[22–24,47,48] To avoid unnecessary use of polymers and surfactants, alcohols and carboxylic acids have been proved to be very competent capping/ structure directing agents by chelating with metal ions. Moreover when mixed together, they react at elevated temperatures to produce esters, which can further influence the growth rate and self-assembly process of nanocrystallites.[26,69]
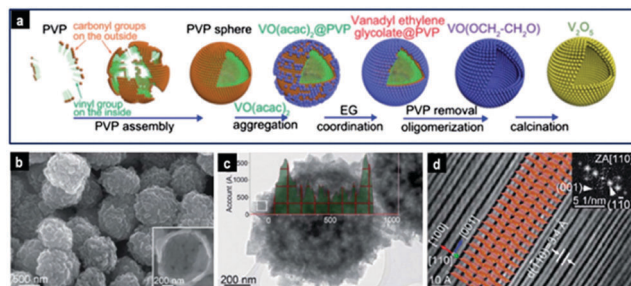
**Fig. 5** Hierarchical orthorhombic $V_2O_5$ hollow nanospheres prepared via soft-templating: (a) schematic illustration of the evolution of $V_2O_5$ hollow nanospheres. (b) FESEM and (c) TEM images of $V_2O_5$ nanospheres; (d) atomic resolution HRTEM image, from which the interlayer structure of $V_2O_5$ was directly observed. Reproduced with permission from ref. 115. Copyright © 2014, Royal Society of Chemistry.

Some researchers have used micelles to create mesoporous structures. Luo et al.[123] examined a resol-assisted solvent evaporation method in the presence of THF, PEO-b-PS block copolymer and $NbCl_5$. Upon evaporation of THF, the block copolymer aggregated into cylindrical micelles covered by the resol/$Nb^{5+}$ composite. Upon further evaporation, the micelles tended to bend and aggregate into spherical particles, while resol was acting as a binder. Subsequent pyrolysis and calcination produced $Nb_2O_5$ spheres of diameter 0.2–1 μm having uniform mesopores with an average size of 11.4 nm, a high surface area of 131 $m^2\,g^{-1}$, and a pore volume of 0.26 $cm^3\,g^{-1}$. This solvent evaporation-driven self-assembly was also recently used to create mesoporous $TiO_2$ microspheres with [101] exposed facets from spherical composite micelles consisting of PEO–PPO–PEO and titania oligomers.[186] Similarly, surfactants such as Pluronic P123, due to its long hydrophobic chains, can be used to create large mesopores between 12 and 15 nm in the $WO_3$/$TiO_2$ composite spheres.[54] Elsewhere, Wang's group[187] used a water in oil system in the presence of acrylamide and azobisisobutyronitrile to synthesize hierarchically mesoporous hematite microspheres with high surface area and bimodal structure with mesopores of 2.5 nm and 9 nm.

**2.1.3 Sol–gel and controlled hydrolysis.** The sol–gel process is a viable method for the synthesis of metal oxides from alkoxides such as butoxides, ethoxides and isopropoxides. Alkoxides vigorously react with water molecules in the presence of an excess of alcohol and ammonia as catalyst to form an inorganic network or gel of a polymer-like metal oxide that condenses into particles shown in Fig. 6. Titanium alkoxides such as titanium butoxide and titanium isopropoxide and

halides such as $TiCl_4$ are very well known and commonly used precursors for the synthesis of $TiO_2$ spheres. Because of the nature of these $TiO_2$ precursors, the reaction can be controlled by adding a small amount of water. Some of the techniques used to control the amount of water are discussed in the previous section.

Controlled hydrolysis has been used to prepare $TiO_2$ spheres,[188–196] core–shell,[197] yolk–shell,[198,199] and hollow[177,183,200–204] particles. A more detailed discussion on the synthesis of $TiO_2$ has been presented elsewhere; the reader is encouraged to refer to a comprehensive review on the synthesis of spherical $TiO_2$ nanostructures by Chen et al.[5]

Nevertheless, other types of metal alkoxides have also been used to produce the respective oxides, such as vanadium oxiisopropoxide,[51,116] vanadium(v) oxytriisopropoxide[127] and tin tert-butoxide.[151] As shown in Fig. 7, $V_2O_5$ mesoporous spheres were synthesized at room temperature by reacting vanadium isopropoxide in a mixture of acetone, pyridine and water at a volume ratio of 983 : 500 : 1.[127] The average size of the particles was tuned between ∼1 μm and ∼150 nm by increasing the amount of water while maintaining the ratio of pyridine/acetone. The reduction of particle size with increasing water content was attributed to the increased number of sites for nucleation of particles.

Silica supported $Ta_2O_5$ ($SiO_2$–$Ta_2O_5$) composite shells were produced by sol–gel synthesis using TEOS, tantalum isopropoxide, CTAB, $H_2O$, $NH_3$ and ethanol.[113] $NH_3$ catalyzed the reaction but also assisted in the dissolution of cores at higher temperature. The diameter and shell thickness were tuned by changing the molar ratio of Si : Ta. The BET surface area of the calcined particles increased from 225 to 610 $m^2\,g^{-1}$ with increasing Ta content.

The sol–gel method can be also used to manufacture templates for the synthesis of hollow and porous spheres. The one-pot sol–gel polymerization of formamide–resorcinol was employed to create vesicle templates for the synthesis of hollow $In_2O_3$ spheres,[205] while the porosity in $SnO_2$ spheres was created upon removal of the carbon template from composite Sn–resorcinol–formaldehyde resin particles.[206]

**2.1.4 Ostwald ripening.** According to the IUPAC's terminology, the process of Ostwald ripening refers to "the growth of larger crystals from those of smaller size which have higher solubility than the larger ones".[207] As can be seen from Tables 2 and 4 the Ostwald ripening represents the major process of hollowing particles under hydrothermal conditions. Once a metal oxide amorphous precursor is formed, crystallization proceeds with
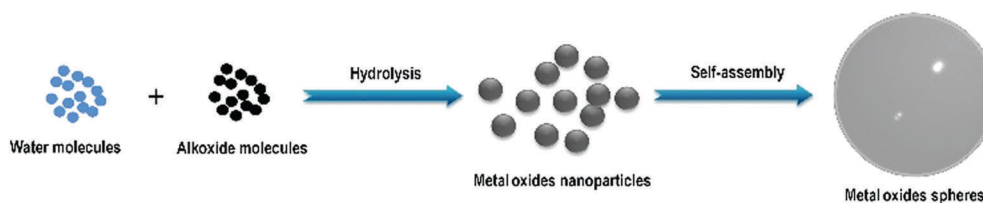


**Fig. 6** Schematic illustration of the formation of metal oxide spheres by a sol–gel process.
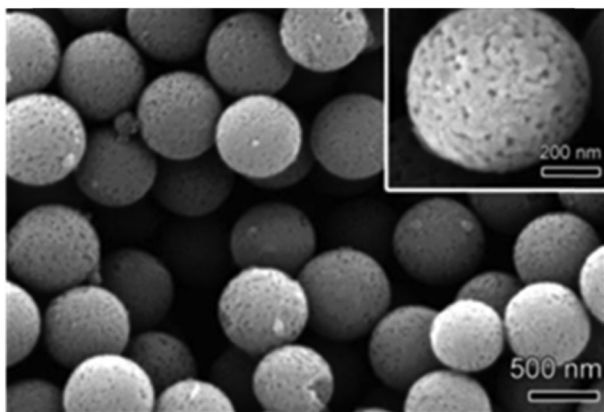
Fig. 7 SEM image of the V$_2$O$_5$ porous microspheres; the inset shows the porous structure of a single sphere. Reproduced with permission from ref. 127. Copyright © 2011, Royal Society of Chemistry.

increasing time; namely, smaller nanocrystals from the central core dissolve and recrystallize into loosely packed crystallites at the surface of spheres that act as seeds. The resulting void enlarges until a hollow structure is obtained, as shown in Fig. 8a. For example, flower-like hollow MgO spheres having a size of about 1 μm, cavities of ~500 nm, a high surface area of 343 m$^2$ g$^{-1}$ and a pore volume of 1.9 cm$^3$ g$^{-1}$ were fabricated by ripening magnesium glycolate under hydrothermal conditions.[96]

In some cases, due to the localized Ostwald ripening around a dense core, an intermediate yolk–shell architecture is formed (Fig. 8b), as in the case of MoO$_2$@MoO$_2$,[102] CeO$_2$@CeO$_2$,[70] SnO$_2$@SnO$_2$,[106] TiO$_2$@TiO$_2$[208] and V$_2$O$_5$@V$_2$O$_5$,[117] which subsequently is converted to a multi-shell structure having 2–3 shells after a prolonged hydrothermal process, and finally to hollow spheres. Similarly, double-shell CoO and Co$_3$O$_4$,[209] double-shell α-Fe$_2$O$_3$,[84] as well as perovskite-type BaZrO$_3$@BaZrO$_3$[64] and LaFeO$_3$@LaFeO$_3$[91] structures were obtained. In a different work, Li et al.[86] found that the two interfaces created by hydrothermal etching of silica from Fe$_3$O$_4$@SiO$_2$@TiO$_2$ in 1 M NaOH at 150 °C for 24 h allowed for the dissolution of TiO$_2$ crystals and their subsequent growth in an opposite direction to eventually form Fe$_3$O$_4$@TiO$_2$ double-shell spheres with flower-like morphology and with a uniform size of ~560 nm and a high surface area of 150 m$^2$ g$^{-1}$. Ostwald ripening involving selective etching of crystals is favored in basic and acidic solutions and it is apparent from Tables 2 and 4
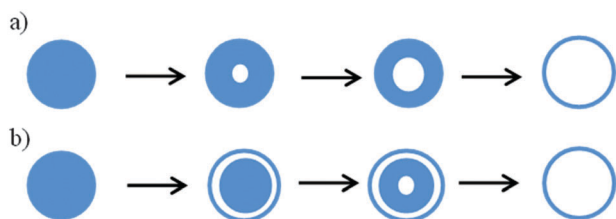
that bases such as urea, KOH, NaOH and amines or acids such as HCl, HNO$_3$ and other organic acids facilitate this process.

**2.1.5 Kirkendall effect.** The Kirkendall effect is an atomic diffusion phenomenon that occurs at elevated temperatures between two species separated by an interface (solid–solid, solid–liquid or solid–gas) and having different diffusion rates. The net directional flow of matter is balanced by an opposite flux of vacancies, which can result in the formation of voids, normally at the interface because of its high energy and defect density. Consequently, the Kirkendall effect has been utilized for the preparation of hollow nanocrystals,[210] yolk–shell particles[211] as well as metal oxide hollow spheres.[111,112,212,213] Fig. 9 shows the formation of a shell by the exchange of ions between the solid core and its surrounding.

The thermal treatment in air of a film decorated with the Cu(II) complex showed that the bulk diffusion of atoms/ions at the Cu–O interface gave Cu$_2$O-rich and CuO-poor spheres at 200 °C.[212] As the temperature increases, the Cu from the core moves outwards through the oxide shell to react with oxygen, leaving a hollow space (since the outward diffusion of Cu ions is much faster than the inward diffusion of O ions) until a hollow sphere of pure CuO is formed at 400 °C. Core-in-double-shell hollow NiCo$_2$O$_4$ spheres were obtained by slow annealing of NiCo–glycerate spheres in air due to a combination of the Kirkendall effect and the contraction and adhesion forces during the oxidative degradation of organic species.[105] This method can also be extended to the synthesis of ZnCo$_2$O$_4$ and CoMn$_2$O$_4$ with complex interior structures.

The Kirkendall effect can also occur during the hydrothermal reaction stage. The reaction of TiO$_2$ microspheres with a solution of strontium chloride hexahydrate at 180 °C for 6 h generated perovskite-type SrTiO$_3$ hollow spheres having a size of 3–5 μm and a shell thickness of ~700 nm.[112] With the assistance of NaOH, the Ti–O–Ti bonds can be broken to form Ti–O–Na on the surface of the sphere. Then, the Sr$^{2+}$ ions can react with the sodium titanate to form a thin layer of SrTiO$_3$ shell, separating the inner TiO$_3^{2-}$ ions from the Sr$^{2+}$ ions in solution. Hence, the concentration gradient between these two types of ions permitted TiO$_3^{2-}$ to diffuse out and the Sr$^{2+}$ ions to diffuse in through the shell, resulting in hollow SrTiO$_3$ spheres. Additionally, composite SnO$_2$–C hollow spheres were prepared by Wu et al.[111] under hydrothermal conditions by reacting Sn spheres in a solution of glucose at 180 °C.

Interestingly, a simple solution route by mixing hydrothermal carbon spheres in a solution of KMnO$_4$ at room temperature produced MnO$_2$ spheres of different morphologies.[214] Solid MnO$_2$ spheres were produced with 100 ml of 25 g L$^{-1}$ KMnO$_4$, C@MnO$_2$ yolk–shell spheres were obtained with 100 ml of 2.5 g L$^{-1}$ KMnO$_4$ and finally MnO$_2$ hollow shell spheres were



Fig. 8 Ostwald ripening initiated by dissolution of the middle core (panel a), and localized Ostwald ripening (panel b).



Fig. 9 Hollowing by the Kirkendall effect.

6028 | Chem. Soc. Rev., 2016, 45, 6013–6047

This journal is © The Royal Society of Chemistry 2016

obtained with 200 ml of 2.5 g $L^{-1}$ $KMnO_4$ solution. The formation of different morphologies was achieved due to different stages of the Kirkendall effect occurring through the soft surface of the hydrothermally synthesized carbon spheres by varying $MnO_4^{-}$ concentration.

The Kirkendall mechanism provides a pathway for the selective etching of the surface-protected metal oxides to produce hollow structures. For instance, the PVP-protected $TiO_2$ solid spheres were selectively etched by fluoride ions to form hollow or yolk–shell $TiO_2$.[215] Similarly, it was also reported that NaOH and HCl were used to etch the PVP-protected colloidal $Al_2O_3$ and ZnO into hollow spheres, respectively.[137]

It is apparent that during the Kirkendall mechanism, a solid core acts as a sacrificial template by reacting with its surrounding environment to form different hollow structures. This method could therefore be extremely useful to synthesize a variety of complex hollow compounds and composites from various solid templates.

## 2.2 Spray method

Spray methods include electrospray ionization[216–219] and gas phase processes such as aerosol[220–225] and flame or ultrasonic spray pyrolysis (USP).[226–229] These methods use high temperatures to evaporate the liquid from the colloidal precursor solution released by the spray nozzle to form solid or hollow spherical structures. Several types of metal oxides such as $CeO_2$ spheres,[216] $TiO_2$ spheres,[217] $WO_3$ spheres,[228] ZnO spheres,[221,225] $\alpha$-$Fe_2O_3$ microspheres,[230] CuO hollow spheres,[222] $Mn_3O_4$ hollow spheres,[224] $WO_3$ hollow spheres,[226] hollow $TiO_2$ and $ZrO_2$ spheres,[223] $TiO_2$ core–shell particles,[218] $Bi_2WO_6$ spheres,[229] $Fe_3O_4$–carbon composite spheres,[220] $Li_2O$–CuO–$SnO_2$ multi-deck cage-type spherical composites[219] and $\alpha$-$Fe_2O_3$ multi-shell hollow spheres[231] have been produced via the spray method. Some morphologies including porous spheres,[221] hollow spheres,[222,223] yolk–shell spheres,[232] yolk–multi-shell spheres,[233] and "ant-cave" spherical structure[234] are shown in Fig. 10.

In the electrospray method, the liquid is evaporated via the potential difference between the nozzle and the metal receptor, while in the gas phase processes, the colloids pass through a flame or horizontal furnace (Fig. 11). Kang and co-workers have published numerous works on spray pyrolysis for the synthesis of hollow spheres, yolk–shell particles, multi-shell spheres and porous microspheres. Hollow $WO_3$ spheres with thin and porous shells were produced by USP using citric acid as the carbon source.[226] Multi-shell structures were created from the precursor dissolved in sucrose solution. During decomposition, a dense carbon–metal oxide composite was formed, which upon further heating resulted in contraction and combustion of the carbon to form the multi-shell structures. This method was used to prepare yolk–shell $TiO_2$ and composite multi-component systems (composed of up to 5 components including $TiO_2$, $Al_2O_3$, $ZrO_2$, $CeO_2$ and $Y_2O_3$),[232] double-shell $LiNi_{0.5}Mn_{1.5}O_4$ particles,[235] Pd loaded double-shell $SnO_2$ particles[233] and double-shell $SnO_2$ spheres.[234] Alternatively, the spray-pyrolysis method has been extended to the synthesis
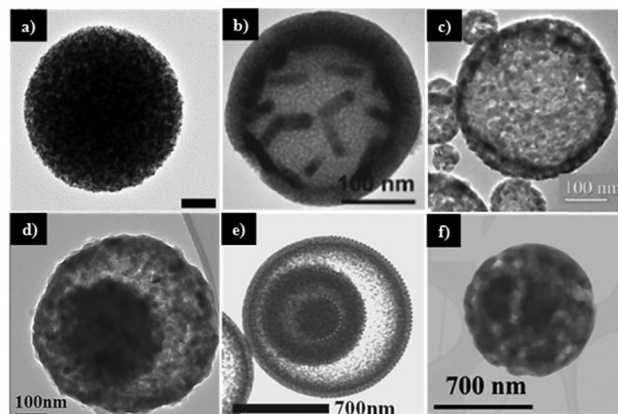


Fig. 10 Different types of metal oxide structures prepared by the aerosol method: (a) porous sphere (reproduced with permission from ref. 221; Copyright © 2014, Royal Chemical Society); (b) hollow sphere loaded with nanometals (reproduced with permission from ref. 223. Copyright © 2013, Wiley); (c) hollow shell (reproduced with permission from ref. 222. Copyright © 2013, Wiley); (d) yolk–shell sphere (reproduced with permission from ref. 232. Copyright © 2013, Wiley); (e) yolk–multi-shell sphere (reproduced with permission from ref. 233. Copyright © 2013, Wiley); and (f) "ant-cave" spherical structure (reproduced with permission from ref. 234. Copyright © 2013, American Chemical Society).
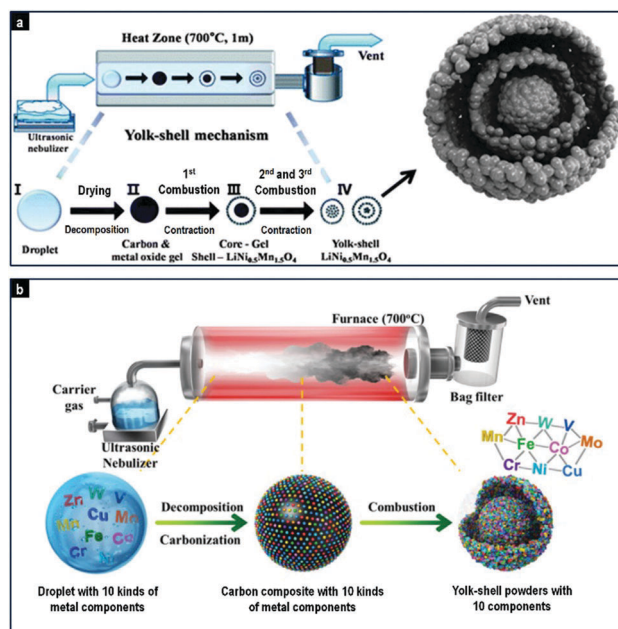


Fig. 11 Spray pyrolysis for the formation of yolk–shell-structured $LiNi_{0.5}Mn_{1.5}O_4$ spheres (panel a; reproduced with permission from ref. 235. Copyright © 2013, Royal Chemical Society) and yolk–shell ten-component transition metal oxide powder (panel b; reproduced with permission from ref. 236. Copyright © 2014, Royal Chemical Society).

of yolk–shell structured metal oxide with 10 kinds of metal components in one step as shown in Fig. 11b.[236] The method could also be modified to produce metal sulfide multi-shell spheres. $SnO_2$ yolk–double shell spheres were indeed treated with $H_2S$ gas to produce SnS yolk–double shell spheres.[237] Another work reported the synthesis of a new structured

This journal is © The Royal Society of Chemistry 2016

Chem. Soc. Rev., 2016, 45, 6013–6047 | 6029

material named "ant-cave microball", where polystyrene nanobeads were used as templates to create $MoO_3$–C composite spheres.[234] The decomposition of these nanobeads resulted in unique morphology of porous composite spheres with nanochannels, effectively resembling an ant-cave.

ZnO spheres were synthesized *via* an aerosol method using an organometallic precursor dissolved in toluene and Brij 58 as the structure directing agent.[221] The ZnO spheres had a BET surface area, crystal size and maximum pore volume of 61 $m^2$ $g^{-1}$, 8.6 nm and 13 nm, respectively. Al and S could be easily incorporated into the ZnO matrix by adding similar organometals into the precursor solution. Unfortunately, the dopants reduced the crystal size and hence the maximum pore size of the resulting ZnO spheres but this could be counteracted by using the triblock copolymer P123. Recently, very high surface area $\alpha$-$Fe_2O_3$ microspheres with an average size of 560 nm, a BET surface area of 301 $m^2$ $g^{-1}$ and an average pore size of 2.1 nm were synthesized by USP using $Fe(NO_3)_3$ and $Na_2CO_3$ as precursors.[230] The average particle size could be tuned by changing the concentration of the precursors.

Hollow or macroporous structures could be synthesized by using hard templates,[223,228] furnace synthesis at elevated temperatures,[225] *in situ* bubble reactions[222,224] or non-equilibrium air calcination.[231] Au nanorods, Pd nanocubes and Au core/Pd shell nanorods were successfully introduced into hollow $TiO_2$ and $ZrO_2$ spheres by initially embedding these nanometals in PS nanospheres. The PS spheres were dispersed in solution containing metal alkoxides and then sprayed by using $N_2$ through a tube furnace. Subsequently, calcination was performed to remove the PS template, leaving hollow $TiO_2$ and $ZrO_2$ spheres of average diameters of 0.8 μm and 0.6 μm, respectively, and containing nanometals inside the hollow space. In another work,[225] ZnO spheres of various shapes were produced simply by changing the furnace temperature. Amorphous porous spheres were obtained between 40 °C and 100 °C, solid spheres at 400 °C, yolk–shell spheres at 600 °C and hollow spheres with different crystallite sizes between 700 °C and 1200 °C. The hollowing process was induced by the Kirkendall effect. An interesting *in situ* bubble hollowing method was devised by Jian *et al.*[222] to prepare hollow CuO spheres by adding sucrose and $H_2O_2$ to $Cu(NO_3)_2$ solution. The decomposition of the sucrose into $CO_2$ and $H_2O$ (with $H_2O_2$ acting as a catalyst) within the aerosol at high temperature inflated the spheres like balloons to produce particles with an average size of ∼85 nm and very thin walls of 5–10 nm. The same strategy was used to prepare hollow $Mn_3O_4$ spheres.[224] $\alpha$-$Fe_2O_3$ multi-shell hollow spheres[231] were synthesized by spray drying a mixture of Fe(III) citrate and sucrose. The obtained Fe(III)–sucrose composite was then calcined in air to remove the carbon template. From the effect of non-equilibrium heating in air, the number of shells could be varied between 2 and 4 by simply changing the Fe(III) citrate/glucose ratio between 0.25 and 1.5.

The spray method is a simple and continuous process with a short residence time (a few seconds) of particles at a high temperature, which produces high purity products and can be easily implemented on an industrial scale. Moreover, other constituents can be included in the precursor solution allowing the preparation of composite or doped metal oxide particles. However, due to the low residence time of the particles at high temperature, further annealing may be required to improve the crystallinity of the products. Furthermore, the method has not yet been able to create hierarchical structures and the surface areas of the particles are often in the low to moderate range.

## 2.3 Other methods

Besides the methods presented above, there are a variety of other routes for the preparation of colloidal metal oxide structures such as template- and solvent-free methods, ultrasonic irradiation- and microwave-assisted syntheses, electrodeposition, direct printing, and methods involving lasers or taking advantage of gas–liquid diffusion.

A template- and solvent-free method was devised by Wang *et al.*[238] for the synthesis of hierarchical metal oxide spheres (HMOS) of $TiO_2$, $Fe_2O_3$, $ZrO_2$ and their composites. This method involves grind milling of the metal oxides in the presence of PEG and some water to create a paste, which was spread into a film and annealed. The process generated microspheres *via* PEG modification and self-assembly and has great potential for large scale production of HMOS.

During ultrasonic irradiation, the formation and collapse of bubbles in the aqueous phase results in localized extremely high temperatures ($>5000$ K), high pressures ($>20$ MPa) and very high cooling rates ($10^{10}$ K $s^{-1}$), which can supply enough energy to drive the formation of spherical metal oxide structures.[144] Various metal oxide spherical particles such as ZnO hollow nanospheres of size ∼80 nm,[239] mesoporous NiO hollow spheres,[149] $MnO_2$ spheres made of interconnected nanoflakes,[21] ZnO spheres with bimodal pores at 25 nm and 180 nm,[134] CuO hollow spheres,[144] composite $Ag_2O$–$MnO_2$ spheres with $Ag_2O$ residing at the end of $MnO_2$ nanowires,[19] and $WO_3$ spheres[130] were synthesized that way.

The electrodeposition method was used to prepare uniformly distributed 100–500 nm sized $MnO_2$ spheres with a very high surface area of 129 $m^2$ $g^{-1}$ and mesopores in the range of 5–12 nm, which were composed of randomly oriented nanorod-like structures.[240] This synthesis is inexpensive, operates at room temperature and the deposition potential is an extra parameter that can be varied to achieve different morphologies. However, the synthesized oxides have low crystallinity and require further annealing. Other examples of particles prepared *via* electrodeposition are $Y(OH)_3$ and $Y_2O_3$ nanospheres,[241] $Co_3O_4$ hollow spheres deposited on PS spheres and organized into a close-packed monolayer array[242] and $SnO_2$ spheres.[243]

The microwave-assisted synthesis is analogous to the hydrothermal method but offers a much faster heating rate of the solution. An enormous advantage of this method is the very short time which is reduced to minutes instead of hours (as shown in Tables 1 and 2) as compared to the hydrothermal method. Some examples of metal oxides prepared by this method are $Fe_3O_4$ and $\gamma$-$Fe_2O_3$ hollow spheres,[85] NiO spheres[41]

and hollow spheres[244] with very high surface areas reaching 200 m² g⁻¹, TiO₂ spheres[195,245] and Bi₂O₃ spheres.[22]
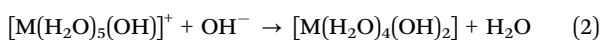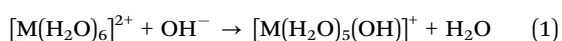
Laser irradiation is another powerful and versatile way to obtain CuO[246] and ZrO₂ spheres.[247] This method was even used to make hollow spheres of metals and semiconductors such as Fe, Co, Ni, TiO₂, Co₃O₄, NiO, WO₃ and Fe₂O₃.[248] The method offers control over the size of particles and high crystallinity, and therefore no annealing step is required. The high energy dispersed during laser heating was successful in producing single-crystalline rutile TiO₂ at room temperature with an average size of 540 nm[248] from commercial anatase TiO₂ nanoparticles dispersed in acetone. The hollowing was attributed to the Kirkendall effect. The size of spheres could be tuned by controlling the laser beam and irradiation time; however the size of the void space could not be controlled. In another light-driven approach, UV irradiation was used to decompose titanium glycolate spheres into highly uniform mesoporous TiO₂ spheres with amorphous structure.[249]

Some other methods include thermal decomposition of various precursors such as Ni(CH₃COO)₂·4H₂O at 500 °C for 10 h to produce NiO mesoporous spheres,[250] synthesis of hollow CuO spheres[212] involving direct printing of metal–ion complex ink on a substrate followed by thermal heating, and a gas–liquid diffusion method to prepare Co₃O₄ hollow spheres by controlled precipitation from a solution of Co(NO₃)₂ in the presence of a vapor from crushed ammonium carbonate.[251]

## 2.4 Methods for controlling the precipitation process

To prevent the uncontrolled precipitation of the metal oxide into large aggregates, the release of reactants in solution can be regulated. The commonly used procedures to control the precipitation process include metal complexation, pH control and controlled release of other reactants. Very low concentrations of metal precursors (usually in mmol amounts) are used as the first preventive measure.

**2.4.1 Complexation.** Metal ions present in solutions have a high positive charge to radius ratio, which makes them highly electronegative, i.e., they have a high affinity for electrons. As a result, the metal cations tend to attract polar molecules (or ligands) in solution by chelation to form stable dissolved metal complexes. Examples of ligands that form metal complexes are water, NH₃,[122] simple organic compounds such as organic acids (e.g. citric acid,[37] ascorbic acid[34] and tartaric acid[37]), alcohols (methanol[48] and EG[82,88]), amines,[59,252] acetylacetonates,[30] acetates,[2,32,42] citrates[38,58] and oxalates.[31] The metal complexes prevent the uncontrolled precipitation of the metal oxides into aggregates by slowly combining with hydroxide ions via multiple steps, as shown in eqn (1) and (2) for a hexa-aqua 2+ complex, until a neutral complex is precipitated out of the solution.

$$[M(H_2O)_6]^{2+} + OH^- \rightarrow [M(H_2O)_5(OH)]^+ + H_2O \quad (1)$$

$$[M(H_2O)_5(OH)]^+ + OH^- \rightarrow [M(H_2O)_4(OH)_2] + H_2O \quad (2)$$

Cations with high positive charge such as Ce³⁺,[26] Fe³⁺,[35] In³⁺,[253] Sn⁴⁺[47,48] and W⁶⁺[52,53] can precipitate from the solution via forced hydrolysis at elevated temperatures without the need of

a basic additive. The soluble hydroxyl complexes created by hydrolysis reaction (as per eqn (3)) form precursors for the nucleation of crystallites.

$$[M(H_2O)_n]^{z+} \rightleftharpoons [M(H_2O)_{n-y}(OH)_y]^{(z-y)+} + yH^+ \quad (3)$$
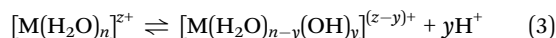
Ligands behave like surfactants or capping agents, since they adhere to preferred planes of the grains/crystallites, which then prevent their growth in specific directions. This gives rise to hierarchical spherical structures, built from differently shaped building blocks, such as nanocubes, nanosheets, nanopetals, nanowires, etc.

**2.4.2 pH control.** While the availability of metal ions is controlled via chelation, there are other methods to limit the availability of OH⁻ ions for precipitation. A slow release of OH⁻ ions for controlled precipitation of metal hydroxide complexes can be realized in solution via degradation of amides (such as urea) and amines (such as HMT, hydrazine and ethanolamine) at moderate temperatures (above 80 °C). Tables 1 and 4 show that this method is popular for the synthesis of solid and hollow spheres at moderate temperatures.

To successfully coat a homogeneous and very thin layer of metal oxide on a substrate can be a very challenging task. This subject has been studied by Zhang et al.,[138] who reported a simple but interesting method of controlling the amount of OH⁻ ions available for precipitation of metal hydroxides, which could be converted to metal oxides upon calcination. For controlled precipitation, the ionic product of the metal hydroxide precursor ($K_{mp}$) has to be equal to or slightly higher than its solubility constant ($K_{sp}$). For a metal hydroxide M(OH)ₙ, $K_{mp}$ can be related to pH as expressed by eqn (4) and (5):

$$K_{mp} = [M_{aq}^{n+}][OH_{aq}^-]^n \quad (4)$$

$$K_{mp} = [M_{aq}^{n+}][K_w \times 10^{pH}]^n \quad (5)$$

Hence for precipitation,

$$K_{mp} \geq K_{sp} \quad (6)$$

where n is the valence number of the metal ion and $K_w$ is the water dissociation constant, which has the value of $1.00 \times 10^{-14}$ mol² L⁻². A buffer solution within the required pH range can then be used to provide a constant pH during reaction for controlled precipitation. Consequently, for Al₂(SO₄)₃ in a formic acid/ammonium formate buffer solution within the pH range of 3.8 and 4.6, a nanolayer of Al₂O₃ could be coated on different kinds of substrates such as Au, Si, SiO₂ and PS and different shapes could be created such as core–shell structures of multi-walled carbon nanotubes. The thickness of the shell could be controlled between 1 and 20 nm by adjusting the concentration of Al₂(SO₄)₃ salt. This method can be easily extended to other metal oxide coatings.

**2.4.3 Controlled hydrolysis.** The reaction of alkoxides with water during the sol–gel process is extremely fast. A few protocols are adopted to avoid uncontrolled precipitation of particles. Commonly, very small amounts of water are used in high purity alcoholic solvents (purity very close to 100%). Also, alkoxide or hydrated precursors are added very slowly, e.g., by vapor

This journal is © The Royal Society of Chemistry 2016

Chem. Soc. Rev., 2016, 45, 6013–6047 | 6031

deposition[193] or in a dropwise fashion.[177,199,201] Gyger et al.,[151] on the other hand, minimized the contact of Sn(Ot-Bu)$_4$ with water by slowly adding a mixture of Sn(Ot-Bu)$_4$ in dodecane to a water-in-oil microemulsion system. The hydrolysis of tin tert-butoxide occurred slowly on water droplets at the organic–water interface, eventually leading to the formation of SnO$_2$ hollow spheres.

The deposition of a very thin layer of TiO$_2$ via the modified Stöber sol–gel method is normally difficult. However, it was successfully achieved by controlling the hydrolysis rate of the TiO$_2$ precursor by varying the amount of ammonia, which has a crucial role in controlling the reaction kinetics for the formation of TiO$_2$ shells.[204] Accordingly, the thickness of the TiO$_2$ shell could be changed from 25 nm to 70 nm by varying the ammonia concentration from 0.25 vol% to 0.4 vol%.

Some researchers used the in situ generated water during chemical reactions for the synthesis of metal oxide particles. Liu et al.[254] used the aldol condensation reaction between titanium isopropoxide and acetone to generate water molecules for the formation of TiO$_2$ spheres. Similarly, the water produced during the reaction of vanadium(v) oxytriisopropoxide with acetic acid catalyzed the hydrolysis–condensation process that led to the formation of vanadium oxide spheres.[51] Guo et al. synthesized TiO$_2$ spheres by using water generated during esterification reaction of ethanol and acetic acid.[255] In another example, TiO$_2$ shells were prepared on hydrated sulfate templates of ZnSO$_4$·7H$_2$O in ethanol.[256] The spherical templates of ZnSO$_4$·7H$_2$O in ethanol that were formed acted as sites for deposition of titanium species. Moreover, water present in hydrated crystals acted as a supplier of water molecules for hydrolysis of titania precursors.

# 3. Effect of synthesis parameters

In this section, we examine the effects of the different experimental parameters such as reaction time, reaction temperature, calcination, pH and reactant and solvent types on the structure and phase of metal oxide spherical particles.

## 3.1 Reaction time

During initial stages of the reaction, nanocrystallites are formed and start aggregating into spheres to reduce their surface energy. The spheres are amorphous in nature but their size, long range ordering and the degree of crystallinity improve with increasing synthesis time.

Solution phase reactions at high temperatures favor hollowing via Ostwald ripening as time increases. The hollowing can be initiated at the central core whereby the relatively small crystallites dissolve and migrate to recrystallize on larger crystals on the surface of spheres. This mechanism has been used to obtain hollow spheres of different metal oxides, such as CeO$_2$,[67,69,72] CuO,[33,78,79,143] CuO/CuO$_2$,[80] ZnO,[158] MgO,[95] ZrO$_2$,[62] SnO$_2$,[150] NiO,[244] TiO$_2$[257] and In$_2$O$_3$.[94] Some examples are presented in Tables 2 and 4. The shell thickness[67] or hollow core size[94] could be increased by increasing the reaction time.

However, the synthesis time should be carefully adjusted because an excessive reaction time can corrode and collapse the formed hollow structures.[33,158]

Another hollowing Ostwald ripening mechanism occurs at localized spots within the spheres, at fracture points or low crystal densities. Such cases can result in the formation of yolk–shell particles such as MoO$_2$@MoO$_2$,[102] TiO$_2$@TiO$_2$,[81,203] CeO$_2$@CeO$_2$,[70] γFe$_2$O$_3$@γFe$_2$O$_3$,[88] BaZrO$_3$@BaZrO$_3$[64] and LnFeO$_3$@LnFeO$_3$ (Ln = La, Pr–Tb),[91] multi-shell particles such as Fe$_3$O$_4$@TiO$_2$ double-shell structure[86] and V$_2$O$_5$ with up to three shells[117] or porous In$_2$O$_3$ particles.[37] However these structures are, in general, eventually transformed into hollow shells due to further dissolution of the core if reaction time is further increased.

## 3.2 Reaction temperature

The reaction temperature is an important parameter, which affects the rate of crystal nucleation and therefore the size, morphology and polymorph of metal oxide particles.

Temperature affects the crystallization rate, which limits the quantity of crystals formed. This in turn affects the shape[32,36,64,79] and size[21,32,146] of the synthesized particles. As the nanocrystals continuously form, they aggregate into hierarchical structures. During hydrothermal growth of CuO spheres, the particle shape evolved from irregular CuO nanoparticles at 80 °C to uniform spindle-shaped CuO nanorods with sharp ends at 100 °C, small amounts of nanospheres at 140 °C and large scale monodisperse nanospheres with a wave-like surface at 160 °C.[32] On the other hand, hollow flower-like spheres of α-GaOOH changed into microspheres and finally into rods as the temperature increased from 175 °C to 225 °C.[36] Therefore, the optimum temperature for achieving a maximum amount of the required structures needs to be experimentally determined. The diameters of solid spheres[21] or shells[32,146] can also increase with temperature. The ultrasound-assisted solution precipitation of MnO$_2$ produced spherical particles with an average size that could be tuned between 0.4 and 1.28 μm by varying the temperature from 30 °C to 70 °C.[21] High temperature was shown to favor the hollowing process of solid spheres via Ostwald ripening.[64,79,244] Conversely, the synthesis of hollow structures via bubble[82] and emulsion templating[83] is not recommended at high temperatures due to reduced stability of the liquid medium.

Changes in temperature can also affect the growth patterns of the crystals, giving rise to different crystal phases. As an example, the Cu$_2$O content in CuO spheres increased with temperature[79,80] while α-Fe$_2$O$_3$ was favored at elevated temperatures instead of FeOOH.[35,90]

## 3.3 Calcination

Calcination improves the crystallinity of metal oxides by densifying the crystallites and also removes organic impurities bound to the precursor during the hydrothermal process. As a result, the grain size of the crystals increases and the removal of water and CO$_2$ creates additional pores and interspaces. The sum of these effects generally decreases the surface area of particles

(although an increase in the surface area has been observed in some cases[56]) and increases the pore volume.

Calcination in an oxygen-containing atmosphere is required to remove carbon templates in the synthesis of porous or hollow spheres. Sometimes, multi-step calcination involving a pyrolysis step followed by oxidative calcination is required. During the synthesis of mesoporous $Nb_2O_5$,[123] the PEO-*b*-PS copolymer was used as a pore forming template and resol as a "glue" for the niobia composite following high temperature polymerization. The composite was pyrolyzed first at 350 °C to selectively decompose PEO-*b*-PS, then at 550 °C to crystallize $Nb_2O_5$ crystals without collapsing the polymer skeleton. Finally, the carbon skeleton was removed by calcination in air at 400 °C to obtain mesoporous crystalline $Nb_2O_5$ particles.

Some researchers reported the formation of yolk–shell structures of $ZnCo_2O_4$,[120] $SnO_2$, $CeO_2$ and $Tb_4O_7$[73] *via* simple calcination of metal oxide precursors at 600 °C (using a rate of 5 °C $min^{-1}$) that were hydrothermally loaded into the pores of carbon spheres. The template removal occurred in two steps with the burning off of the first layer closest to the surface, separating the oxide shell and the composite core. Further calcination removed the carbon template from the core to produce the yolk–shell metal oxide structures.

In some circumstances, the heating rate was found to have some interesting effects on the final structure of calcined particles. A zinc oxide precursor–carbon composite was calcined in air *via* three methods.[119] The first sample was calcined for 3 h in a preheated furnace at 550 °C, the second sample was calcined at a heating rate of 5 °C $min^{-1}$ to 550 °C and maintained for 3 h and the third sample was calcined at a heating rate of 2 °C $min^{-1}$ to 550 °C and maintained for 3 h. Single-shell hollow spheres were obtained from the first sample, while double- and triple-shell spheres were formed from the second and third samples, respectively. The formation of multi-shell particles was explained by the occurrence of a temperature gradient between the exterior and interior of the precursors, giving rise to an inside out Ostwald ripening process. Dong *et al.*[170] went a step further by proposing an easy way to control the number of shells and inter-shell spacing in hollow ZnO microspheres by controlling the heating processes (heating rate and final temperature) and precursor concentration on the carbon sphere templates. In another work, a gradual removal of the carbon core from C@V composite microspheres was successfully used to obtain $V_2O_5@V_2O_5$ yolk–shell particles.[116] The core was much larger when the C@V sample was annealed at 350 °C at a rate of 3 °C $min^{-1}$ as compared to a rate of 1 °C $min^{-1}$, due to the relatively fast removal of the carbon core at the highest rate, leaving behind a $V_2O_5$ core formed from the vanadium species that were initially bound to the carbon core. However, annealing at 400 °C at a rate of 1 °C $min^{-1}$ gave porous single-shell spheres. In a similar fashion, the control of heating rate could generate core-in-double-shell $NiCo_2O_4$ spheres[105] and multi-shell $Y_2O_3$ spheres.[180]

The calcination temperature can also govern the metal oxide polymorphism. For example, anatase $TiO_2$ forms between 300 °C and 600 °C and the more crystalline rutile phase starts to form at temperatures >600 °C,[182,191,258] the perovskite $LaFeO_3$ would not form below an annealing temperature of 750 °C,[91] β-$Bi_2O_3$ was obtained at 350 °C while α-$Bi_2O_3$ was formed at 450 °C,[259] the change of phase from γ-$Ga_2O_3$ to β-$Ga_2O_3$ occurred at $T$ > 700 °C[92] and γ-$Al_2O_3$ and α-$Al_2O_3$ were formed at 900 °C and 1100 °C, respectively.[121]

## 3.4 pH

We have already mentioned how pH alters the degree of precipitation and induces Ostwald ripening in the particles. Nevertheless, the solution pH can affect particle growth in various ways, for instance, by controlling adsorption of the precursor on carbon templates,[175] changing the degree of ionization of the ligands,[67] modifying the electric charge of the surface of nanoparticles[253] and altering the degree of complexation of the metal ions in solution.[104]

In the synthesis of $Mn_2O_3$, multi-shell structures were formed with the help of carbon sphere templates; the amount of metal cations that can be adsorbed on the carbon spheres was varied by using different solution pH (since high precursor concentration results in its accumulation on the template surface rather than in its infiltration into template pores).[175] This strategy was shown to be well suited to alter the zeta potential of carbon spheres and hence their electrostatic interaction with metal ions. As a result, depending on pH, single-, double- or triple-shell $Mn_2O_3$ structures were formed upon calcination.

$CeO_2$ particles of different shapes were respectively obtained at pH of 1, 2 and 3.5 in the presence of citric acid used as a ligand, namely, solid spheres, hollow spheres and microplates.[67] Due to the three levels of ionization of citric acid ($pK_a$ = 3.13, 4.76 and 6.4), different ligands were formed at different pH. At pH below 1, most of the citric acid was in solution as $H_3Cit$ without ionization, which coordinated with $Ce^{3+}$ to give solid microspheres. At pH = 3.5, $H_2Cit^-$ concentration was higher than $H_3Cit$ concentration, giving rise to microplates. At pH = 2, the ligands were a mix of $H_3Cit$ and $H_2Cit^-$, which resulted in the formation of coordination polymers (metal organic frameworks) in a metastable stage between solid spheres and microplates, compromising the shape into hollow spheres.

The pH of a microemulsion system was found to alter the surface energy and the electric charge distribution on the surface of $In(OH)_3$ nanoparticles as well as the amount of adsorbed CTAB on the different crystal faces.[253] As a result, the particles aggregated and grew in different directions to form bundles of nanorods at pH = 5 and spheres at pH = 3.

The hydrothermal synthesis of NiO in the presence of D-glucose was performed at different ammonia concentrations[104] to investigate its effect on the shape of final particles. A high concentration of ammonia decreased the concentration of free $Ni^{2+}$ by forming stable $[Ni(NH_3)_x]^{2+}$ complexes in solution and thereby controlling the rate of precipitation of $Ni(OH)_2$. Therefore, aggregated porous structures were obtained at pH < 10.5, and at pH 10.5 a controlled precipitation of the Ni species on the *in situ* formed carbon spheres followed by calcination afforded

This journal is © The Royal Society of Chemistry 2016

*Chem. Soc. Rev.*, 2016, **45**, 6013–6047 | 6033

hollow microspheres. A further increase of pH to 10.9 reduced the rate of precipitation of nickel hydroxide, allowing formation of carbon layers on the surface of $Ni(OH)_2$ particles, which upon calcination were converted to multi-shell NiO microspheres. Therefore, pH is an important parameter to consider for controlling the morphology of particles.

### 3.5 Solvents and reactants

The type and composition of solvents is also an important factor that can be used to manipulate the morphology and surface area of metal oxide particles.[55,83,90,95,122,251,260]

A mixture of water and ethanol was used to synthesize multi-shell $Co_3O_4$ when using carbon spheres as templates as opposed to single shells when only water was used.[171] The effect of ethanol was used to decrease the number of aqua groups coordinated to Co ions, hence to decrease the size of the hydrated Co ions. This strategy was used to control the diffusion of ions through the carbon template, allowing the production of spherical structures, which upon calcination gave multi-shell structures. The same principle was applied to synthesize $\alpha$-$Fe_2O_3$ multi-shell hollow microspheres.[172]

The quasi-emulsion template was used for the formation of $\alpha$-$Fe_2O_3$ hollow spheres;[83] the concentration of the soft template was varied by changing the glycerol/water ratio at 145 °C. As a result, the morphology was evolved from solid flower-like particles consisting of densely packed needle-like subunits to hollow spheres and finally solid spheres made up of nanosheets at the solvent ratios of 1:19, 1:7 and 1:4, respectively. The effect of the EG/water ratio was investigated during hydrothermal synthesis of MgO microspheres.[95] It was found that at a high EG volume, spheres were obtained, while at a high water volume, nanoplates were formed.

In another work, the glycol concentration had no effect on the morphology but rather affected the surface area of the synthesized particles.[122] The BET surface area of CuO spheres (before calcination) decreased from 157 $m^2$ $g^{-1}$ to 104 $m^2$ $g^{-1}$ as the glycol content in water increased.

The solvent ratio can also influence the particle size. The solution phase precipitation at room temperature of $V_2O_5$ spheres in a mixed solvent of acetone, pyridine and water gave particles of different sizes (between ~150 nm and ~1000 nm) simply by varying the water or pyridine concentration.[127]

An increase in the ratio of the structure directing agent (SDA) to the metal precursor improved the sphericity of particles such as ZnO,[56,185] $SnO_2$,[125] and $Bi_2WO_6$ spheres[24] as well as $\alpha$-$Fe_2O_3$ multi-shell hollow spheres[87] because SDA acted as a capping agent and prevented uncontrolled aggregation, although an excess of SDA can be detrimental to the crystallinity[118] or development of the structures.[24] Moreover, this ratio has also been used to control the size and morphology of particles such as NiO,[43] $Y_2O_3$,[261] ZnO,[134] $ZnCo_2O_4$@$CeO_2$,[133] $Bi_2O_3$,[23] $SnO_2$[48] and $Co_3O_4$.[28] Conversely, the effect of the change in the precursor concentration while keeping the overall ratio constant has been examined in the low temperature precipitation of ZnO hollow spheres using HMT at a 1:1 ratio.[159] Hollow fluffy-like spheres having a size of 2–3 µm

and a surface area of 138 $m^2$ $g^{-1}$ were produced; however a decrease in the concentration of the reactants (but keeping the same ratio) gave solid spheres with a net-like surface and a much higher surface area of ~368 $m^2$ $g^{-1}$.

The type of reactant can also impact the shape or phase of the final products. $CuO$/$Cu_2O$ hollow spheres were obtained *via* a hydrothermal method using ethanolamine but CuO flower-like spheres were obtained when ammonia was used.[80] In the hydrothermal synthesis of NiO spheres, the $\beta$-$Ni(OH)_2$ phase was formed when NaOH or ethanolamine was used while $\alpha$-$Ni(OH)_2$ was formed with urea instead.[43] This study indicates that the phase and structure of the final products depend on the special properties and structure of the reactants used.

## 4. Applications of spherical metal oxide particles

Metal oxides are used in diverse and multidisciplinary areas ranging from industrially relevant sensing and catalytic uses to biomedical, environmental and energy-related applications. This section shows how the characteristics of different metal oxides affect their respective applications.

### 4.1 Sensing and catalytic applications

**4.1.1 Sensors.** Sensors are used to measure and detect slight changes of a chemical compound or molecule in their surroundings, resulting in important applications in fields such as environmental monitoring, biomedical detection, oil and gas industry, metallurgy, food industry, *etc.* Some typical chemicals that require sensing are flammables such as ethanol,[27,45,56,57,59,93,251,262–264] acetone[131,262] and hydrogen,[47,48,125] strong oxidizing agents such as $H_2O_2$,[123] health hazards such as 2-chloroethanol,[46] ammonia,[158] $H_2S$,[143] methanol,[183] toluene,[30,131] $NO_2$,[130] trimethylamine,[226] formaldehyde[82,205] and CO[47,48,151] as well as glucose[239,240] to monitor its level in blood. While the most common materials that have been used are $SnO_2$ spheres and hollow spheres[45,47,48,125,151,262,264] and ZnO spheres and hollow spheres[56,57,59,158,239] due to their low cost and availability, other metal oxides have been tested too, such as $Nb_2O_5$ spheres,[123] $In_2O_3$ hollow spheres,[93,94,205] $MnO_2$ spheres,[240] $Co_3O_4$ spheres,[27] $Co_3O_4$ hollow spheres,[251] $\alpha$-$Fe_2O_3$ hollow spheres,[82] yolk–shell $\alpha$-$Fe_2O_3$ spheres,[84] CuO hollow spheres,[143] $WO_3$·$H_2O$ spheres,[131] $WO_3$ spheres,[130] $WO_3$ hollow spheres,[226] $Cr_2O_3$ spheres[30] and $TiO_2$ hollow spheres.[183]

Basically sensors operate in two ways. Biosensors make use of immobilized enzymes that can break down a biomolecule to give an electrochemical signal. On the other hand, n-type oxide semiconductors such as $SnO_2$, ZnO, $In_2O_3$, $TiO_2$ and $WO_3$ operate by the chemoresistive detection of reducing gases at their surface, involving the diffusion of the analyte gas towards the sensor surface and its electrochemical oxidation with a negatively charged adsorbed oxygen.[94] Sensors should have a high sensitivity (at the ppb or ppm level), very fast response (a few seconds), good selectivity towards similar substances, stability, a wide response range, a linear dependency with

respect to gas concentration, good repeatability and reusability. These qualities are imparted by the proper choice of sensor material with a microstructure that has been tailored to have specific properties such as a high surface area, porosity, thermal and chemical stability, a short diffusion length for efficient mass transfer, non-toxicity and biocompatibility (for biosensors). From morphology viewpoint, porous or hollow particles have been found to be well suited as sensing materials since their pores allow for rapid mass diffusion and can accommodate numerous active sites, while hollow particles offer short diffusion lengths and an empty structure that can act as a reservoir to continuously replenish active sites with the monitored substance. To improve their performance, some sensors have been loaded with precious metals such as Au,[47,56,262] Er[93] and Rh,[94] made as composites, for example $\alpha$-Fe$_2$O$_3$/In$_2$O$_3$ hollow spheres[263] or as hierarchical structures with high surface area such as nanosheet-assembled WO$_3$ microspheres[130] or Co$_3$O$_4$ microspheres composed of large and thin nanoplatelets.[27]

Kim et al.[94] observed that 1.67 atomic% Rh loaded into In$_2$O$_3$ hollow spheres showed an excellent response to 2–100 ppm ethanol, which was up to 180 times higher than in the case of unloaded In$_2$O$_3$ hollow spheres. Also, Rh additionally decreased the optimum operating temperature from 475 °C to 371 °C and enhanced the selectivity to ethanol 15–25 times. The sensing time was very short (0.4 s) but recovery time was relatively large ($\sim$200 s) due to thermal promotion of the surface reactions. A higher Rh loading could decrease the recovery time at the expense of a lower response, which was attributed to the formation of unwanted rhodium and indium phases.

Hierarchical MnO$_2$ spheres consisting of nanorod subunits were synthesized via electrodeposition and loaded with the glucose oxidase enzyme for the mediator-less detection of glucose.[240] The particles exhibited a high surface area of 129 m$^2$ g$^{-1}$ and pore size between 5 and 12 nm, which could easily accommodate the enzyme molecules. The sensor had a high sensitivity of 31.6 μA mM cm$^{-2}$, a large linear range up to 3.15 mM and a low detection limit of 0.35 μM. Moreover, no interference was observed with species that coexist with glucose in blood, such as ascorbic acid, uric acid and acetaminophen, indicating good selectivity of the sensor.

With the advent of more and more chemicals that are classified as toxic and the implementation of more stringent laws for their detection, the development of more versatile and sensitive sensors will be required in the future and metal oxides can effectively offer a solution.

**4.1.2 Catalysts.** The attributes that make metal oxide nanoparticles attractive as catalysts are their high surface area, easy accessibility of pores (for reactants as well as for loading noble metals), thermal resistance (since many catalytic reactions are performed at elevated temperatures), toughness (to avoid damage during multiple use), chemical stability, environmental friendliness, special inherent properties that are useful for specific applications and ability to interact synergistically with loaded nanometals for superior catalytic performances.
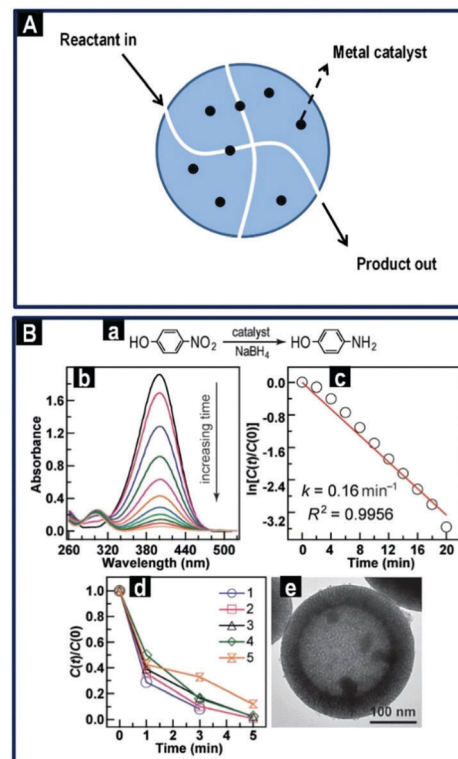


Fig. 12 (A) Operating principle of a metal oxide support loaded with nanoparticles of a metal catalyst. (B) Catalytic reduction of 4-NP to 4-AP. (a) Reaction equation. (b) Time-dependent absorption spectra of the reaction solution in the presence of the Pd nanocube-embedded hollow mesoporous TiO$_2$ microspheres. (c) Plot of ln[$C(t)/C(0)$] against the reaction time. The $R^2 = 0.9956$ is the coefficient of determination obtained from the linear fitting. (d) Plot of $C(t)/C(0)$ against the reaction time for five successive cycles of the reduction reaction catalyzed by Pd nanocube-embedded hollow mesoporous ZrO$_2$ microspheres. (e) TEM image of the ZrO$_2$ microspheres after five cycles of the reduction reaction (panel B reproduced with permission from ref. 223. Copyright © 2013, Wiley-VCH).

Fig. 12A presents a simplified illustration of the operating principle of a supported catalyst.

The environmentally friendly room temperature degradation of HCHO to CO$_2$ and H$_2$O was achieved by using Pt loaded $\gamma$-Al$_2$O$_3$ hollow spheres.[63] As shown in Fig. 12B, the hierarchical macro–mesoporous structure allowed for high dispersion of Pt and accessible pores facilitated diffusion of reactive molecules and products to/from reaction sites, respectively. In another work,[223] the embedded Pd nanoparticles inside the hollow space of mesoporous TiO$_2$ and ZrO$_2$ spheres synthesized via the PS nanospherical template-assisted aerosol method prevented the aggregation of metal nanoparticles and reduced the loss of catalyst during recycling, enhancing the reduction reaction of 4-nitrophenol. Similarly, high CO oxidation at low temperatures was possible via the use of nanosized Au in Au@TiO$_2$ yolk–shell particles due to the unique synergy between Au and TiO$_2$ and the protection of nanometal by the shell.[199]

Porous ZrO$_2$ microspheres have strong Lewis acidity and poor Brønsted sites but their treatment with phosphoric acid could improve the acidity of the Brønsted sites.[136] The synthesized catalyst was tested for the catalytic Friedel–Crafts alkylation of

This journal is © The Royal Society of Chemistry 2016

Chem. Soc. Rev., 2016, 45, 6013–6047 | 6035
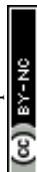
indoles with chalcones, giving 98% yield in 6 h and showed a negligible loss in its activity even after 22 reuses. Similarly, Friedel–Crafts reactions were carried out with mesoporous $Nb_2O_5$ spheres[40] and $Fe_3O_4$@$TiO_2$ double-shell yolk–shell particles[86] once the Lewis and Brønsted sites were improved by acidification with sulfuric acid and hydrothermal treatment in basic solution, respectively.

$CeO_2$ on the other hand shows strong oxygen storage and release capacity *via* facile conversion between $Ce^{3+}$ and $Ce^{4+}$. This makes ceria a model catalyst for oxidation reactions. Hollow $CeO_2$ spheres converted 43% CO at 295 °C,[70] while 10% Cu doped $CeO_2$ spheres showed >98% CO conversion at 210 °C[68] and a complete oxidation was achieved on the core–shell $ZnCo_2O_4$@$CeO_2$ particles at less than 200 °C.[133] However, loading $CeO_2$ with noble nanometals such as Pd,[74] Ag[26] and Au[69] drastically improved its performance at much lower temperatures. For instance, Pd@$CeO_2$ multi-yolk–shell particles achieved 100% CO oxidation at 110 °C.[74] The catalyst also performed excellently in the case of aerobic oxidation of cinnamyl alcohol into cinnamaldehyde with >99.9 conversion after 1.5 h. In another case, $CeO_2$ doped into $MnO_2$ hollow spheres could catalytically oxidize benzene with 90% oxidation at 252 °C and completely oxidize it at 340 °C.[99]

Mesoporous NiO spheres and flowers having a size of 500 nm and mesopores in the range of 10–30 nm showed high catalytic activity for the transformation of toxic phenolic pollutants.[2] Furthermore, the NiO nanostructures with large scale nanocrystal domains and well-shaped morphologies imparted magnetic properties to an otherwise antiferromagnetic system due to the quantum confinement effect, allowing easy magnet-assisted separation.

Other types of metal oxides and their combinations have been investigated for several other reactions. Perovskite $LnFeO_3$ (Ln = La, Pr–Tb) hollow spheres showed an excellent catalytic performance for NO + CO reaction at high temperatures between 200 °C and 500 °C due to their outstanding thermal and chemical stability.[91] MgO spheres and flowers performed much better than bulk MgO in the Claisen condensation of benzaldehyde and acetophenone under solvent-free conditions.[265] $Co_3O_4$ hollow spheres were used for methane conversion[141] and $H_2O_2$ oxidation.[142] $Fe_3O_4$@$SiO_2$@void@$TiO_2$ particles were employed as a catalyst for epoxidation of styrene,[198] giving a high conversion and selectivity of 90.2% and 88.5% respectively. In the latter work, the $Fe_3O_4$ core was well protected by the $SiO_2$ layer and the void space was successfully loaded with Au nanometals, which respectively provided magnetic separability and high reactivity and reusability.

## 4.2 Biomedical applications

### 4.2.1 Photoluminescence.
Rare earth doped materials have been widely used as high performance upconversion or down-conversion luminescent devices. Upconversion is an optical process in which the interaction of two or more photons leads to the emission of light at shorter wavelength than the excitation wavelength such that energy is conserved, while in down-conversion, one high energy (short wavelength) photon is converted to two or more, low energy (longer wavelength) photons. This behavior arises due to their unique electronic and optical properties resulting from their 4f electrons. The host matrix for the rare earth elements needs to have good chemical durability, thermal stability and low phonon energy. Lanthanide oxide spheres such as $Y_2O_3$ solid and hollow spheres[55,132,155–157,261] or $Lu_2O_3$ hollow spheres[266] have been used in upconversion devices. For example, under UV or low voltage electron beam excitation, the $Ln^{3+}$ ($Ln^{3+}$ = $Eu^{3+}$ and $Tb^{3+}$) ion doped $Y_2O_3$ samples showed strong red and green emission, respectively,[156] whereas multi-color upconversion emission was realized under 980 nm excitement when using Er doped $Y_2O_3$ spheres.[132] Furthermore, multi-shell structures revealed that the upconversion luminous intensity increased as the number of shells increased due to multiple reflections and the enhanced light harvesting.[180] Luminescent materials could find application in the field of lighting, optoelectronic devices, biological labeling and drug delivery. Recently, hollow structured $Y_2O_3$:Yb/Er–$Cu_xS$ nanospheres with multifunctionalities were created.[267] Aside from upconversion luminescence properties, the material showed good biocompatibility and exhibited high ablation efficiency with regard to tumor cells because of the synergetic therapeutic effect between chemotherapy and photothermal therapy arising from loaded DOX and attached $Cu_xS$ nanoparticles.

Some semiconductors were shown to have photoluminescence capabilities. This arises from oxygen vacancy defects that can accommodate photogenerated electrons, which release photons upon recombination with free photogenerated holes. Some examples of semiconductors that have been found to possess photoluminescence properties are perovskite $BaZrO_3$ hollow spheres,[64] $In_2O_3$ spheres[37,253] and $\gamma$-$Ga_2O_3$ hollow nanoflowers,[92] with the latter also showing excellent solar blind detection performance.

### 4.2.2 Drug delivery and antimicrobial properties.
Metal oxide spheres are also good candidates as drug delivery vehicles. TiZr oxide spheres showed high loading of drugs such as IBU, DEX and ERY as well as hydrolytic stability and sustained release profiles in simulated body fluids.[268] $Gd_2O_3$ nanoparticles have a combination of magnetic and optical properties, which can be advantageous in the field of biomedicine. Indeed, $Gd_2O_3$:Yb/Er hollow spheres could simultaneously serve as a dual-imaging agent for optical/MR imaging and as a vehicle for drug storage/release.[145] Magnetic-based drug distribution was also a possibility with PEG-coated $Fe_3O_4$ and $\gamma$-$Fe_2O_3$ hollow spheres.[85] Both structures had high ibuprofen storage capacities of 297 mg $g^{-1}$ and 237 mg $g^{-1}$, respectively. Furthermore, a sustained drug release could be observed with most of the loaded drug released to the simulated body fluid in 136 h; the process of loading and releasing drugs is illustrated in Fig. 13A.

Nor *et al.* reported hematite hollow nanospheres (HNS) synthesized by the hard templating method; reduction of hematite HNS by $H_2$ led to magnetite HNS (Fig. 13B). It was reported that magnetite HNS (hematite HNS and C-magnetite) shows superior antibacterial performance towards both *E. coli* and *S. epidermidis* (Fig. 13C). In comparison to hematite HNS,
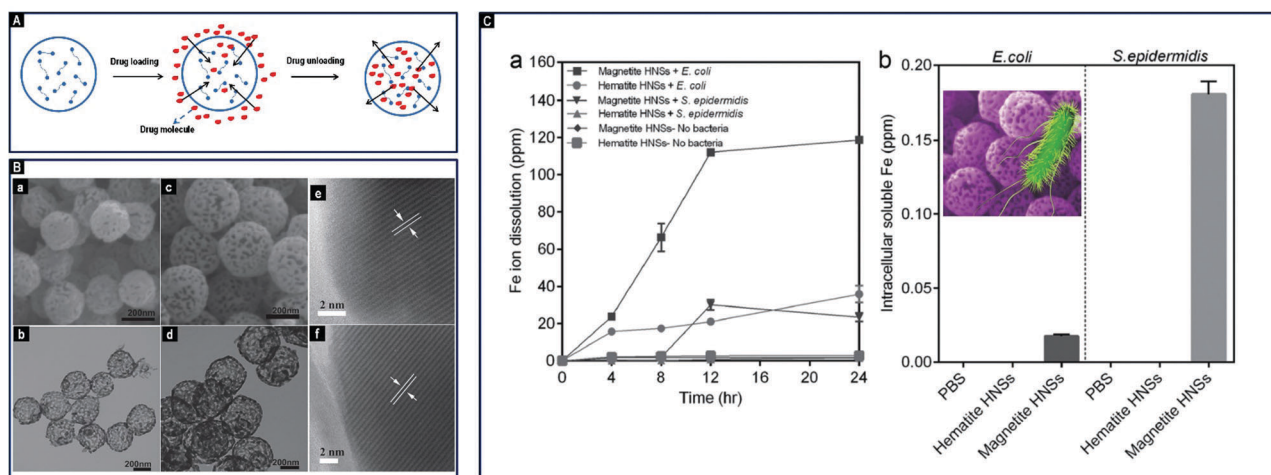
6036 | *Chem. Soc. Rev.*, 2016, **45**, 6013–6047

This journal is © The Royal Society of Chemistry 2016

**Fig. 13** (A) Schematic illustration of loading and unloading a drug to/from the PEG-coated hollow metal oxide particles. (B) (a) HRSEM image, (b) TEM image of hematite HNS, (c) HRSEM image, (d) TEM image of magnetite HNS, (e) HRTEM images of hematite HNS showing lattice fringes of the (006) plane, and (f) magnetite HNS showing lattice fringes of the (311) plane. (C) (a) Dynamics of extracellular dissolution of total Fe throughout the course of microbial growth in the absence and presence of bacteria and (b) intracellular content of Fe in the bacteria after 4 h incubation with nanoparticles of 500 μg ml$^{-1}$ concentration in LB broth (the inset illustrates the enhancement of the antimicrobial process). (Panels B and C reproduced with permission from ref. 269. Copyright © 2016, Wiley-VCH.)

magnetite HNS allows for a multiple-fold increase in the generated soluble iron ions, showing that the control over both the composition and nanostructure is crucial for tuning the antimicrobial activity of iron oxides.

### 4.3 Environmental applications

**4.3.1 Photocatalysis.** Semiconductors can be photoexcited by light of suitable energy to generate electrons and holes, which can be used as mediators for the photocatalytic removal of pollutants (commonly dyes) and even for bacterial deactivation.[23,107] The pertinent features of a semiconductor nanomaterial that make it an attractive photocatalyst are its morphology, phase, size of crystals, chemical and physical stability and reduced amount of defects in the crystal lattice. These allow for increased lifetime of photogenerated electrons and holes and their fast migration towards the particle's surface for redox reactions, while reducing the probability of their recombination. Additionally, a proper engineering of semiconductor nanocrystallites can effectively reduce the band gap energy (hence the required energy of incident photons) with respect to the bulk sample, due to the quantum confinement phenomena, making them responsive to visible light. Numerous materials have been employed as photocatalysts using UV light such as $SnO_2$ spheres,[107,125] ZnO spheres and hollow spheres,[58,60,118,270,271] ZnO multi-shell hollow spheres,[119] $\gamma$-$Fe_2O_3$ hollow spheres,[88] $In_2O_3$ spheres,[38] $\alpha$-$Ga_2O_3$ spheres,[36] $CuO/Cu_2O$ composite hollow spheres,[80] $SiO_2$ supported $Ta_2O_5$ hollow spheres,[113] perovskite type $SrTiO_3$ hollow spheres[112] and $Fe_3O_4$@$TiO_2$ double-shell yolk–shell spheres.[86] Catalysts that performed well under visible light due to their narrow band gap energy were $Bi_2O_3$ spheres,[23,259] $WO_3$ spheres and hollow spheres,[129,153] $\alpha$-$Fe_2O_3$ spheres[34] and $CeO_2$ hollow spheres,[71] perovskite types such as $BiFeO_3$ spheres[66] and

$Bi_2WO_6$ spheres[25,229] and composites such as $CeO_2/Bi_2O_3$ nanospheres,[272] $Bi_2O_3/Co_3O_4$ spheres,[65] $WO_3/TiO_2$ spheres[54] and $WO_3/WO_3·H_2O$ hollow spheres.[154]

The morphology of the material is of utmost importance for designing a photocatalyst. A large surface area affords numerous reaction sites and a high crystallinity favors photocatalytic activity due to effective charge migration. Indeed, the annealing process improves the crystallinity of the material but at the expense of the total surface area. Therefore, a compromise needs to be reached for the best crystal size and the largest possible surface area for optimum photocatalytic performance. $SnO_2$ spheres calcined at 150 °C had the best activity under UV light for the degradation of methyl orange as compared to uncalcined samples and samples calcined at 200 °C, 300 °C and 500 °C respectively.[125] Similarly, $Bi_2O_3$ spheres calcined at 350 °C degraded 99% of methyl orange under visible light after 3.5 hours as compared to only 25% degradation for samples calcined at 500 °C. It was also shown that hollow structures performed better than solid ones due to multiple light reflection and absorption within the structure cavities (Fig. 14A) and stability of the photogenerated charge carriers.

Dilger et al.[225] studied the effect of nanoarchitecture on the photoconductivity of ZnO particles (Fig. 14B). They found that the time needed for the current from photogenerated charge carriers to drop down to 10% of its maximum value ($T_{0.1}$) was <60 s for bulk and porous ZnO, whereas for yolk–shell and hollow spheres, $T_{0.1}$ was substantially higher reaching 521 s and 1150 s, respectively. This structural effect is duly reflected by photocatalytic experiments using various materials. Porous $CeO_2$ hollow spheres degraded 92% of gas phase acetaldehyde within 24 h, four times better than in the case of $CeO_2$ nanoparticles, despite the fact that the latter had a smaller band gap (2.88 eV as compared to 3.01 eV for hollow
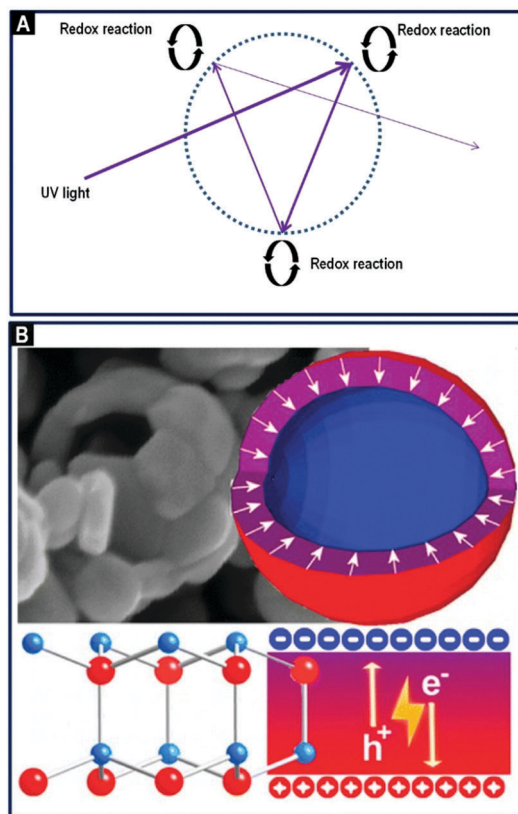
**Fig. 14** (A) Schematic illustration of multiple reflection and absorption of UV light in a hollow shell photocatalyst. (B) SEM image and schematic illustration of photoexcitation electrons and holes migrating to the opposite sides of the interface in hollow ZnO spheres (panel B reproduced with permission from ref. 225. Copyright © 2014, American Chemical Society).

$CeO_2$ spheres) and better crystallinity.[71] $WO_3$ hollow spheres had better performance than flower-like spheres, with first order kinetics of 0.056 min$^{-1}$ as compared to 0.0151 min$^{-1}$ for the removal of rhodamine B under UV light.[129] While both structures possessed similar surface areas (13 m$^2$ g$^{-1}$ and 16 m$^2$ g$^{-1}$ for the microspheres and hollow spheres, respectively), the improvement in the catalytic activity of the hollow spheres was attributed to the large textural porosity between 3.3 nm and 89.6 nm. Increasing the number of shells also resulted in better photoactivity. For example, ZnO hollow spheres with 1, 2 and 3 shells degraded 84.1%, 88.3% and 99% of rhodamine B respectively,[119] while the required time for complete degradation of the same pollutant under visible light was 1.5 h for $WO_3$ with multiple shells as compared to 2.5 h for single shell particles.[153]

The crystal phase, due to its geometric structure, is another important aspect that is related to photoactivity. Hou *et al.*[273] showed that the β-phase of $Ga_2O_3$ exhibited superior photocatalytic activity towards the gas phase degradation of aromatic compounds as compared to α- and γ-$Ga_2O_3$. Also, studies of $Fe_2O_3$ as catalyst showed that α-$Fe_2O_3$ spheres could completely degrade rhodamine 6G after 1 h under visible light irradiation,[34] while F doped γ-$Fe_2O_3$ needed UV light to degrade rhodamine B.[88]

$TiO_2$ has been the most extensively studied semiconductor for photocatalytic purposes due to its abundance, low cost, non-toxicity and high photoactivity accompanied by a high oxidation and reduction potential. $TiO_2$ can oxidize a large variety of organic compounds in water or air[182,189,193,200,203,254–257,274–278] and has also been successful for reducing metal ions such as $Cr^{6+}$ [193] and for $H_2$ production.[254] The major factors affecting the degree of photoactivity are surface area, porosity, crystallinity and morphology. A high crystallinity is desired rather than a large surface area to increase the separation between the photogenerated electrons and holes, and reduce their instantaneous recombination. However, the rutile phase despite its higher crystallinity and lower band gap energy has a lower activity than the anatase phase because of the lower surface area of the rutile particles. As a result, the surface area and the crystal size of particles have to be finely tuned due to their inverse role in photocatalysis, which is the reason why a wide discrepancy has been observed for the optimum calcination temperatures of the synthesized $TiO_2$ particles (between 450 °C and 800 °C for grain sizes varying between *ca.* 12 and 30 nm), depending on their sizes, morphologies and treatment methods.[177,182,200,278] The activity of $TiO_2$ under visible light has been enhanced by doping with Pt,[254] $CO_3^{2-}$,[254] N,[193,279] metal oxides,[256] CdS[184] and even trace organics from the solvent or organic precursor,[255] since the inclusion of a dopant within the $TiO_2$ matrix provides a sink for photogenerated electrons, thereby reducing the degree of electron–hole recombination. Similar to other semiconductors discussed in this section, the hollow shell morphology $TiO_2$ performed better than its other counterparts[203] because of multi-reflection of light.

**4.3.2 Adsorption.** Due to their isoelectric point and porosity, semiconductors have been useful as adsorbents for removal of pollutants from wastewater. MgO spheres had excellent adsorption properties towards fluoride and arsenic in water, with 120 mg g$^{-1}$ [95] and 569.7 mg g$^{-1}$ [96] respectively. $ZrO_2$ solid and hollow spheres,[62] CuO spheres and $Cu_2O$ hollow spheres,[32] NiO spheres,[42,43] perovskite $BaZrO_3$ hollow spheres[64] and $CeO_2$ hollow spheres[70] were used for the removal of anionic dyes, while urchin-like α-FeOOH hollow spheres[90] had high removal capacities towards both organic dyes and heavy metal ions. $MnO_2$ spheres with a hierarchical dandelion-like surface structure, a high surface area of 163 m$^2$ g$^{-1}$ and main mesopores of about 65 nm showed both oxidation and adsorption properties over lethal As(III) species.[17] The As(III) species could be effectively oxidized by $MnO_2$ particles to the less toxic As(V) species, followed by their adsorption.

### 4.4 Energy storage and conversion applications

**4.4.1 Lithium-ion batteries.** Transition metal oxides have been actively investigated as electrodes for lithium-ion batteries because they can reach high theoretical reversible capacities of more than 700 mA h g$^{-1}$,[280] while the graphite used in commercial batteries has a relatively low Li storage capacity of 370 mA h g$^{-1}$.[18] The energy density and life-cycle of the existing Li-ion batteries are unsatisfactory for many applications involving large devices such as electric vehicles and large scale energy grid storage,[102] and better alternatives are being explored. The two major advantages offered by metal oxide

**6038** | *Chem. Soc. Rev.*, 2016, **45**, 6013–6047

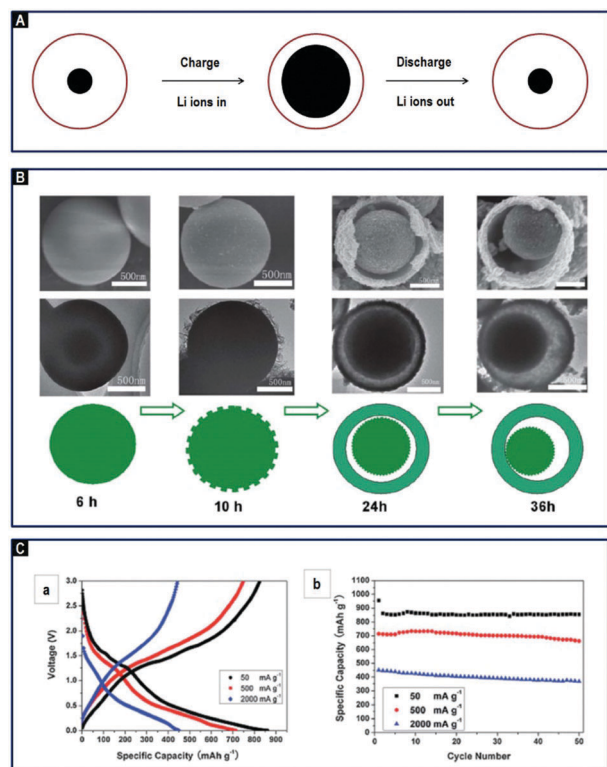This journal is © The Royal Society of Chemistry 2016

**Fig. 15** (A) Charging and discharging of Li ions in a yolk–shell type Li-ion battery; (B) schematic illustration of the formation process of yolk–shell MoO$_2$ microspheres; (C) (a) discharge–charge voltage profiles of the MoO$_2$ electrode at different current densities of 50, 500 and 2000 mA g$^{-1}$; and (b) cycling performance of the as-synthesized MoO$_2$ microspheres at 50, 500 and 2000 mA g$^{-1}$. (Panels B and C reproduced with permission from ref. 102. Copyright © 2013, Royal Chemical Society.)

colloidal structures that make them attractive as electrodes in lithium-ion batteries are high surface area for better contact of the active material with the electrolyte and porosity, which accommodates the volume change associated with the insertion and extraction of Li ions during charging and discharging processes, as shown in Fig. 15 for yolk–shell type particles.

V$_2$O$_5$ microspheres synthesized by an additive-free hydro-thermal method involving a hierarchical assembly of nanopor-ous fibers possessed a moderate surface area of 42 m$^2$ g$^{-1}$.[51] The structure endowed the material with shorter diffusion pathways for easier Li and electron transport hence enhancing electrochemical performance. The microspheres displayed a very stable capacity retention of 130 mA h g$^{-1}$ over 100 cycles at a current rate of 0.5C and showed an excellent rate capability with a capacity of 105 mA h g$^{-1}$, even at a high rate of 30C. Also, TiO$_2$ anatase spheres consisting of ultrathin nanosheets formed via crystals growing in the [001] direction[188] performed well at low and high rates. In another work,[250] NiO spheres with loosely connected crystals, a surface area of 30 m$^2$ g$^{-1}$ and pore size distribution in the range of 10–60 nm provided suitable pathways for efficient transport of electrolyte ions, large surface to volume ratios, and good structural stability to deliver a reversible capacity of 800 mA h g$^{-1}$ after 100 cycles at a current density of 500 mA g$^{-1}$. The material was also tolerant to various

charge and discharge currents, indicating high rate performance for high power applications. Aside from the morphology, crystal polymorphs can also be a deciding factor in the fabrication of metal oxide-based Li-ion batteries. It was shown that the anatase phase exhibited higher capacity than either brookite or rutile due to the more favorable Li ion insertion mechanism.[188,191,281,282]

Hollow structures have also attracted great attention due to the increased contact area between the electrode material and electrolyte as well as their mechanical flexibility. Hierarchical orthorhombic V$_2$O$_5$ hollow spheres showed good performance in Na-ion batteries (an alternative to Li-ion batteries) due to the predominantly exposed [110] crystal planes, which provided channels for easy Na$^+$ insertion and extraction as well as high tolerance to the deformation imparted by voids in the shells of hollow spheres.[115]

Mn$_3$O$_4$ hollow spheres synthesized by an aerosol method featured a high surface area of 96 m$^2$ g$^{-1}$ and thin shells of 5–10 nm. These hollow spheres exhibited good stability with a high capacity retention of 980 mA h g$^{-1}$ over 140 cycles and exceptional rate capability by retaining a capacity of 300 mA h g$^{-1}$ at an ultra-high current density of 10 000 mA g$^{-1}$.[224] These values represent the best electrochemical performance for Mn$_3$O$_4$ anode materials to date and were attributed to the unique thin wall hollow structure, which provided considerably reduced diffusion paths for electrons and Li ions. On the other hand, multi-shell hollow α-Fe$_2$O$_3$ showed a superior capability of 1203 mA h g$^{-1}$ at a current density of 100 mA g$^{-1}$ after 128 cycles and an excellent cycling stability of 870 mA h g$^{-1}$ at a current density of 400 mA g$^{-1}$ after 300 cycles due to the material's hierarchical porosity and structure, which assured shorter diffusion pathways for efficient transport of electrons and Li ions.[87] An excellent performance of multi-shell hollow α-Fe$_2$O$_3$ spheres was indeed recently confirmed by another work,[172] reporting up to 1702 mA h g$^{-1}$ at a current density of 50 mA g$^{-1}$, which was due to the enhanced volumetric capacity of the structure that allows for maximum lithium storage. Recently, multi-shell V$_2$O$_5$ hollow microspheres, synthesized by a simple method involving adsorption of anions on carbon templates, were found to exhibit an exceptionally high specific capacity of 447.9 mA h g$^{-1}$ (at a high current density of 1000 mA g$^{-1}$), exceptional rate capability and cycling stability, due to the ample charge storage sites, short transport paths and good structural stability of the material.[176] These attributes also belong to yolk–shell structures such as MoO$_2$@MoO$_2$[102] and V$_2$O$_5$@V$_2$O$_5$.[116,117] The superiority of the yolk–shell structure over solid spheres was demonstrated for the V$_2$O$_5$@V$_2$O$_5$ yolk–shell particles retaining 89% of its specific discharge capacity after 50 cycles as compared to around 60% only for solid V$_2$O$_5$ spheres.[117]

Composites or multi-component structures are attractive for studies due to the synergetic effect between the different components. Carbon-supported amorphous and crystalline V$_2$O$_3$ microspheres both showed excellent high rate and electro-chemical performance due to the uniform distribution of partly graphitized carbon within the framework and also due to the stable structure of spheres, which assured a low charge resistance, fast electronic transport, a large surface area and

This journal is © The Royal Society of Chemistry 2016

Chem. Soc. Rev., 2016, **45**, 6013–6047 | 6039

excellent stability.[50] The amorphous spheres showed 95% retention in the discharge capacity after 7000 cycles at a high current density of 2 A g$^{-1}$, while the crystalline ones retained 98% after 9000 cycles. Ant-cave structured MoO$_3$–C composite microspheres[234] synthesized by USP exhibited high initial discharge and charge capacities of 1109 and 724 mA h g$^{-1}$ and still delivered a discharge capacity of 733 mA h g$^{-1}$ after 300 cycles. The high performance was attributed to the combination of ant-cave channel structure and conductivity of the carbon in the composite. A yolk–shell structure of CuO@NiO spheres exhibited much higher capacity than the theoretical value of 1061 mA h g$^{-1}$ after 200 cycles due to the unique multilayer hollow structure, which provided a large electrochemically active surface, more active sites for Li ion storage and facilitated Li diffusion.[283] In another example, the carbon coated triple-shell hollow spheres of CoMn$_2$O$_4$ possessed a high specific capacity of 726.7 mA h g$^{-1}$ and nearly 100% capacity retention after 200 cycles.[168]

Numerous other metal oxides and composites of various shapes and accommodating space for lithium have been successfully used in Li-ion batteries. The list of metal oxides used in Li-ion batteries is quite long and includes the following: CuO spheres and hollow spheres,[18,78,79,122] Fe$_2$O$_3$ hollow spheres,[83,88] α-Fe$_2$O$_3$ multi-shell hollow spheres,[172,231] Co$_3$O$_4$ spheres,[28] Co$_3$O$_4$ multiple shells,[171] Gd$_2$O$_3$ hollow spheres,[145] NiO spheres and hollow spheres,[41,103,149,284] TiO$_2$ hollow spheres,[285] TiO$_2$ yolk–shell spheres,[281] multi-shell TiO$_2$ hollow microspheres,[174] Fe$_2$O$_3$@TiO$_2$ core–shell spheres,[204] V$_2$O$_5$ spheres and hollow spheres,[114,127,128] SnO$_2$ spheres and hollow spheres,[106,109,206,264] SnO$_2$ multi-shell spheres,[110] Li$_2$O–CuO–SnO$_2$ multi-deck cage spheres,[219] CoFe$_2$O$_4$ and other metal ferrite spheres,[29,77] core-in-double-shell NiCo$_2$O$_4$ particles,[105] multi-shell LiMn$_2$O$_4$ hollow microspheres,[286] Cr$_2$O$_3$–C core–shell spheres,[31] SnO$_2$@C spheres,[49] SnO$_2$/C composite hollow spheres[108,111] and Fe$_3$O$_4$–C composite spheres.[220]

**4.4.2 Supercapacitors.** Supercapacitors are energy storage devices that provide a large specific energy density, a high specific power density, fast charging capability and a long lifetime due to the excellent cycling stability. Metal oxides are promising materials because of their high theoretical capacitance, low cost and environmental friendliness. To enhance the rate of ion and electron transport in the electrodes and at the electrode/electrolyte interface, the structural aspects such as short diffusion path lengths, a high surface area and porosity to accommodate the strain from the high rate of insertion and extraction of ions are required.

The surface area of MnO$_2$ hollow spheres prepared by a double templating method was varied by changing the ratio of the F127 surfactant and SiO$_2$ spheres used as soft and hard templates, respectively.[97] The urchin-like hollow spheres showed the best capacitance of 266.6 F g$^{-1}$ within the potential range of 1 V at a current density of 0.1 A g$^{-1}$ due to their high surface area of 233 m$^2$ g$^{-1}$ relative to the other hollow structures. Co$_3$O$_4$ hollow spheres with thin shells of 130 nm, a moderate surface area of 60 m$^2$ g$^{-1}$ and mesopores centered at 7.8 nm, prepared hydrothermally using sucrose as a precursor for carbon

sphere templates, performed well giving a specific capacitance of 470 F g$^{-1}$ at 1 A g$^{-1}$ with no obvious capacitance decrease observed over 1000 cycles.[75] On the other hand, bacteria-templated Co$_3$O$_4$ hollow spheres prepared by a one-pot mineralization method at room temperature featured a similar average pore size of 7.7 nm but a larger surface area of 149 m$^2$ g$^{-1}$ due to their fluffy-like surface.[14] These particles showed a high capacitance of 214 F g$^{-1}$ at 2 A g$^{-1}$, a Coulombic efficiency averaging over 95% and excellent cycling stability that showed a capacitance retention of about 95% after 4000 cycles. Mn$_2$O$_3$ triple-shell hollow microspheres with thin porous shells and a large pore volume of 0.52 cm$^3$ g$^{-1}$ but a moderate surface area of 37 m$^2$ g$^{-1}$ showed a record high specific capacitance up to 1651 F g$^{-1}$ at 0.5 A g$^{-1}$, an excellent rate capability of 1422 F g$^{-1}$ at 10 A g$^{-1}$ and a cycling stability retention of 92% after 2000 cycles.[175] These findings show the importance of porosity, surface texture and high surface area for the performance of metal oxide particles as supercapacitors.

However, the particle morphology may surpass the effect of surface area in some cases, as it was shown in the case of NiO spheres prepared by a hydrothermal method.[43] It was found that NiO spheres made of ultrathin nanowires performed much better than urchin-like spheres with nearly 100% capacity retention after 200 cycles at a current density of 10 A g$^{-1}$, despite the higher surface area of the latter (243 m$^2$ g$^{-1}$ vs. 215 m$^2$ g$^{-1}$). The high capacity was attributed to the bimodal pore size distribution of the ultrathin nanowire-assembled spheres at 3.2 nm and 8.9 nm as opposed to the monomodal 4 nm pores in the urchin-like spheres as well as to their network-like surface texture, which assured efficient diffusion paths for OH$^-$ ions and greatly enhanced intercalation of the electrolyte ions, ensuring sufficient Faradic reactions.

Doped or composite structures can also perform well as supercapacitors as it was shown for Fe$_3$O$_4$ doped MnO$_2$ microspheres,[21] Ag$_2$O–MnO$_2$ composite spheres[19] and MnO$_2$/C composite spheres.[100] Core–shell C@MnO$_2$ had a high specific capacitance of 583 F g$^{-1}$ at a current density of 1 A g$^{-1}$ in 0.1 M Na$_2$SO$_4$ electrolyte,[214] which was attributed to the inner graphitized carbon core coupled with porous interconnected MnO$_2$ nanorods for enhanced electrolyte accessibility, short ion diffusion length and charge transfer pathways. Ternary metal oxides with two different metal cations also exhibited high electrochemical performance as it was demonstrated for core-in-double-shell hollow NiCo$_2$O$_4$ spheres[105] with a complex interior, porous shells and consisting of small nanocrystalline particles. This material delivered high pseudocapacitance values of 1141, 1048, 965, 862 and 784 F g$^{-1}$ at current densities of 1, 2, 5, 10 and 15 A g$^{-1}$. Furthermore, after 4000 cycles at 5 A g$^{-1}$, 94.7% of the specific capacitance was retained, proving the high stability of the spheres.

Other examples of metal oxides that have been used as supercapacitors are NiO spheres and hollow spheres,[41,124,148,244,287] La doped NiO spheres,[44] Co$_3$O$_4$ hollow spheres[242] and MnO$_2$ hollow spheres.[98]

**4.4.3 Dye sensitized solar cells (DSSCs).** In a DSSC, light is absorbed by dye molecules attached to the surface of a wide

6040 | Chem. Soc. Rev., 2016, **45**, 6013–6047

This journal is © The Royal Society of Chemistry 2016

band gap metal oxide (usually $TiO_2$) to generate free electrons, which are then injected into the conduction band of the metal oxide to be transported to an external circuit, thereby generating a current. Generally, the photoanodes in DSSCs are in the form of a film consisting of anatase $TiO_2$ nanocrystals of size *ca.* 20 nm.[192] These films have high surface area, allowing for high dye adsorption and high energy conversion efficiency. However, these films have poor separability of electrons and holes due to various defects, grain boundaries and non-homogeneity. Moreover, the small particle size means that most of the visible light of longer wavelengths passes through without being absorbed.

To address this issue, an additional layer of metal oxide particles has been deposited to enhance the light to current capability of DSSCs. The engineered particles have increased dye loading, interconnected crystals to improve the current transport, improved crystallization to intensify electron–hole separation and more importantly, enhanced back-scattering of light of longer wavelength (visible and near infrared region) onto the primary layer of DSSCs, which augments absorption of light, as shown in Fig. 16. There are numerous reports on the use of $TiO_2$ particles of varying architecture in DSSCs such as spheres,[184,190,192,195,217,245,288–290] hollow spheres,[227,248,291] and yolk–shell structures.[208]

Macroporous $TiO_2$ spheres were prepared by an emulsion templating method using PS particles as templates for the macropores,[184] and were formed *via* calcination of the PS–$TiO_2$ composite spheres. These spheres had size in the range of 500–2000 nm, pore size in the range of 200–300 nm, a surface area of 76 $m^2$ $g^{-1}$ and were composed of crystals with sizes of 6–8 nm. The high surface area assured a high amount of dye loading, which was about 1.5 times higher than that adsorbed on a commercial nano-$TiO_2$, and the proper size of spheres improved the scattering of light in the wavelength range of 500–800 nm. Hence, the geometry of particles assured a significant improvement in light scattering, and increased dye loading as well as interconnected pores (fewer grain boundaries) enhanced light to current efficiency as compared to conventional $TiO_2$ materials.

$TiO_2$ spheres of size 2.1 μm consisting of nanorods were prepared by a hydrothermal method.[289] The large surface area (64 $m^2$ $g^{-1}$) and size of the particles resulted in a high power

conversion efficiency of 10.34%. The high performance was also due to the crystal size and structure, which increased the electron transport rate and slowed down the recombination rate of electrons and holes. On the other hand, $TiO_2$ mesoporous microspheres of size *ca.* 800 nm, created by an evaporation-driven self-assembly method,[186] possessed a large surface area of 112 $m^2$ $g^{-1}$, a large pore volume of 0.164 $cm^3$ $g^{-1}$, and highly crystalline walls with [101] exposed facets. These attributes resulted in DSSCs with high energy conversion efficiency of up to 12.1%.

The wavelength of the scattered light is closely related to the size of particles. Xu *et al.*[202] showed that $TiO_2$ particles with a size of 380 nm exhibited strong resonance with light of wavelength 366 nm. However, Yu *et al.*[288] studied the effect of light scattering by the particles with sizes in the range of 260–800 nm and found that particles with a size of 450 nm showed the highest scattering of light in the range 600–750 nm and therefore the best photon to current efficiency; this was attributed to the size uniformity and long range ordering when the particles were applied as a light scattering layer in DSSCs.

Other semiconductors such as $SnO_2$,[126,243] quintuple shell $SnO_2$[173] and $Nb_2O_5$[39] have also been used in DSSCs. However, the power conversion efficiencies did not reach those of $TiO_2$-based electrodes.

## 5. Conclusions and perspectives

We have reviewed the synthesis methods and potential applications of metal oxide spherical nanoparticles. These particles were engineered to have a high surface area to volume ratio, a high pore volume, and high mechanical strength, which endorse them for a variety of applications in the catalytic, environmental, biomedical and energy fields. They can show synergistic interactions with noble metals when used as supports, making them potentially attractive catalysts. Furthermore, for specific crystal size, the quantum effects can impart semiconducting or magnetic properties to the particles, which can be beneficial in the field of photocatalysis and separation. The most common methods currently used for the synthesis of metal oxide spheres are the high temperature hydrothermal and low temperature solution precipitation methods. However, these methods are time consuming and suitable for batch production only. Thus, the emerging methods such as aerosol and spray drying or spray pyrolysis methods are well suited for continuous large scale production, and can be used to synthesize porous spheres and shells, allowing high loading of noble metals. However, further studies are required toward controlling the uniformity and size of spheres and the thickness of shells. For multi-shell hollow spheres, the finely controlled synthesis of concentric hollow spheres is still a challenge and more research in this direction is needed. Further studies on the design and synthesis of metal oxide structures, especially core–shell and yolk–shell particles with cores and shells of tailored surface properties, porosity and chemical composition for advanced catalytic, biomedical and energy-related applications, are highly
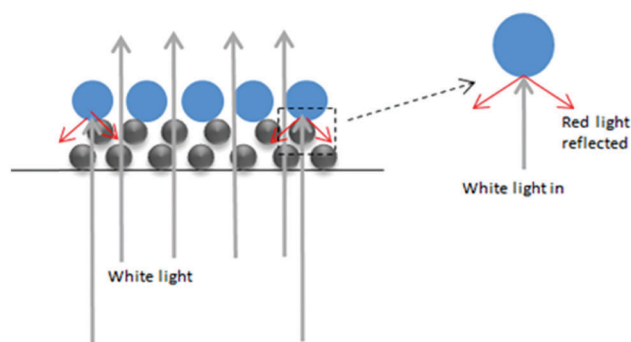


**Fig. 16** Scattering of long wavelength light (red light) due to the layer of larger particles on the top of $TiO_2$ film in a DSSC.

desirable. Since chemistry of metal oxide nanoparticles is a rapidly growing research area, new discoveries in the synthesis and applications of these materials are anticipated.

In perspective, synergetic interactions of metal oxide composites need to be further investigated to possibly avoid the use of precious metals as active agents in catalysis, and enhance the energy storage capacities of the materials used in the energy field. Multiple functionalization within the same structure could generate catalysts that can cope with tandem reactions, hence avoiding the use of two or more catalysts. Furthermore, more work on the synthesis of hollow metal oxide spheres in the nanometer regime needs to be carried out for use as nanoreactors in colloidal solutions. The new generation of porous non-silica metal oxide submicrospheres with precisely controlled functionality can be envisioned to be created by taking advantage of prosperous nanochemistry synthesis methods under mild conditions. A further development of the computationally assisted design and fabrication of complex porous non-silica metal oxide particles is needed for structure prediction and reduction of the number of synthesized samples. In the past decade, there has been a remarkable evolution in porous non-silica metal oxide submicrospheres with unique properties as platforms for emerging applications, which envisages a bright and exciting future for these unique materials.

## Abbreviations

| BET | Brunauer–Emmett–Teller |
|---|---|
| CS | Carbon spheres |
| CTAB | Cetyltrimethylammonium bromide |
| DEX | Dexamethasone |
| DMF | N,N-Dimethylformamide |
| EDA | Ethylenediamine |
| EG | Ethylene glycol |
| ERY | Erythromycin |
| GMA-co-EGDMA | Glycidyl methacrylate-co-ethylene glycol dimethacrylate |
| HMT | Hexamethylenetetramine |
| IBU | Ibuprofen |
| IUPAC | International Union of Pure and Applied Chemistry |
| MEA | Monoethanolamine |
| PEG | Poly-ethylene glycol |
| PEO-b-PS | Polyethylene oxide-block-polystyrene |
| PEO–PPO–PEO | Poly(ethylene oxide)–poly(propylene oxide)–poly(ethylene oxide) |
| PS | Polystyrene |
| PVP | Polyvinyl pyrrolidone |
| SDBS | Sodium dodecylbenzenesulfonate |
| TBOT | Titanium butoxide |
| TEA | Triethanolamine |
| TEOS | Tetraethyl orthosilicate |
| TFA | Trifluoroacetic acid |
| THF | Tetrahydrofuran |

## Acknowledgements

## Notes and references

1  A. P. Alivisatos, *Science*, 1996, **271**, 933–937.
2  M. Khairy, S. A. El-Safty, M. Ismael and H. Kawarada, *Appl. Catal., B*, 2012, **127**, 1–10.
3  H. Li, Z. Bian, J. Zhu, D. Zhang, G. Li, Y. Huo, H. Li and Y. Lu, *J. Am. Chem. Soc.*, 2007, **129**, 8406–8407.
4  P. Zhang, A. Li and J. Gong, *Particuology*, 2015, **22**, 13–23.
5  D. Chen and R. A. Caruso, *Adv. Funct. Mater.*, 2013, **23**, 1356–1374.
6  W. Wu, Z. Wu, T. Yu, C. Jiang and W.-S. Kim, *Sci. Technol. Adv. Mater.*, 2015, **16**, DOI: 10.1088/1468-6996/16/2/023501.
7  J.-H. Lee, *Sens. Actuators, B*, 2009, **140**, 319–336.
8  X. Lai, J. E. Halpert and D. Wang, *Energy Environ. Sci.*, 2012, **5**, 5604–5618.
9  Z. Wang and L. Zhou, *Adv. Mater.*, 2012, **24**, 1903–1911.
10  J. Hu, M. Chen, X. Fang and L. Wu, *Chem. Soc. Rev.*, 2011, **40**, 5472–5491.
11  J. Qi, X. Lai, J. Wang, H. Tang, H. Ren, Y. Yang, Q. Jin, L. Zhang, R. Yu, G. Ma, Z. Su, H. Zhao and D. Wang, *Chem. Soc. Rev.*, 2015, **44**, 6749–6773.
12  X. W. Lou, L. A. Archer and Z. Yang, *Adv. Mater.*, 2008, **20**, 3987–4019.
13  K. Byrappa and T. Adschiri, *Prog. Cryst. Growth Charact. Mater.*, 2007, **53**, 117–166.
14  H.-W. Shim, A.-H. Lim, J.-C. Kim, E. Jang, S.-D. Seo, G.-H. Lee, T. D. Kim and D.-W. Kim, *Sci. Rep.*, 2013, **3**, 2325, DOI: 10.1038/srep02325.
15  X. Zou, H. Fan, Y. Tian, M. Zhang and X. Yan, *Dalton Trans.*, 2015, **44**, 7811–7821.
16  H. Cao, A. Yang, H. Li, L. Wang, S. Li, J. Kong, X. Bao and R. Yang, *Sens. Actuators, B*, 2015, **214**, 169–173.
17  T. Zhang and D. D. Sun, *Chem. Eng. J.*, 2013, **225**, 271–279.
18  Z. Yuan, Y. Wang and Y. Qian, *RSC Adv.*, 2012, **2**, 8602–8605.
19  Y. Dai, S. Tang, S. Vongehr and X. Meng, *ACS Sustainable Chem. Eng.*, 2014, **2**, 692–698.
20  T. Lin, L. Yu, M. Sun, G. Cheng, B. Lan and Z. Fu, *Chem. Eng. J.*, 2016, **286**, 114–121.
21  J. Zhu, S. Tang, H. Xie, Y. Dai and X. Meng, *ACS Appl. Mater. Interfaces*, 2014, **6**, 17637–17646.
22  M.-G. Ma, J.-F. Zhu, R.-C. Sun and Y.-J. Zhu, *Mater. Lett.*, 2010, **64**, 1524–1527.
23  F. Qin, H. Zhao, G. Li, H. Yang, J. Li, R. Wang, Y. Liu, J. Hu, H. Sun and R. Chen, *Nanoscale*, 2014, **6**, 5402–5409.
24  Y. Li, J. Liu, X. Huang and G. Li, *Cryst. Growth Des.*, 2007, **7**, 1350–1355.
25  D. Ma, S. Huang, W. Chen, S. Hu, F. Shi and K. Fan, *J. Phys. Chem. C*, 2009, **113**, 4369–4374.
26  X. Liang, J. Xiao, B. Chen and Y. Li, *Inorg. Chem.*, 2010, **49**, 8188–8190.

27 C. Sun, S. Rajasekhara, Y. Chen and J. B. Goodenough, *Chem. Commun.*, 2011, **47**, 12852–12854.

28 W. Hao, S. Chen, Y. Cai, L. Zhang, Z. Li and S. Zhang, *J. Mater. Chem. A*, 2014, **2**, 13801–13804.

29 S. Yoon, *J. Appl. Electrochem.*, 2014, **44**, 1069–1074.

30 H. Ma, Y. Xu, Z. Rong, X. Cheng, S. Gao, X. Zhang, H. Zhao and L. Huo, *Sens. Actuators, B*, 2012, **174**, 325–331.

31 L.-Y. Jiang, S. Xin, X.-L. Wu, H. Li, Y.-G. Guo and L.-J. Wan, *J. Mater. Chem.*, 2010, **20**, 7565–7569.

32 S. Yang, S. Zhang, H. Wang, H. Yu, Y. Fang and F. Peng, *RSC Adv.*, 2014, **4**, 43024–43028.

33 R. Liu, J. Yin, W. Du, F. Gao, Y. Fan and Q. Lu, *Eur. J. Inorg. Chem.*, 2013, 1358–1362.

34 G. Liu, Q. Deng, H. Wang, D. H. Ng, M. Kong, W. Cai and G. Wang, *J. Mater. Chem.*, 2012, **22**, 9704–9713.

35 C. Wang, Y. Cui and K. Tang, *Nanoscale Res. Lett.*, 2013, **8**, 1–4.

36 M. Muruganandham, R. Amutha, M. S. A. Wahed, B. Ahmmad, Y. Kuroda, R. P. Suri, J. J. Wu and M. E. Sillanpaa, *J. Phys. Chem. C*, 2011, **116**, 44–53.

37 H. Yang, L. Liu, H. Liang, J. Wei and Y. Yang, *CrystEngComm*, 2011, **13**, 5011–5016.

38 B. Tao, Y. Zhang, D. Han, Y. Li and Z. Yan, *J. Mater. Chem. A*, 2014, **2**, 5455–5461.

39 X. Jin, C. Liu, J. Xu, Q. Wang and D. Chen, *RSC Adv.*, 2014, **4**, 35546–35553.

40 C. C. Li, J. Dou, L. Chen, J. Lin and H. C. Zeng, *ChemCatChem*, 2012, **4**, 1675–1682.

41 A. K. Mondal, D. Su, Y. Wang, S. Chen, Q. Liu and G. Wang, *J. Alloys Compd.*, 2014, **582**, 522–527.

42 T. Zhu, J. S. Chen and X. W. Lou, *J. Phys. Chem. C*, 2012, **116**, 6873–6878.

43 X. Li, S. Xiong, J. Li, J. Bai and Y. Qian, *J. Mater. Chem.*, 2012, **22**, 14276–14283.

44 D. Han, X. Jing, J. Wang, P. Yang, D. Song and J. Liu, *J. Electroanal. Chem.*, 2012, **682**, 37–44.

45 P.-P. Jin, X. Zou, L.-J. Zhou, J. Zhao, H. Chen, Y. Tian and G.-D. Li, *Sens. Actuators, B*, 2014, **204**, 142–148.

46 Z. Li, Q. Zhao, W. Fan and J. Zhan, *Nanoscale*, 2011, **3**, 1646–1652.

47 X. Wang, S. Qiu, C. He, G. Lu, W. Liu and J. Liu, *RSC Adv.*, 2013, **3**, 19002–19008.

48 X. Wang, S. Qiu, J. Liu, C. He, G. Lu and W. Liu, *Eur. J. Inorg. Chem.*, 2014, 863–869.

49 X. W. Lou, J. S. Chen, P. Chen and L. A. Archer, *Chem. Mater.*, 2009, **21**, 2868–2874.

50 C. Niu, M. Huang, P. Wang, J. Meng, X. Liu, X. Wang, K. Zhao, Y. Yu, Y. Wu and C. Lin, *Nano Res.*, 2015, 1–11.

51 C. Zhang, Z. Chen, Z. Guo and X. W. D. Lou, *Energy Environ. Sci.*, 2013, **6**, 974–978.

52 S. Jeon and K. Yong, *J. Mater. Chem.*, 2010, **20**, 10146–10151.

53 W. Zeng, C. Dong, B. Miao, H. Zhang, S. Xu, X. Ding and S. Hussain, *Mater. Lett.*, 2014, **117**, 41–44.

54 S. A. K. Leghari, S. Sajjad and J. Zhang, *RSC Adv.*, 2013, **3**, 15354–15361.

55 M. K. Devaraju, S. Yin and T. Sato, *Inorg. Chem.*, 2011, **50**, 4698–4704.

56 X. Liu, J. Zhang, L. Wang, T. Yang, X. Guo, S. Wu and S. Wang, *J. Mater. Chem.*, 2011, **21**, 349–356.

57 W. Wang, Y. Tian, X. Wang, H. He, Y. Xu, C. He and X. Li, *J. Mater. Sci.*, 2013, **48**, 3232–3238.

58 A. Lei, B. Qu, W. Zhou, Y. Wang, Q. Zhang and B. Zou, *Mater. Lett.*, 2012, **66**, 72–75.

59 W. Guo, T. Liu, J. Wang, W. Yu, R. Sun, Y. Chen, S. Hussain, X. Peng and Z. Wang, *Ceram. Int.*, 2013, **39**, 5919–5924.

60 Y. Lai, M. Meng and Y. Yu, *Appl. Catal., B*, 2010, **100**, 491–501.

61 X. Fu, X. Yang, Z. Qiu, F. Zhao, J. Zhuang, A. He, L. Chen, C. Wu, X. Duan and C. Liang, *CrystEngComm*, 2013, **15**, 3334–3340.

62 C. Wang, Y. Le and B. Cheng, *Ceram. Int.*, 2014, **40**, 10847–10856.

63 L. Nie, A. Meng, J. Yu and M. Jaroniec, *Sci. Rep.*, 2013, **3**, 3215, DOI: 10.1038/srep03215.

64 Z. Dong, T. Ye, Y. Zhao, J. Yu, F. Wang, L. Zhang, X. Wang and S. Guo, *J. Mater. Chem.*, 2011, **21**, 5978–5984.

65 S.-H. Hsieh, G.-J. Lee, C.-Y. Chen, J.-H. Chen, S.-H. Ma, T.-L. Horng, K.-H. Chen and J. J. Wu, *Top. Catal.*, 2013, **56**, 623–629.

66 Y. Huo, Y. Jin and Y. Zhang, *J. Mol. Catal. A: Chem.*, 2010, **331**, 15–20.

67 Z. Shen, J. Liu, F. Hu, S. Liu, N. Cao, Y. Sui, Q. Zeng and Y. Shen, *CrystEngComm*, 2014, **16**, 3387–3394.

68 D. Zhang, Y. Qian, L. Shi, H. Mai, R. Gao, J. Zhang, W. Yu and W. Cao, *Catal. Commun.*, 2012, **26**, 164–168.

69 Y. Jiao, F. Wang, X. Ma, Q. Tang, K. Wang, Y. Guo and L. Yang, *Microporous Mesoporous Mater.*, 2013, **176**, 1–7.

70 Z. Yang, J. Wei, H. Yang, L. Liu, H. Liang and Y. Yang, *Eur. J. Inorg. Chem.*, 2010, 3354–3359.

71 S. Yuan, Q. Zhang, B. Xu, Z. Jin, Y. Zhang, Y. Yang, M. Zhang and T. Ohno, *RSC Adv.*, 2014, **4**, 62255–62261.

72 G. Shen, H. Liu, Q. Wang, Z. Wang and Y. Chen, *J. Nanopart. Res.*, 2012, **14**, 1–8.

73 H. Jiu, Y. Sun, L. Zhang, C. Zhang, J. Zhang and J. Liu, *Ceram. Int.*, 2014, **40**, 3149–3154.

74 C. Chen, X. Fang, B. Wu, L. Huang and N. Zheng, *ChemCatChem*, 2012, **4**, 1578–1586.

75 H. Du, L. Jiao, Q. Wang, J. Yang, L. Guo, Y. Si, Y. Wang and H. Yuan, *Nano Res.*, 2013, **6**, 87–98.

76 J. Zhao, Y. C. Zou, X. X. Zou, T. Y. Bai, Y. P. Liu, R. Q. Gao, D. J. Wang and G. D. Li, *Nanoscale*, 2014, **6**, 7255–7262.

77 S. Li, A. Li, R. Zhang, Y. He, Y. Zhai and L. Xu, *Nano Res.*, 2014, **7**, 1116–1127.

78 C. Wang, Q. Li, F. Wang, G. Xia, R. Liu, D. Li, N. Li, J. S. Spendelow and G. Wu, *ACS Appl. Mater. Interfaces*, 2014, **6**, 1243–1250.

79 X. Guan, L. Li, G. Li, Z. Fu, J. Zheng and T. Yan, *J. Alloys Compd.*, 2011, **509**, 3367–3374.

80 S. Wang, P. Li, H. Zhu and W. Tang, *Powder Technol.*, 2012, **230**, 48–53.

This journal is © The Royal Society of Chemistry 2016

*Chem. Soc. Rev.*, 2016, **45**, 6013–6047 | 6043

81 D. Li, Q. Qin, X. Duan, J. Yang, W. Guo and W. Zheng, *ACS Appl. Mater. Interfaces*, 2013, **5**, 9095–9100.

82 Z. Wu, K. Yu, S. Zhang and Y. Xie, *J. Phys. Chem. C*, 2008, **112**, 11307–11313.

83 B. Wang, J. S. Chen, H. B. Wu, Z. Wang and X. W. Lou, *J. Am. Chem. Soc.*, 2011, **133**, 17146–17148.

84 L. Wang, Z. Lou, J. Deng, R. Zhang and T. Zhang, *ACS Appl. Mater. Interfaces*, 2015, **7**, 13098–13104.

85 S.-W. Cao, Y.-J. Zhu, M.-Y. Ma, L. Li and L. Zhang, *J. Phys. Chem. C*, 2008, **112**, 1851–1856.

86 W. Li, Y. Deng, Z. Wu, X. Qian, J. Yang, Y. Wang, D. Gu, F. Zhang, B. Tu and D. Zhao, *J. Am. Chem. Soc.*, 2011, **133**, 15830–15833.

87 Z.-G. Wu, Y.-J. Zhong, J.-T. Li, X.-D. Guo, L. Huang, B. Zhong and S.-G. Sun, *J. Mater. Chem. A*, 2014, **2**, 12361–12367.

88 L.-P. Zhu, L.-L. Wang, N.-C. Bing, C. Huang, L.-J. Wang and G.-H. Liao, *ACS Appl. Mater. Interfaces*, 2013, **5**, 12478–12487.

89 F. X. Ma, H. Hu, H. B. Wu, C. Y. Xu, Z. Xu and L. Zhen, *Adv. Mater.*, 2015, **27**, 4097–4101.

90 B. Wang, H. Wu, L. Yu, R. Xu and T. T. Lim, *Adv. Mater.*, 2012, **24**, 1111–1116.

91 X. Li, C. Tang, M. Ai, L. Dong and Z. Xu, *Chem. Mater.*, 2010, **22**, 4879–4889.

92 Y. Teng, L. X. Song, A. Ponchel, Z. K. Yang and J. Xia, *Adv. Mater.*, 2014, **26**, 6238–6243.

93 T. Zhang, M. Chen, F. Gu, D. Han, Z. Wang and G. Guo, *Integr. Ferroelectr.*, 2012, **138**, 117–122.

94 S.-J. Kim, I.-S. Hwang, C. W. Na, I.-D. Kim, Y. C. Kang and J.-H. Lee, *J. Mater. Chem.*, 2011, **21**, 18560–18567.

95 L.-X. Li, D. Xu, X.-Q. Li, W.-C. Liu and Y. Jia, *New J. Chem.*, 2014, **38**, 5445–5452.

96 S. Yang, P. Huang, L. Peng, C. Cao, Y. Zhu, F. Wei, Y. Sun and W. Song, *J. Mater. Chem. A*, 2016, **4**, 400–406.

97 J. Ma, Q. Cheng, V. Pavlinek, P. Saha and C. Li, *New J. Chem.*, 2013, **37**, 722–728.

98 S.-W. Bian, Y.-P. Zhao and C.-Y. Xian, *Mater. Lett.*, 2013, **111**, 75–77.

99 D. Li, X. Wu and Y. Chen, *J. Phys. Chem. C*, 2013, **117**, 11040–11046.

100 G. Wang, H. Xu, L. Lu and H. Zhao, *J. Mater. Chem. A*, 2015, **3**, 1127–1132.

101 H. Zhang, Y. Li, Z. Hong and M. Wei, *Mater. Lett.*, 2012, **79**, 148–151.

102 X. Zhang, X. Song, S. Gao, Y. Xu, X. Cheng, H. Zhao and L. Huo, *J. Mater. Chem. A*, 2013, **1**, 6858–6864.

103 D. Xie, Q. Su, Z. Dong, J. Zhang and G. Du, *CrystEngComm*, 2013, **15**, 8314–8319.

104 L. Chu, M. Li, Z. Wan, L. Ding, D. Song, S. Dou, J. Chen and Y. Wang, *CrystEngComm*, 2014, **16**, 11096–11101.

105 L. Shen, L. Yu, X. Y. Yu, X. Zhang and X. W. D. Lou, *Angew. Chem., Int. Ed.*, 2015, **54**, 1868–1872.

106 X. M. Yin, C. C. Li, M. Zhang, Q. Y. Hao, S. Liu, L. B. Chen and T. H. Wang, *J. Phys. Chem. C*, 2010, **114**, 8084–8088.

107 S. Liu, G. Huang, J. Yu, T. W. Ng, H. Y. Yip and P. K. Wong, *ACS Appl. Mater. Interfaces*, 2014, **6**, 2407–2414.

108 X. W. Lou, D. Deng, J. Y. Lee and L. A. Archer, *Chem. Mater.*, 2008, **20**, 6562–6566.

109 S. Ding and X. W. D. Lou, *Nanoscale*, 2011, **3**, 3586–3588.

110 H. X. Yang, J. F. Qian, Z. X. Chen, X. P. Ai and Y. L. Cao, *J. Phys. Chem. C*, 2007, **111**, 14067–14071.

111 P. Wu, N. Du, H. Zhang, C. Zhai and D. Yang, *ACS Appl. Mater. Interfaces*, 2011, **3**, 1946–1952.

112 Z. Zheng, B. Huang, X. Qin, X. Zhang and Y. Dai, *J. Colloid Interface Sci.*, 2011, **358**, 68–72.

113 M. Sharma, D. Das, A. Baruah, A. Jain and A. K. Ganguli, *Langmuir*, 2014, **30**, 3199–3208.

114 E. Uchaker, N. Zhou, Y. Li and G. Cao, *J. Phys. Chem. C*, 2013, **117**, 1621–1626.

115 D. Su, S. X. Dou and G. Wang, *J. Mater. Chem. A*, 2014, **2**, 11185–11194.

116 H. B. Wu, A. Pan, H. H. Hng and X. W. D. Lou, *Adv. Funct. Mater.*, 2013, **23**, 5669–5674.

117 A. Pan, H. B. Wu, L. Yu and X. W. D. Lou, *Angew. Chem.*, 2013, **125**, 2282–2286.

118 J. Yu and X. Yu, *Environ. Sci. Technol.*, 2008, **42**, 4902–4907.

119 X. Ma, X. Zhang, L. Yang, K. Wang, K. Jiang, Z. Wei and Y. Guo, *CrystEngComm*, 2014, **16**, 7933–7941.

120 Y. Sun, L. Zhang, J. Zhang, P. Chen, S. Xin, Z. Li and J. Liu, *Ceram. Int.*, 2014, **40**, 1599–1603.

121 H.-S. Roh, G. K. Choi, J.-S. An, C. M. Cho, D. H. Kim, I. J. Park, T. H. Noh, D.-W. Kim and K. S. Hong, *Dalton Trans.*, 2011, **40**, 6901–6905.

122 Z. Zhang, H. Chen, H. Che, Y. Wang and F. Su, *Mater. Chem. Phys.*, 2013, **138**, 593–600.

123 W. Luo, Y. Li, J. Dong, J. Wei, J. Xu, Y. Deng and D. Zhao, *Angew. Chem., Int. Ed.*, 2013, **52**, 10505–10510.

124 C. Yuan, X. Zhang, L. Su, B. Gao and L. Shen, *J. Mater. Chem.*, 2009, **19**, 5772–5777.

125 P. Manjula, R. Boppella and S. V. Manorama, *ACS Appl. Mater. Interfaces*, 2012, **4**, 6252–6260.

126 G. Shang, J. Wu, M. Huang, J. Lin, Z. Lan, Y. Huang and L. Fan, *J. Phys. Chem. C*, 2012, **116**, 20140–20145.

127 S. Wang, Z. Lu, D. Wang, C. Li, C. Chen and Y. Yin, *J. Mater. Chem.*, 2011, **21**, 6365–6369.

128 J. Shao, X. Li, Z. Wan, L. Zhang, Y. Ding, L. Zhang, Q. Qu and H. Zheng, *ACS Appl. Mater. Interfaces*, 2013, **5**, 7671–7675.

129 J. Huang, X. Xu, C. Gu, G. Fu, W. Wang and J. Liu, *Mater. Res. Bull.*, 2012, **47**, 3224–3232.

130 S. Bai, K. Zhang, L. Wang, J. Sun, R. Luo, D. Li and A. Chen, *J. Mater. Chem. A*, 2014, **2**, 7927–7934.

131 J. Huang, X. Xu, C. Gu, M. Yang, M. Yang and J. Liu, *J. Mater. Chem.*, 2011, **21**, 13283–13289.

132 P. Zhao, Y. Zhu, X. Yang, K. Fan, J. Shen and C. Li, *RSC Adv.*, 2012, **2**, 10592–10597.

133 F. Wang, X. Wang, D. Liu, J. Zhen, J. Li, Y. Wang and H. Zhang, *ACS Appl. Mater. Interfaces*, 2014, **6**, 22216–22223.

134 H. Liu, G. Shao, W. Jia, Z. Zhang, Y. Zhang, J. Liang, X. Liu, H. Jia and B. Xu, *CrystEngComm*, 2013, **15**, 3615–3622.

135 P. Ma, Y. Wu, Z. Fu and W. Wang, *J. Alloys Compd.*, 2011, **509**, 3576–3581.

136 J. He, J. Chen, L. Ren, Y. Wang, C. Teng, M. Hong, J. Zhao and B. Jiang, *ACS Appl. Mater. Interfaces*, 2014, **6**, 2718–2725.

137 J. H. Pan, Y. Bai and Q. Wang, *Langmuir*, 2015, **31**, 4566–4572.

138 W. Zhang, Z. X. Chi, W. X. Mao, R. W. Lv, A. M. Cao and L. J. Wan, *Angew. Chem.*, 2014, **126**, 12990–12994.

139 B. Bai, W. Guan, Z. Li and G. Li Puma, *Mater. Res. Bull.*, 2011, **46**, 26–31.

140 Y. Chen and J. Lu, *J. Porous Mater.*, 2012, **19**, 289–294.

141 C.-A. Wang, S. Li and L. An, *Chem. Commun.*, 2013, **49**, 7427–7429.

142 N. Kang, J. H. Park, M. Jin, N. Park, S. M. Lee, H. J. Kim, J. M. Kim and S. U. Son, *J. Am. Chem. Soc.*, 2013, **135**, 19115–19118.

143 Y. Qin, F. Zhang, Y. Chen, Y. Zhou, J. Li, A. Zhu, Y. Luo, Y. Tian and J. Yang, *J. Phys. Chem. C*, 2012, **116**, 11994–12000.

144 C. Deng, H. Hu, X. Ge, C. Han, D. Zhao and G. Shao, *Ultrason. Sonochem.*, 2011, **18**, 932–937.

145 G. Tian, Z. Gu, X. Liu, L. Zhou, W. Yin, L. Yan, S. Jin, W. Ren, G. Xing and S. Li, *J. Phys. Chem. C*, 2011, **115**, 23790–23796.

146 W. J. Tseng, T. T. Tseng, H. M. Wu, Y. C. Her and T. J. Yang, *J. Am. Ceram. Soc.*, 2013, **96**, 719–725.

147 Y. Liu, Z. Chen, C.-H. Shek, C.-M. L. Wu and J. K.-L. Lai, *ACS Appl. Mater. Interfaces*, 2014, **6**, 9776–9784.

148 S. Ding, T. Zhu, J. S. Chen, Z. Wang, C. Yuan and X. W. D. Lou, *J. Mater. Chem.*, 2011, **21**, 6602–6606.

149 D. Xie, W. Yuan, Z. Dong, Q. Su, J. Zhang and G. Du, *Electrochim. Acta*, 2013, **92**, 87–92.

150 L. Shi and H. Lin, *Langmuir*, 2010, **26**, 18718–18722.

151 F. Gyger, M. Hubner, C. Feldmann, N. Barsan and U. Weimar, *Chem. Mater.*, 2010, **22**, 4821–4827.

152 S. Ding, J. S. Chen, G. Qi, X. Duan, Z. Wang, E. P. Giannelis, L. A. Archer and X. W. Lou, *J. Am. Chem. Soc.*, 2010, **133**, 21–23.

153 G. Xi, Y. Yan, Q. Ma, J. Li, H. Yang, X. Lu and C. Wang, *Chem. – Eur. J.*, 2012, **18**, 13949–13953.

154 Y. Liu, Q. Li, S. Gao and J. Shang, *CrystEngComm*, 2014, **16**, 7493–7501.

155 G. Jia, H. You, Y. Song, Y. Huang, M. Yang and H. Zhang, *Inorg. Chem.*, 2010, **49**, 7721–7725.

156 Z. Xu, Y. Gao, T. Liu, L. Wang, S. Bian and J. Lin, *J. Mater. Chem.*, 2012, **22**, 21695–21703.

157 H. Jiu, Y. Fu, L. Zhang, Y. Sun, Y. Wang and T. Han, *Micro Nano Lett.*, 2012, **7**, 947–950.

158 F. Meng, J. Yin, Y.-Q. Duan, Z.-H. Yuan and L.-J. Bie, *Sens. Actuators, B*, 2011, **156**, 703–708.

159 Y. Wei, Y. Huang, J. Wu, M. Wang, C. Guo, D. Qiang, S. Yin and T. Sato, *J. Hazard. Mater.*, 2013, **248**, 202–210.

160 H. Yao, D. Jia and H. Zhang, *Ceram. Int.*, 2015, **41**, 1531–1534.

161 Y. Xia and R. Mokaya, *J. Mater. Chem.*, 2005, **15**, 3126–3131.

162 X. Sun, J. Liu and Y. Li, *Chem. – Eur. J.*, 2006, **12**, 2039–2047.

163 M.-M. Titirici, M. Antonietti and A. Thomas, *Chem. Mater.*, 2006, **18**, 3808–3812.

164 P. M. Arnal, C. Weidenthaler and F. Schüth, *Chem. Mater.*, 2006, **18**, 2733–2739.

165 D. G. Shchukin and R. A. Caruso, *Chem. Mater.*, 2004, **16**, 2287–2292.

166 H. Ren, J. J. Sun, R. B. Yu, M. Yang, L. Gu, P. R. Liu, H. J. Zhao, D. Kisailus and D. Wang, *Chem. Sci.*, 2016, **7**, 793–798.

167 X. Zeng, J. Yang, L. Shi, L. Li and M. Gao, *Nanoscale Res. Lett.*, 2014, **9**, 1–10.

168 G. Zhang and X. W. D. Lou, *Angew. Chem., Int. Ed.*, 2014, **53**, 9041–9044.

169 X. Lai, J. Li, B. A. Korgel, Z. Dong, Z. Li, F. Su, J. Du and D. Wang, *Angew. Chem., Int. Ed.*, 2011, **50**, 2738–2741.

170 Z. H. Dong, X. Y. Lai, J. E. Halpert, N. L. Yang, L. X. Yi, J. Zhai, D. Wang, Z. Y. Tang and L. Jiang, *Adv. Mater.*, 2012, **24**, 1046–1049.

171 J. Y. Wang, N. L. Yang, H. J. Tang, Z. H. Dong, Q. Jin, M. Yang, D. Kisailus, H. J. Zhao, Z. Y. Tang and D. Wang, *Angew. Chem., Int. Ed.*, 2013, **52**, 6417–6420.

172 S. M. Xu, C. M. Hessel, H. Ren, R. B. Yu, Q. Jin, M. Yang, H. J. Zhao and D. Wang, *Energy Environ. Sci.*, 2014, **7**, 632–637.

173 Z. Dong, H. Ren, C. M. Hessel, J. Wang, R. Yu, Q. Jin, M. Yang, Z. Hu, Y. Chen, Z. Tang, H. Zhao and D. Wang, *Adv. Mater.*, 2014, **26**, 905–909.

174 H. Ren, R. Yu, J. Wang, Q. Jin, M. Yang, D. Mao, D. Kisailus, H. Zhao and D. Wang, *Nano Lett.*, 2014, **14**, 6679–6684.

175 J. Y. Wang, H. J. Tang, H. Ren, R. B. Yu, J. Qi, D. Mao, H. J. Zhao and D. Wang, *Adv. Sci.*, 2014, **1**, DOI: 10.1002/advs.201400011.

176 J. Wang, H. Tang, L. Zhang, H. Ren, R. Yu, Q. Jin, J. Qi, D. Mao, M. Yang, Y. Wang, P. Liu, Y. Zhang, Y. Wen, L. Gu, G. Ma, Z. Su, Z. Tang, H. Zhao and D. Wang, *Nat. Energy*, 2016, **1**, 16050.

177 J. B. Joo, I. Lee, M. Dahl, G. D. Moon, F. Zaera and Y. Yin, *Adv. Funct. Mater.*, 2013, **23**, 4246–4254.

178 J. Chen, D. W. Wang, J. Qi, G. D. Li, F. Y. Zheng, S. X. Li, H. J. Zhao and Z. Y. Tang, *Small*, 2015, **11**, 420–425.

179 H. M. Abdelaal and B. Harbrecht, *C. R. Chim.*, 2015, **18**, 379–384.

180 L. Zong, P. Xu, Y. Ding, K. Zhao, Z. Wang, X. Yan, R. Yu, J. Chen and X. Xing, *Small*, 2015, **11**, 2768–2773.

181 X. Li, F. Chen, X. Lu, C. Ni, X. Zhao and Z. Chen, *J. Porous Mater.*, 2010, **17**, 297–303.

182 H. Liu, J. B. Joo, M. Dahl, L. Fu, Z. Zeng and Y. Yin, *Energy Environ. Sci.*, 2015, **8**, 286–296.

183 G. Yang, P. Hu, Y. Cao, F. Yuan and R. Xu, *Nanoscale Res. Lett.*, 2010, **5**, 1437–1441.

184 G. Veerappan, D.-W. Jung, J. Kwon, J. M. Choi, N. Heo, G.-R. Yi and J. H. Park, *Langmuir*, 2014, **30**, 3010–3018.

185 G. Zhang, X. Shen and Y. Yang, *J. Phys. Chem. C*, 2011, **115**, 7145–7152.

186 Y. Liu, R. Che, G. Chen, J. Fan, Z. Sun, Z. Wu, M. Wang, B. Li, J. Wei and Y. Wei, *Sci. Adv.*, 2015, **1**, e1500166.

This journal is © The Royal Society of Chemistry 2016

*Chem. Soc. Rev.*, 2016, **45**, 6013–6047 | 6045

187 D. Mao, J. X. Yao, X. Y. Lai, M. Yang, J. A. Du and D. Wang, *Small*, 2011, **7**, 578–582.

188 J. S. Chen, Y. L. Tan, C. M. Li, Y. L. Cheah, D. Luan, S. Madhavi, F. Y. C. Boey, L. A. Archer and X. W. Lou, *J. Am. Chem. Soc.*, 2010, **132**, 6124–6130.

189 J. H. Pan, Z. Cai, Y. Yu and X. Zhao, *J. Mater. Chem.*, 2011, **21**, 11430–11438.

190 W.-G. Yang, F.-R. Wan, Q.-W. Chen, J.-J. Li and D.-S. Xu, *J. Mater. Chem.*, 2010, **20**, 2870–2876.

191 Z. Lin, M. Zheng, B. Zhao, G. Wang, L. Pu and Y. Shi, *J. Solid State Electrochem.*, 2014, **18**, 1673–1681.

192 D. Chen, F. Huang, Y. B. Cheng and R. A. Caruso, *Adv. Mater.*, 2009, **21**, 2206–2210.

193 H. Ming, Z. Ma, H. Huang, S. Lian, H. Li, X. He, H. Yu, K. Pan, Y. Liu and Z. Kang, *Chem. Commun.*, 2011, **47**, 8025–8027.

194 K. Del Ángel-Sánchez, O. Vázquez-Cuchillo, M. Salazar-Villanueva, J. Sánchez-Ramirez, A. Cruz-López and A. Aguilar-Elguezabal, *J. Sol–Gel Sci. Technol.*, 2011, **58**, 360–365.

195 H.-E. Wang, L.-X. Zheng, C.-P. Liu, Y.-K. Liu, C.-Y. Luan, H. Cheng, Y. Y. Li, L. Martinu, J. A. Zapien and I. Bello, *J. Phys. Chem. C*, 2011, **115**, 10419–10425.

196 D. Chen, L. Cao, F. Huang, P. Imperia, Y.-B. Cheng and R. A. Caruso, *J. Am. Chem. Soc.*, 2010, **132**, 4438–4444.

197 Y. Cui, L. Liu, B. Li, X. Zhou and N. Xu, *J. Phys. Chem. C*, 2010, **114**, 2434–2439.

198 C. Wang, J. Chen, X. Zhou, W. Li, Y. Liu, Q. Yue, Z. Xue, Y. Li, A. A. Elzatahry and Y. Deng, *Nano Res.*, 2014, 1–8.

199 I. Lee, J. B. Joo, Y. Yin and F. Zaera, *Angew. Chem.*, 2011, **123**, 10390–10393.

200 J. B. Joo, Q. Zhang, M. Dahl, I. Lee, J. Goebl, F. Zaera and Y. Yin, *Energy Environ. Sci.*, 2012, **5**, 6321–6327.

201 X. Cheng, M. Chen, L. Wu and G. Gu, *Langmuir*, 2006, **22**, 3858–3863.

202 H. Xu, X. Chen, S. Ouyang, T. Kako and J. Ye, *J. Phys. Chem. C*, 2012, **116**, 3833–3839.

203 L. Cao, D. Chen and R. A. Caruso, *Angew. Chem., Int. Ed.*, 2013, **52**, 10986–10991.

204 W. Li, J. Yang, Z. Wu, J. Wang, B. Li, S. Feng, Y. Deng, F. Zhang and D. Zhao, *J. Am. Chem. Soc.*, 2012, **134**, 11864–11867.

205 B. Li, Y. Xie, M. Jing, G. Rong, Y. Tang and G. Zhang, *Langmuir*, 2006, **22**, 9380–9385.

206 P. Gurunathan, P. M. Ette and K. Ramesha, *ACS Appl. Mater. Interfaces*, 2014, **6**, 16556–16564.

207 H. Chun Zeng, *Curr. Nanosci.*, 2007, **3**, 177–181.

208 W. Q. Fang, X. H. Yang, H. Zhu, Z. Li, H. Zhao, X. Yao and H. G. Yang, *J. Mater. Chem.*, 2012, **22**, 22082–22089.

209 D. Zhang, J. Zhu, N. Zhang, T. Liu, L. Chen, X. Liu, R. Ma, H. Zhang and G. Qiu, *Sci. Rep.*, 2015, **5**, 8737, DOI: 10.1038/srep08737.

210 Y. Yin, R. M. Rioux, C. K. Erdonmez, S. Hughes, G. A. Somorjai and A. P. Alivisatos, *Science*, 2004, **304**, 711–714.

211 J. Liu, S. Z. Qiao, J. S. Chen, X. W. D. Lou, X. Xing and G. Q. M. Lu, *Chem. Commun.*, 2011, **47**, 12578–12591.

212 Y.-H. Choi, D.-H. Kim, H. S. Han, S. Shin, S.-H. Hong and K. S. Hong, *Langmuir*, 2014, **30**, 700–709.

213 M. Kong, W. Zhang, Z. Yang, S. Weng and Z. Chen, *Appl. Surf. Sci.*, 2011, **258**, 1317–1321.

214 S. Li and C.-A. Wang, *J. Colloid Interface Sci.*, 2015, **438**, 61–67.

215 J. H. Pan, X. Z. Wang, Q. Huang, C. Shen, Z. Y. Koh, Q. Wang, A. Engel and D. W. Bahnemann, *Adv. Funct. Mater.*, 2014, **24**, 95–104.

216 W. Yu, Q. Ma, C. Wang, X. Dong, J. Wang and G. Liu, *Mater. Express*, 2014, **4**, 435–440.

217 D. Hwang, H. Lee, S.-Y. Jang, S. M. Jo, D. Kim, Y. Seo and D. Y. Kim, *ACS Appl. Mater. Interfaces*, 2011, **3**, 2719–2725.

218 B. Liu, K. Nakata, M. Sakai, H. Saito, T. Ochiai, T. Murakami, K. Takagi and A. Fujishima, *Langmuir*, 2011, **27**, 8500–8508.

219 Y. Yu, C. H. Chen and Y. Shi, *Adv. Mater.*, 2007, **19**, 993–997.

220 X. Jia, Z. Chen, X. Cui, Y. Peng, X. Wang, G. Wang, F. Wei and Y. Lu, *ACS Nano*, 2012, **6**, 9911–9919.

221 D. Lehr, D. Großmann, W. Grünert and S. Polarz, *Nanoscale*, 2014, **6**, 1698–1706.

222 G. Jian, L. Liu and M. R. Zachariah, *Adv. Funct. Mater.*, 2013, **23**, 1341–1346.

223 Z. Jin, F. Wang, J. Wang, J. C. Yu and J. Wang, *Adv. Funct. Mater.*, 2013, **23**, 2137–2144.

224 G. Jian, Y. Xu, L.-C. Lai, C. Wang and M. R. Zachariah, *J. Mater. Chem. A*, 2014, **2**, 4627–4632.

225 S. Dilger, M. Wessig, M. R. Wagner, J. S. Reparaz, C. M. Sotomayor Torres, L. Qijun, T. Dekorsy and S. Polarz, *Cryst. Growth Des.*, 2014, **14**, 4593–4601.

226 Y. H. Cho, Y. C. Kang and J.-H. Lee, *Sens. Actuators, B*, 2013, **176**, 971–977.

227 J. Huo, Y. Hu, H. Jiang, W. Huang, Y. Li, W. Shao and C. Li, *Ind. Eng. Chem. Res.*, 2013, **52**, 11029–11035.

228 A. B. D. Nandiyanto, O. Arutanti, T. Ogi, F. Iskandar, T. O. Kim and K. Okuyama, *Chem. Eng. Sci.*, 2013, **101**, 523–532.

229 Y. Huang, Z. Ai, W. Ho, M. Chen and S. Lee, *J. Phys. Chem. C*, 2010, **114**, 6342–6349.

230 J. W. Overcash and K. S. Suslick, *Chem. Mater.*, 2015, **27**, 3564–3567.

231 Z. Padashbarmchi, A. H. Hamidian, H. Zhang, L. Zhou, N. Khorasani, M. Kazemzad and C. Yu, *RSC Adv.*, 2015, **5**, 10304–10309.

232 Y. J. Hong, M. Y. Son, B. K. Park and Y. C. Kang, *Small*, 2013, **9**, 2224–2227.

233 Y. J. Hong, M. Y. Son and Y. C. Kang, *Adv. Mater.*, 2013, **25**, 2279–2283.

234 Y. N. Ko, S. B. Park, K. Y. Jung and Y. C. Kang, *Nano Lett.*, 2013, **13**, 5462–5466.

235 S. H. Choi, Y. J. Hong and Y. C. Kang, *Nanoscale*, 2013, **5**, 7867–7871.

236 S. H. Choi, J.-K. Lee and Y. C. Kang, *Nanoscale*, 2014, **6**, 12421–12425.

237 S. H. Choi and Y. C. Kang, *Small*, 2014, **10**, 474–478.

238 C. Wang, M. Zhu, H. Liu, Y. Cui and Y. Chen, *RSC Adv.*, 2014, **4**, 24176–24182.

239 B. Fang, C. Zhang, G. Wang, M. Wang and Y. Ji, *Sens. Actuators, B*, 2011, **155**, 304–310.

240 P. Si, P. Chen and D.-H. Kim, *J. Mater. Chem. B*, 2013, **1**, 2696–2700.

241 M. Aghazadeh, A.-A. M. Barmi and H. M. Shiri, *Russ. J. Electrochem.*, 2013, **49**, 344–353.

242 X.-H. Xia, J.-P. Tu, X.-L. Wang, C.-D. Gu and X.-B. Zhao, *Chem. Commun.*, 2011, **47**, 5786–5788.

243 M. A. Hossain, G. Yang, M. Parameswaran, J. R. Jennings and Q. Wang, *J. Phys. Chem. C*, 2010, **114**, 21878–21884.

244 C.-Y. Cao, W. Guo, Z.-M. Cui, W.-G. Song and W. Cai, *J. Mater. Chem.*, 2011, **21**, 3204–3209.

245 P. Chen, J.-D. Peng, C.-H. Liao, P.-S. Shen and P.-L. Kuo, *J. Nanopart. Res.*, 2013, **15**, 1–11.

246 H. Wang, A. Pyatenko, K. Kawaguchi, X. Li, Z. Swiatkowska-Warkocka and N. Koshizaki, *Angew. Chem.*, 2010, **122**, 6505–6508.

247 X. Li, Y. Shimizu, A. Pyatenko, H. Wang and N. Koshizaki, *Nanotechnology*, 2012, **23**, 115602.

248 H. Wang, M. Miyauchi, Y. Ishikawa, A. Pyatenko, N. Koshizaki, Y. Li, L. Li, X. Li, Y. Bando and D. Golberg, *J. Am. Chem. Soc.*, 2011, **133**, 19102–19109.

249 X.-X. Zou, G.-D. Li, Y.-N. Wang, J. Zhao, C. Yan, M.-Y. Guo, L. Li and J.-S. Chen, *Chem. Commun.*, 2011, **47**, 1066–1068.

250 Z. Ju, C. Guo, Y. Qian, B. Tang and S. Xiong, *Nanoscale*, 2014, **6**, 3268–3273.

251 Q. Jiao, M. Fu, C. You, Y. Zhao and H. Li, *Inorg. Chem.*, 2012, **51**, 11513–11520.

252 R. D. Hancock and A. E. Martell, *Chem. Rev.*, 1989, **89**, 1875–1914.

253 J. Yang, C. Lin, Z. Wang and J. Lin, *Inorg. Chem.*, 2006, **45**, 8973–8979.

254 B. Liu, L.-M. Liu, X.-F. Lang, H.-Y. Wang, X. W. D. Lou and E. S. Aydil, *Energy Environ. Sci.*, 2014, **7**, 2592–2597.

255 C. Guo, X. Wu, M. Yan, Q. Dong, S. Yin, T. Sato and S. Liu, *Nanoscale*, 2013, **5**, 8184–8191.

256 X. Lü, F. Huang, J. Wu, S. Ding and F. Xu, *ACS Appl. Mater. Interfaces*, 2011, **3**, 566–572.

257 S. Shang, X. Jiao and D. Chen, *ACS Appl. Mater. Interfaces*, 2012, **4**, 860–865.

258 M. Pelaez, N. T. Nolan, S. C. Pillai, M. K. Seery, P. Falaras, A. G. Kontos, P. S. Dunlop, J. W. Hamilton, J. A. Byrne and K. O'Shea, *Appl. Catal., B*, 2012, **125**, 331–349.

259 G. Zhu, J. Lian, M. Hojamberdiev and W. Que, *J. Cluster Sci.*, 2013, **24**, 829–841.

260 Y. Jia, X.-Y. Yu, T. Luo, J.-H. Liu and X.-J. Huang, *RSC Adv.*, 2012, **2**, 10251–10254.

261 Q. Zhu, J.-G. Li, X. Li, X. Sun and Y. Sakka, *Sci. Technol. Adv. Mater.*, 2011, **12**, 055001.

262 J. Zhang, X. Liu, S. Wu, M. Xu, X. Guo and S. Wang, *J. Mater. Chem.*, 2010, **20**, 6453–6459.

263 G. Han, Q. Lu, G. Liu, X. Ye, S. Lin, Y. Song, B. Liu, X. Yang and G. Li, *J. Mater. Sci.: Mater. Electron.*, 2012, **23**, 1616–1620.

264 H. Wang, Q. Liang, W. Wang, Y. An, J. Li and L. Guo, *Cryst. Growth Des.*, 2011, **11**, 2942–2947.

265 N. Sutradhar, A. Sinhamahapatra, S. K. Pahari, P. Pal, H. C. Bajaj, I. Mukhopadhyay and A. B. Panda, *J. Phys. Chem. C*, 2011, **115**, 12308–12316.

266 P. Yang, S. Gai, Y. Liu, W. Wang, C. Li and J. Lin, *Inorg. Chem.*, 2011, **50**, 2182–2190.

267 R. Lv, P. Yang, F. He, S. Gai, G. Yang and J. Lin, *Chem. Mater.*, 2015, **27**, 483–496.

268 X. Wang, D. Chen, L. Cao, Y. Li, B. J. Boyd and R. A. Caruso, *ACS Appl. Mater. Interfaces*, 2013, **5**, 10926–10932.

269 Y. A. Nor, L. Zhou, A. K. Meka, C. Xu, Y. Niu, H. Zhang, N. Mitter, D. Mahony and C. Yu, *Adv. Funct. Mater.*, 2016, **26**, 5408–5418.

270 X. Wu, K. Li and H. Wang, *J. Hazard. Mater.*, 2010, **174**, 573–580.

271 D. Xiang, F. Qu, X. Chen, Z. Yu, L. Cui, X. Zhang, J. Jiang and H. Lin, *J. Sol-Gel Sci. Technol.*, 2014, **69**, 370–377.

272 Q. Wang, S. Yu, Z. Tan, R. Zhang, Z. Li, X. Gao, B. Shen and H. Su, *CrystEngComm*, 2015, **17**, 671–677.

273 Y. Hou, L. Wu, X. Wang, Z. Ding, Z. Li and X. Fu, *J. Catal.*, 2007, **250**, 12–18.

274 G. Li, H. Zhang, J. Lan, J. Li, Q. Chen, J. Liu and G. Jiang, *Dalton Trans.*, 2013, **42**, 8541–8544.

275 B. Liu, K. Nakata, M. Sakai, H. Saito, T. Ochiai, T. Murakami, K. Takagi and A. Fujishima, *Catal. Sci. Technol.*, 2012, **2**, 1933–1939.

276 H. Bai, Z. Liu, L. Liu and D. D. Sun, *Chem. – Eur. J.*, 2013, **19**, 3061–3070.

277 S. Ding, X. Yin, X. Lü, Y. Wang, F. Huang and D. Wan, *ACS Appl. Mater. Interfaces*, 2011, **4**, 306–311.

278 H. Zhang, G. Du, W. Lu, L. Cheng, X. Zhu and Z. Jiao, *CrystEngComm*, 2012, **14**, 3793–3801.

279 B. Chi, L. Zhao and T. Jin, *J. Phys. Chem. C*, 2007, **111**, 6189–6193.

280 J.-M. Tarascon and M. Armand, *Nature*, 2001, **414**, 359–367.

281 S. Yoon and A. Manthiram, *J. Phys. Chem. C*, 2011, **115**, 9410–9416.

282 S. Yoon, C. A. Bridges, R. R. Unocic and M. P. Paranthaman, *J. Mater. Sci.*, 2013, **48**, 5125–5131.

283 W. Guo, W. Sun and Y. Wang, *ACS Nano*, 2015, **9**, 11462–11471.

284 X. Yan, X. Tong, J. Wang, C. Gong, M. Zhang and L. Liang, *Mater. Lett.*, 2013, **95**, 1–4.

285 S. Ding, J. S. Chen, Z. Wang, Y. L. Cheah, S. Madhavi, X. Hu and X. W. Lou, *J. Mater. Chem.*, 2011, **21**, 1677–1680.

286 F. Wang, J. Y. Wang, H. Ren, H. J. Tang, R. B. Yu and D. Wang, *Inorg. Chem. Front.*, 2016, **3**, 365–369.

287 W. Yu, X. Jiang, S. Ding and B. Q. Li, *J. Power Sources*, 2014, **256**, 440–448.

288 I. G. Yu, Y. J. Kim, H. J. Kim, C. Lee and W. I. Lee, *J. Mater. Chem.*, 2011, **21**, 532–538.

289 J.-Y. Liao, B.-X. Lei, D.-B. Kuang and C.-Y. Su, *Energy Environ. Sci.*, 2011, **4**, 4079–4085.

290 P. Cheng, S. Du, Y. Cai, F. Liu, P. Sun, J. Zheng and G. Lu, *J. Phys. Chem. C*, 2013, **117**, 24150–24156.

291 S. Dadgostar, F. Tajabadi and N. Taghavinia, *ACS Appl. Mater. Interfaces*, 2012, **4**, 2964–2968.

This journal is © The Royal Society of Chemistry 2016

*Chem. Soc. Rev.*, 2016, **45**, 6013–6047 | 6047